

1

# UNIVERSITY OF BRISTOL

2

## DOCTORAL THESIS

3

---

4

# **Investigating, implementing, and creating methods for analysing large neuronal ensembles**

5

---

6

*Author:*

Thomas J. DELANEY

*Supervisors:*

Dr. Cian O'DONNELL

Dr. Michael C. ASHBY

7

*A thesis submitted in fulfillment of the requirements  
for the degree of Doctor of Philosophy*

8

*in the*

9

Biological Intelligence & Machine Learning Unit  
Department of Computer Science

10

11

12

July 7, 2020



## <sup>15</sup> Declaration of Authorship

<sup>16</sup> I, Thomas J. DELANEY, declare that this thesis titled, "Investigating, implementing, and  
<sup>17</sup> creating methods for analysing large neuronal ensembles" and the work presented in it are  
<sup>18</sup> my own. I confirm that:

- <sup>19</sup> • This work was done wholly or mainly while in candidature for a research degree at this  
<sup>20</sup> University.
- <sup>21</sup> • Where any part of this thesis has previously been submitted for a degree or any other  
<sup>22</sup> qualification at this University or any other institution, this has been clearly stated.
- <sup>23</sup> • Where I have consulted the published work of others, this is always clearly attributed.
- <sup>24</sup> • Where I have quoted from the work of others, the source is always given. With the  
<sup>25</sup> exception of such quotations, this thesis is entirely my own work.
- <sup>26</sup> • I have acknowledged all main sources of help.
- <sup>27</sup> • Where the thesis is based on work done by myself jointly with others, I have made  
<sup>28</sup> clear exactly what was done by others and what I have contributed myself.

<sup>29</sup>

<sup>30</sup> Signed:

<sup>31</sup> \_\_\_\_\_

<sup>32</sup> Date:

<sup>33</sup> \_\_\_\_\_



34

UNIVERSITY OF BRISTOL

35

*Abstract*

36

Engineering

37

Department of Computer Science

38

Doctor of Philosophy

39

**Investigating, implementing, and creating methods for analysing large neuronal  
ensembles**

41

by Thomas J. DELANEY

42

The Thesis Abstract is written here (and usually kept to just this page). The page is kept centered vertically so can expand into the blank space above the title too...



44

## *Acknowledgements*

45 The acknowledgments and the people to thank go here, don't forget to include your project

46 advisor...



# <sup>47</sup> Contents

<sup>48</sup>	<b>Declaration of Authorship</b>	iii
<sup>49</sup>	<b>Abstract</b>	v
<sup>50</sup>	<b>Acknowledgements</b>	vii
<sup>51</sup>	<b>1 Sensitivity of the spikes-to-fluorescence transform to calcium indicator and neu-</b>	
<sup>52</sup>	<b>ron properties</b>	3
<sup>53</sup>	1.1 Introduction . . . . .	6
<sup>54</sup>	1.2 Results . . . . .	8
<sup>55</sup>	1.2.1 A biophysical computational model can generate accurate fluores-	
<sup>56</sup>	cence traces from spike trains . . . . .	8
<sup>57</sup>	1.2.2 Spike inference algorithms perform similarly on real data compared	
<sup>58</sup>	with time series simulated from the model . . . . .	9
<sup>59</sup>	1.2.3 Relative effects of various buffers to the fluorescence signal . . . . .	10
<sup>60</sup>	1.2.4 Spike inference accuracy is sensitive to indicator properties, and likely	
<sup>61</sup>	varies within and between cells . . . . .	11
<sup>62</sup>	1.2.5 Single spike inference accuracy drops for high firing rates, but firing	
<sup>63</sup>	rate itself can be estimated from mean fluorescence amplitude . . . . .	16
<sup>64</sup>	1.3 Discussion . . . . .	19
<sup>65</sup>	1.4 Methods . . . . .	21
<sup>66</sup>	1.4.1 Calcium dynamics model . . . . .	21
<sup>67</sup>	Photon release & capture . . . . .	23
<sup>68</sup>	1.4.2 Parameter optimisation . . . . .	24
<sup>69</sup>	Fixed parameters . . . . .	25
<sup>70</sup>	1.4.3 Julia . . . . .	25
<sup>71</sup>	1.4.4 Spike inference . . . . .	27
<sup>72</sup>	Comparing spike inference quality . . . . .	29
<sup>73</sup>	1.4.5 Perturbation analysis . . . . .	29

74	1.4.6	Signal-to-noise ratio . . . . .	29
75	1.4.7	Data sources . . . . .	30
76	<b>2</b>	<b>Functional networks expand across anatomical boundaries as correlation time-scale increases</b>	<b>31</b>
77	2.1	Introduction . . . . .	34
78	2.2	Results . . . . .	35
79	2.2.1	Average correlation size increases with increasing time bin width . . .	35
80	2.2.2	Goodness-of-fit for Poisson and Gaussian distributions across increasing time bin widths . . . . .	36
81	2.2.3	Differences between and inter- and intra- regional correlations decrease with increasing bin width . . . . .	38
82	2.2.4	Connected and divided structure in correlation based networks reduces in dimension with increasing bin width . . . . .	41
83	2.2.5	Detecting communities in correlation based networks . . . . .	42
84	2.2.6	Functional communities resemble anatomical division at short timescales	42
85	2.2.7	Conditional correlations & signal correlations . . . . .	46
86	2.2.8	Absolute correlations and negative rectified correlations . . . . .	50
87	2.3	Discussion . . . . .	53
88	2.4	Data . . . . .	56
89	2.4.1	Brain regions . . . . .	56
90	2.4.2	Video recordings . . . . .	57
91	2.5	Methods . . . . .	57
92	2.5.1	Binning data . . . . .	57
93	2.5.2	Correlation coefficients . . . . .	57
94		Total correlations, $r_{SC}$ . . . . .	58
95		Shuffled total correlations . . . . .	58
96		Separating Correlations & Anti-correlations . . . . .	58
97	2.5.3	Conditioning on behavioural data . . . . .	59
98		Linear regression . . . . .	59
99		Elastic net regularisation . . . . .	59
100		Conditional covariance . . . . .	60
101		Measures of conditional correlation . . . . .	61
102	2.5.4	Information Theory . . . . .	61

107	Entropy $H(X)$	61
108	Maximum entropy limit	62
109	Mutual Information $I(X; Y)$	63
110	Variation of Information $VI(X, Y)$	64
111	Measuring entropies & mutual information	65
112	2.5.5 Network analysis	65
113	Correlation networks	65
114	Rectified correlations	65
115	Sparsifying data networks	66
116	Communities	66
117	Weighted configuration model	66
118	Sparse weighted configuration model	66
119	Spectral rejection	67
120	Node rejection	68
121	Community detection	68
122	2.5.6 Clustering Comparison	69
123	Adjusted Rand Index	69
124	Clusterings as random variables	70
125	Information based similarity measures	70
126	Information based metrics	71
127	Comparing detected communities and anatomical divisions	71
128	<b>3 A simple two parameter distribution for modelling neuronal activity and capturing neuronal association</b>	73
129	3.1 Introduction	76
130	3.2 Data	77
131	3.2.1 Experimental protocol	77
132	3.3 Methods	78
133	3.3.1 Binning data	78
134	3.3.2 Number of <i>active</i> neurons	78
135	3.3.3 Moving windows for measurements	78
136	3.3.4 Fano factor	80
137	3.3.5 Probability Distributions suitable for modelling ensemble activity	80
138	Association	80

140	Binomial distribution . . . . .	81
141	Beta-binomial distribution . . . . .	81
142	Conway-Maxwell-binomial distribution . . . . .	82
143	3.3.6 Fitting . . . . .	84
144	3.3.7 Goodness-of-fit . . . . .	86
145	3.4 Results . . . . .	86
146	3.4.1 Increases in mean number of active neurons and variance in number of active neurons at stimulus onset in some regions . . . . .	86
147	Primary visual cortex . . . . .	87
148	Hippocampus . . . . .	87
149	Thalamus . . . . .	87
150	3.4.2 Conway-Maxwell-binomial distribution is usually a better fit than bi- nomial or beta-binomial . . . . .	87
151	3.4.3 Conway-Maxwell-binomial distribution captures changes in associa- tion at stimulus onset . . . . .	92
152	3.4.4 Replicating stimulus related quenching of neural variability . . . . .	92
153	3.5 Discussion . . . . .	94
154	<b>4 Studies with practical limitations &amp; negative results</b>	<b>97</b>
155	4.1 Dynamic state space model of pairwise and higher order neuronal correlations	99
156	4.2 A multiscale model for hierarchical data applied to neuronal data . . . . .	100
157	4.3 Discussion . . . . .	101
158	<b>Bibliography</b>	<b>103</b>

# 163 List of Figures

164	1.1 A: Example spike train (blue) and the corresponding GCaMP6s fluorescence	
165	trace (green), data replotted from (Berens et al., 2018). Inset shows zoomed	
166	section of traces to highlight slow decay of GCaMP6s fluorescence relative	
167	to spike time intervals. B: Schematic diagram of the neuron calcium and	
168	GCaMP computational model. C: Good visual match of data fluorescence	
169	trace (green) and model simulated fluorescence (orange) in response to an	
170	identical spike train (blue). . . . .	7
171	1.2 A: Workflow to compare spike inference for real versus simulated fluores-	
172	cence data. B: True positive rates achieved by three different spike inference	
173	algorithms when applied to observed spike trains, and simulated spike trains.	
174	Data points overlaid as blue circles. The performance is similar from real	
175	and simulated data for each of the algorithms. . . . .	10
176	1.3 <b>Calcium Buffering Dynamics</b> (a) The proportions of bound and free cal-	
177	cium concentrations within a cell, with the associated spike train. (b)-(f) The	
178	dynamics of the concentration of (b) excited indicator bound calcium, (c) in-	
179	dicator bound calcium, (d) immobile endogenous buffer bound calcium, (e)	
180	mobile endogenous buffer bound calcium, and (f) free calcium in response to	
181	an action potential at $\sim 23.2\text{s}$ . . . . .	12
182	1.4 (a) An example trace for each of the five pairs of values used for the binding	
183	and unbinding rates of the fluorescent calcium indicator. (b) The signal-to-	
184	noise ratio of the modelled fluorescence traces using each of the four per-	
185	turbed values, and the experimental value. The SNRs for the two pairs with	
186	values lower than the experimental value are lower than the experimental pair	
187	or the higher value pairs. (c) The true-positive rates of the deconvolution al-	
188	gorithm's predictions when inferring from the observed data, and inferring	
189	from modelled traces using the perturbed and experimental values. . . . .	14

190	1.5	(a) An example trace for each of the five perturbed values for the concentration of fluorescent calcium indicator. The top two traces are produced by the lower perturbed values, the middle trace is produced by the experimental value, and the lowest two traces are produced when using the higher perturbed values. (b) The signal-to-noise ratio of the modelled fluorescence traces using each of the four perturbed values, and the experimental value. Extreme perturbations of the concentration either above or below the experimental level lowered the SNR. (c) The true-positive rates of the deconvolution algorithm's predictions when inferring from the observed data, and inferring from modelled traces using the perturbed and experimental values. We found that the algorithms performs equally badly on the two most extreme values, and performs equally well on the experimental value, and the next higher perturbed value. . . . .	15
203	1.6	(a) An example trace for each of the five perturbed values for the concentration of immobile endogenous buffer. (b) The signal-to-noise ratio of the modelled fluorescence traces using each of the four perturbed values, and the experimental value. The lower values for the immobile buffer produce the same SNR as the experimental value. But the higher perturbed values produce fluorescence traces with a lower SNR. (c) The true-positive rates of the deconvolution algorithm's predictions when inferring from the observed data, and inferring from modelled traces using the perturbed and experimental values. . . . .	17
212	1.7	<b>Simulating fluorescence traces at different firing rates</b> Example modelled traces created using simulated spike trains with a mean firing rate of 1Hz (left column), 5Hz (middle column), and 10Hz (right column). Note the difference in amplitude with different mean firing rates. . . . .	18
216	1.8	<b>Inference quality and <math>\Delta F/F_0</math> vs Firing rate</b> (left) The spike inference accuracy when applied to 30 traces created using simulated spike trains with mean firing rates of 1, 5, and 10 Hz. (right) The mean $\Delta F/F_0$ across those 30 traces for each frequency. . . . .	19

220	2.1 (A) An example of the correlation coefficients between two different pairs 221 of cells, one where both cells are in the same brain region (intra-regional 222 pair), and one where both cells are in different brain regions (inter-regional 223 pair). The correlation coefficients have been measured using different time 224 bin widths, ranging from 5ms to 3s. Note the increasing amplitude of the 225 correlations with increasing bin width. (B) A raster plot showing the spike 226 times of each pair of cells. . . . .	36
227	2.2 Mean correlation coefficients measured from pairs of 50 randomly chosen 228 neurons. (A) All possible pairs, (B) positively correlated pairs, and (C) neg- 229 atively correlated pairs. (D) Mean and standard error of $\chi^2$ test statistics for 230 Poisson and Gaussian distributions fitted to neuron spike counts. . . . .	37
231	2.3 (Left)The mean intra-region and inter-region correlations using all possible 232 pairs of $\sim$ 500 neurons, spread across 9 different brain regions. (Right) 233 Courtesy of Stringer et al. (2019), mean inter-regional (out-of-area) correla- 234 tion coefficients vs mean intra-regional (within-area) correlation coefficients 235 for a bin width of 1.2s. Note that the intra-regional coefficients are higher in 236 each case. . . . .	39
237	2.4 The mean intra-regional correlations (coloured dots) and mean inter-regional 238 correlations (black dots) for a given region, indicated on the x-axis, for dif- 239 ferent time bin widths. Each black dot represents the mean inter-regional 240 correlations between the region indicated on the x-axis and one other region. 241 (A) shows these measurements when we used a time bin width of 5ms. (B) 242 shows these measurements when we used a time bin width of 1s. Note that 243 the difference between the mean inter-regional correlations and mean intra- 244 regional correlations is smaller for 1s bins. . . . .	40
245	2.5 Mean inter-regional (main diagonal) and intra-regional (off diagonal) corre- 246 lation coefficients. (A) Shows these measurements when spike times were 247 binned using 5ms time bins. (B) Shows the same, using 1s time bins. Note 248 that the matrices are ordered according to the main diagonal values, therefore 249 the ordering is different in each subfigure. . . . .	41

250	2.6 The number of dimensions in the $k$ -partite and connected structure in the cor-	
251	relation based networks beyond the structure captured by a sparse weighted	
252	configuration null network model (see section 2.5.5), shown for different time	
253	bin widths. Note that the $k$ -partite structure disappears for time bin width	
254	greater than 200ms for all three subjects. The dimension of the connected	
255	structure reduces with increasing bin width for 2 of the 3 subjects (top row). . . . .	43
256	2.7 (A-B) Correlation matrices with detected communities indicated by white	
257	lines. Each off main diagonal entry in the matrix represents a pair of neu-	
258	rons. Those entries within a white square indicate that both of those neurons	
259	are in the same community as detected by our community detection proce-	
260	dure. Matrices shown are for 5ms and 1s time bin widths respectively. Main	
261	diagonal entries were set to 0. (C-D) Matrices showing the anatomical dis-	
262	tribution of pairs along with their community membership. Entries where	
263	both cells are in the same region are given a colour indicated by the colour	
264	bar. Entries where cells are in different regions are given the grey colour also	
265	indicated by the colour bar. . . . .	44
266	2.8 (A) The variation of information is a measure of distance between cluster-	
267	ings. The distance between the anatomical ‘clustering’ and community de-	
268	detection ‘clustering’ increases with increasing time bin width. (B) The ad-	
269	justed Rand index is a normalised similarity measure between clusterings.	
270	The anatomical and community detection clusterings become less similar as	
271	the time bin width increases. . . . .	45
272	2.9 Comparing the components of the total covariance across different values for	
273	the time bin width. We observed a consistent increase in $E[\text{cov}(X, Y Z)]$ as	
274	the time bin width increased. But we saw different trends for $\text{cov}(E[X Z], E[Y Z])$	
275	for each mouse. . . . .	46
276	2.10 Comparing the components of the total covariance across different values for	
277	the time bin width. We saw a consistent increase in $\rho_{X,Y Z}$ as the time bin	
278	width increased in all three subjects. But we saw different trends in $\rho_{\text{signal}}$ for	
279	each of the subjects. . . . .	47

280	2.11 Matrices showing the regional membership of pairs by colour, and the com-	
281	munities in which those pairs lie. (A-B) Detected communities and regional	
282	membership matrix for network based on rectified spike count correlation	
283	$\rho_{X,Y Z}$ , using time bin widths of 0.005s and 1s respectively. (C-D) Detected	
284	communities and regional membership matrix for network based on rectified	
285	signal correlation $\rho_{\text{signal}}$ , using time bin widths of 0.005s and 1s respectively.	48
286	2.12 Distance and similarity measures between the anatomical division of the neu-	
287	rons, and the communities detected in the network based on the spike count	
288	correlations $\rho_{X,Y Z}$ . (A) The variation of information is a ‘distance’ mea-	
289	sure between clusterings. The distance between the anatomical ‘clustering’	
290	and the community clustering increases as the time bin width increases. (B)	
291	The adjusted Rand index is a similarity measure between clusterings. The	
292	detected communities become less similar to the anatomical division of the	
293	cells as the time bin width increases. . . . .	49
294	2.13 Distance and similarity measures between the anatomical division of the neu-	
295	rons, and the communities detected in the network based on the signal cor-	
296	relations $\rho_{\text{signal}}$ . (A) The variation of information is a ‘distance’ measure be-	
297	tween clusterings. The distance between the anatomical ‘clustering’ and the	
298	community clustering increases as the time bin width increases. (B) The ad-	
299	justed Rand index is a similarity measure between clusterings. The detected	
300	communities become less similar to the anatomical division of the cells as	
301	the time bin width increases. . . . .	50
302	2.14 (A-B) Absolute correlation matrices with detected communities indicated by	
303	white lines. These communities are based on the absolute value of the total	
304	correlation between each pair of cells. Those entries within a white square in-	
305	dicate that both of those neurons are in the same community. Matrices shown	
306	are for 5ms and 1s time bin widths respectively. Main diagonal entries were	
307	set to 0. (C-D) Matrices showing the anatomical distribution of pairs along	
308	with their community membership. Regional membership is indicated by the	
309	colour bar. (E) Variation of information between the anatomical division of	
310	the cells, and the detected communities. (F) Adjusted Rand index between	
311	the anatomical division, and the detected communities. . . . .	51

312	2.15 (A-B) Sign reversed rectified correlation matrices with detected communities indicated by white lines. Those entries within a white square indicate that both of those neurons are in the same community. Matrices shown are for 5ms and 1s time bin widths respectively. Main diagonal entries were set to 0. (C-D) Matrices showing the anatomical distribution of pairs along with their community membership. Regional membership is indicated by the colour bar. (E) Variation of information between the anatomical division of the cells, and the detected communities. (F) Adjusted Rand index between the anatomical division, and the detected communities. . . . .	52
321	2.16 <b>Probe Locations:</b> The locations of the probes in each of the three mouse brains (Stringer et al., 2019). . . . .	57
323	2.17 <b>Entropy Limit:</b> The upper limit on entropy of binned spike count data as a function of the maximum observed spike count. The orange line is the analytical maximum. The blue line is the entropy of samples with $N = 1000$ data points taken from the discrete uniform distribution. . . . .	63
327	3.1 Figures showing the over-dispersion possible for a beta-binomial distribution relative to a binomial distribution. Parameters are shown in the captions. . . . .	82
329	3.2 Figures showing (A) the under-dispersion and (B) over-dispersion permitted by the COMb distribution relative to a binomial distribution. (C) illustrates that the $p$ parameter of the COMb distribution does not correspond to the mean of the distribution, as it does for the binomial and beta-binomial distributions. (D) shows a heatmap for the value of the Kullback-Liebler divergence between the COMb distribution and the standard binomial distribution with same value for $n$ , as a function of $p$ and $\nu$ . Parameters are shown in the captions. . . . .	85

337	3.3 (A) Raster plot showing the spikes fired by 33 randomly chosen neurons in 338       the primary visual cortex. (B-C) (B) average and (C) variance of the number 339       of active neurons, measured using a sliding window 100ms wide, split into 340       100 bins. The midpoint of the time interval for each window is used as the 341       timepoint (x-axis point) for the measurements using that window. The grey 342       shaded area indicates the presence of a visual stimulus. The opaque line is 343       an average across the 160 trials that included a visual stimulus of any kind. 344       We can see a transient increase in the average number of active neurons and 345       the variance of this number, followed by a fluctuation and another increase. . . . .	88
346	3.4 (A) Raster plot showing the spikes fired by 33 randomly chosen neurons in 347       the hippocampus. (B-C) (B) average and (C) variance of the number of active 348       neurons, measured using a sliding window 100ms wide, split into 100 bins. 349       The midpoint of the time interval for each window is used as the timepoint (x- 350       axis point) for the measurements using that window. The grey shaded area 351       indicates the presence of a visual stimulus. The opaque line is an average 352       across the 160 trials that included a visual stimulus of any kind. We can see 353       a transient increase in the average number of active neurons and the variance 354       of this number at stimulus onset. . . . .	89
355	3.5 (A) Raster plot showing the spikes fired by 33 randomly chosen neurons in 356       the thalamus. (B-C) (B) average and (C) variance of the number of active 357       neurons, measured using a sliding window 100ms wide, split into 100 bins. 358       The midpoint of the time interval for each window is used as the timepoint (x- 359       axis point) for the measurements using that window. The grey shaded area 360       indicates the presence of a visual stimulus. The opaque line is an average 361       across the 160 trials that included a visual stimulus of any kind. We can 362       see in immediate increase at stimulus onset, a subsequent fall, and another 363       sustained increased until the stimulus presentation ends. . . . .	90

- 364     3.6 (A) An example of the binomial, beta-binomial, and Conway-Maxwell-binomial  
365       distributions fitted to a sample of neural activity. The Conway-Maxwell-  
366       binomial distribution is the best fit in this case. The histogram shows the  
367       empirical distribution of the sample. The probability mass function of each  
368       distribution is indicated by a different coloured line. (B) Across all samples  
369       in all trials, the proportion of samples for which each fitted distribution was  
370       the the best fit. The Conway-Maxwell-binomial distribution was the best fit  
371       for 93% of the samples taken from V1 using a bin width of 1ms. . . . . 91
- 372     3.7 (A) We fit a Conway-Maxwell-binomial distribution to the number of active  
373       neurons in 1ms time bins of a 100ms sliding window. We did this for all  
374       trials with a visual stimulus and took the average across those trials. We  
375       see a transient drop in value for the distribution's  $\nu$  parameter at stimulus  
376       onset. This shows an increase in association between the neurons. (B) We  
377       measured the correlation coefficient between the spike counts of all possible  
378       pairs of neurons in the same sliding window. The took the average of those  
379       coefficients. We also did this for every visually stimulated trial, and took  
380       the average across trials. The increase in association is not reflected with an  
381       increase in average correlation. . . . . 93
- 382     3.8 (A) The mean Fano factor of the spike counts of the cells in the primary visual  
383       cortex. Means were taken across cells first, then across trials. There was a  
384       significant decrease in the Fano factors immediately after stimulus onset. (B)  
385       The mean Fano factor of the spike counts of the cells in the motor cortex. No  
386       significant change in measurements at any point. . . . . 94

# 387 List of Tables

388	1.1	387 <b>Fixed parameters</b> A table of the parameters fixed before optimising the	389	model. The values of these parameters could be changed to model differ-	390	ent fluorescent calcium indicators. . . . .	26
391	3.1	391 Details of the different bin width and analysis window sizes used when bin-	392	ning spike times, and analysing those data. . . . .	79		
393	3.2	393 Relative dispersion of the COMb distribution, and association between Bernoulli	394	variables as represented by the value of the $\nu$ parameter. . . . .	84		
395	3.3	395 Proportion of samples for which each distribution was the best fit, grouped	396	by bin width. The COMb distribution is the best fit most of the time. . . . .	92		



*For/Dedicated to/To my...*



## 398    **Introduction**

399    Ideas (not in order):

- 400       • From small to big datasets (in terms of number of neurons)
- 401       • Big datasets mean statistical methods are more necessary (curse of dimensionality)
- 402       • Big datasets mean higher order correlations are more meaningful (schneidman)
- 403       • Exploit pairwise correlations in different way (eight probe)
- 404       • abandon correlations embrace association (COMB)
- 405       • electrophysiology drawbacks vs calcium benefits
- 406       • calcium drawbacks (fluorescence modelling) (mention nuclear filling and cell pathology) (mention that calcium imaging can only be used near the surface of the brain, e-phys can go deeper, especially with new probes)

409       Since Hodgkin and Huxley's squid experiments featuring a single axon (Hodgkin and  
410       Huxley, 1939), to more recent research with spike sorted data from  $\sim 24000$  neurons from  
411       34 brain regions from 21 mice (Allen et al., 2019), the number of neurons contributing to  
412       electrophysiological datasets has been growing. Recording methods using two-photon cal-  
413       cium imaging have also been used to extract data from populations containing over 10000  
414       neurons (Peron et al., 2015). This dramatic growth in the number of neurons to analyse  
415       required a dramatic change in analysis methods.

416       To focus on calcium imaging for a start, a neuron that contains a fluorescent calcium  
417       indicator in its cytoplasm will fluoresce when bombarded with photons. The amount that the  
418       cell will fluoresce is dependent on the concentration of fluorescent indicator within the cell,  
419       and the concentration of calcium within the cell. When a neuron fires an action potential, the  
420       influx of free calcium ions causes an increase in fluorescence when those ions bond with the  
421       fluorescent indicator and those bounded molecules are bombarded with photons. After the  
422       action potential, as calcium is extruded from the cell the fluorescence returns to a baseline  
423       level. This is the basic mechanism of fluorescent calcium indicator based imaging.

424       This method has some advantages over electrophysiology as measure of neuronal ensem-  
425       ble activity. Isolating individual neurons is easier and more reliable than identifying unique  
426       spike sources in electrophysiology. Also, spike sorting methods can only detect spikes, but  
427       imaging methods can also detect cells that are not spiking. Cells will emit a baseline level

428 of fluorescence when not firing action potentials. Calcium imaging sites can be re-used for  
429 weeks for longitudinal studies (Chen et al., 2013). Because the fluorescent indicator is deliv-  
430 ered to the cell by adeno-associated viruses, there can be problems with indicator gradients  
431 around the infection site, and expression levels will change in individual cells over weeks  
432 (Tian et al., 2009; Chen et al., 2013). This delivery method can also cause cell pathology,  
433 and nuclear filling (Zariwala et al., 2012), but these problems can be solved by using lines of  
434 transgenic mice (Dana et al., 2014).

435 If the imaging data is collected at a high enough frequency, and the signal-to-noise ratio  
436 of the fluorescence trace is high enough, it should be possible to infer the spike times to some  
437 level of accuracy. For example, the calmodulin based indicator GCaMP6s has a sufficiently  
438 high signal-to-noise ratio that isolated action potentials can be detected and inferred (Chen  
439 et al., 2013). Many spike inference algorithms exist (Vogelstein et al., 2010; Pnevmatikakis  
440 et al., 2016; Friedrich and Paninski, 2016; Pnevmatikakis et al., 2013; Pnevmatikakis et al.,  
441 2014; Deneux et al., 2016; Greenberg et al., 2018), and some of these can perform both cell  
442 isolation and spike detection simultaneously [CITATIONS]

443 but the relationship between spiking and fluorescence change is not fully understood. in-  
444 dicator acts like another calcium buffer, most of the inference algorithms are not biologically  
445 influenced don't include binding dynamics don't include the influence of endogenous buffers  
446 that's why we made the model, we hope it will be useful for this and that

<sup>447</sup> **Chapter 1**

<sup>448</sup> **Sensitivity of the  
spikes-to-fluorescence transform to  
calcium indicator and neuron  
properties**

<sup>450</sup> **451**



452

## *Abstract*

453 Fluorescent calcium indicators such as GCaMP are widely used to monitor neuronal activity.  
454 However the relationship between the fluorescence signal and the underlying action potential  
455 firing is poorly understood. This lack of knowledge makes it difficult for experimenters  
456 to decide between different indicator variants for a given application. We addressed this  
457 problem by studying a basic biophysical model of calcium dynamics in neuronal soma. We  
458 fit the model parameters to publicly available data where GCaMP6s fluorescence and whole-  
459 cell electrophysiological recordings were made simultaneously in the same single neurons.  
460 We systematically varied the model's parameters to characterise the sensitivity of spike train  
461 inference algorithms to the calcium indicator's main biophysical properties: binding rate,  
462 dissociation rate, and molecular concentration. This model should have two potential uses:  
463 experimental researchers may use it to help them select the optimal indicator for their desired  
464 experiment; and computational researchers may use it to generate simulated data to aid design  
465 of spike inference algorithms.

466 

## 1.1 Introduction

467 Although fluorescent calcium indicators such as GCaMP are widely used to monitor neuronal  
468 activity, the relationship between the fluorescence signal and the underlying action potential  
469 firing is imperfect. The fluorescence signal has a low signal-to-noise ratio, and most indi-  
470 cators' kinetics are slow relative to the millisecond-timescale dynamics of the membrane  
471 voltage (example in Figure 1). This makes spike inference difficult. Furthermore, the effects  
472 of the indicator and cell properties on the fluorescence signal are unknown. For example,  
473 genetically encoded indicators can accumulate within neurons over weeks and months (Chen  
474 et al., 2013). Studies using calcium-sensitive fluorescent dyes have shown that indicator con-  
475 centration has substantial effects on the spike-to-fluorescence relationship (Maravall et al.,  
476 2000). Therefore spike rates inferred from GCaMP fluorescence signals may give mislead-  
477 ing results if comparing across imaging sessions. More generally, the poor understanding of  
478 the spike-to-fluorescence transform means experimenters may not know whether to trust the  
479 outputs of spike train inference methods in any given application.

480 Spike trains are usually inferred from the time series of intensity values of one pixel of the  
481 fluorescence image, where the pixel is located at the cell's soma. The problems of identifying  
482 these pixels, and inferring spikes from their time series can solved separately or together.  
483 When attempting to infer spikes, the fluorescence trace is modelled as a linear combination of  
484 calcium concentration dynamics, a baseline calcium concentration, and some Gaussian noise.  
485 The calcium concentration dynamics are modelled as an autoregressive process of degree 1  
486 or 2 with a pulse input corresponding to the spike train, or the number of spikes fired in a  
487 time step. The model includes no dynamics for the fluorescent indicator itself. Furthermore,  
488 in order to make this model into an easily solvable linear programming problem the number  
489 of spikes fired in a timestep is not restricted to non-negative integers but to arbitrary non-  
490 negative values (Vogelstein et al., 2010; Pnevmatikakis et al., 2016; Friedrich and Paninski,  
491 2016; Pnevmatikakis et al., 2013; Pnevmatikakis et al., 2014). More biologically inspired  
492 spike inference models do exist (Deneux et al., 2016), but their fundamentals are very similar.  
493 In this work, we investigated the effect of changing dynamics and buffer concentrations on  
494 the accuracy of the inference algorithms based on these models.

495 The aim of this project was to model the fluorescence traces produced by a fluorescent  
496 calcium indicator in a neuron soma resulting from a specific spike train, given calcium indi-  
497 cator parameters such as binding rate, dissociation rate, and molecular concentration. Such

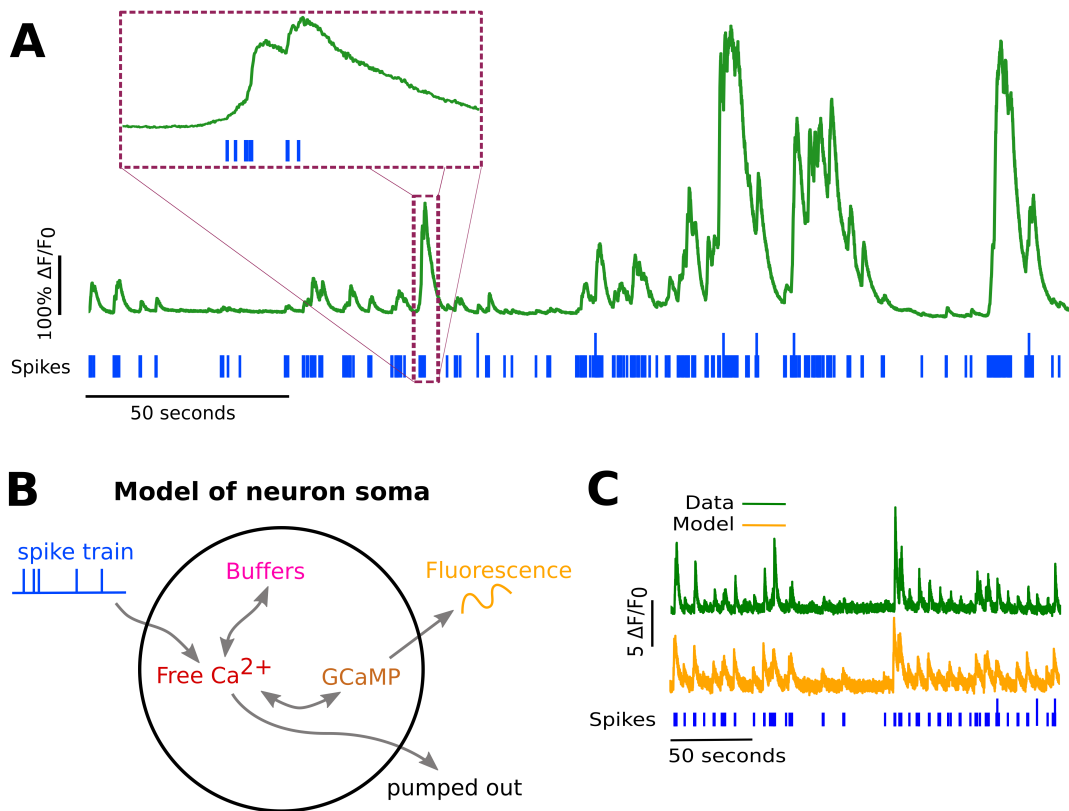


**FIGURE 1.1:**

A: Example spike train (blue) and the corresponding GCaMP6s fluorescence trace (green), data replotted from (Berens et al., 2018). Inset shows zoomed section of traces to highlight slow decay of GCaMP6s fluorescence relative to spike time intervals.

B: Schematic diagram of the neuron calcium and GCaMP computational model.

C: Good visual match of data fluorescence trace (green) and model simulated fluorescence (orange) in response to an identical spike train (blue).

498 a model would allow benchmarking of various spike inference algorithms, and enable under-  
499 standing of how indicator characteristics affect the quality of spike train inference.

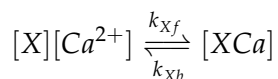
500 The model we developed consisted of free calcium, fluorescent indicator molecules, and  
501 mobile and immobile endogenous calcium buffers. The indicator molecules which were  
502 bound to a calcium molecule could be either excited, i.e. able to release a photon, or relaxed.  
503 In order to reproduce the noise inherent in the data collection, we modelled the release of  
504 photons from the excited indicator bound calcium as a stochastic process.

505 The fluorescence traces produced by the simulation were calibrated to reproduce the  
506 signal-to-noise ratio observed in experimental data. Previously published spike inference  
507 algorithms were then used to infer spike trains from the experimental fluorescence traces and  
508 the modelled fluorescence traces. The parameters of the model were then varied in order to  
509 determine the effect on the system dynamics and the effects on spike inference.

## 510 1.2 Results

### 511 1.2.1 A biophysical computational model can generate accurate fluorescence 512 traces from spike trains

To study the relationship between action potential firing and calcium fluorescence, we built a computational model of calcium dynamics in a neuronal soma. The model consisted of four dynamic variables: the concentration of free calcium, two types of endogenous buffer, and the calcium-sensitive fluorescent indicator. Each of the buffers and the indicator could independently bind and unbind with calcium. These reactions were modelled as



513 where  $X$  is the buffer concentration and  $Ca^{2+}$  is the calcium concentration. Each species  
514 could therefore exist in two states: either bound with calcium or unbound. To model the  
515 imaging process, we also added a third, excited state to the indicator. When in the calcium-  
516 bound state, the indicator could be converted to an excited state, corresponding to the absorp-  
517 tion of a photon. The rate of this excitation process could be interpreted as the intensity of  
518 the light illuminating the sample. Once excited, the species decayed back to the unexcited  
519 state at a fixed rate, corresponding to the spontaneous emission of photons. The total emitted  
520 fluorescence signal was interpreted as proportional to this de-excitation flux. To represent  
521 experimental noise in the photon capture process, we drew a random number of captured

522 photons at each time step from a binomial distribution, parameterised by a number  $p$  that  
523 corresponds to the mean fraction of released photons that are captured.

524 The model had 17 parameters in total describing the molecules' concentrations and re-  
525 action rates (Methods). We set 13 of these parameters to values from the literature. The  
526 remaining 4 parameter values we fit to publicly-available data (Berens et al., 2018), briefly  
527 explained as follows (see Methods for full details). Single neurons from acute rat cortical  
528 slices expressing GCaMP6f were imaged with two-photon microscopy while the membrane  
529 potentials of the somata of the same neurons were simultaneously recorded via whole-cell  
530 patch clamp electrophysiology. In this dataset, the electrical recordings give unambiguous  
531 information about neurons' spike times. To do the parameter fitting, we feed these spike  
532 trains as inputs to the computational model. After running, the model returns a simulated  
533 fluorescence trace. We aimed to find the model parameter values that give the best match  
534 between this simulated fluorescence trace and the real fluorescence time series recorded in  
535 the corresponding neuron. To do this we used a suite of optimisation procedures to jointly  
536 fit both the real neuron's fluorescence time series and power spectrum, which capture com-  
537 plementary information about the spikes-to-fluorescence mapping (Methods). We performed  
538 the fitting procedure independently for each of the 20 neurons in the spikefinder dataset  
539 (<http://spikefinder.org>). After fitting, the model produced realistic-looking fluorescence time  
540 series (Figure 1.1).

541 **1.2.2 Spike inference algorithms perform similarly on real data compared with**  
542 **time series simulated from the model**

543 Researchers often pass the fluorescence time series through a spike inference tool before per-  
544 forming further statistical analyses. These spike inference algorithms take the fluorescence  
545 trace as input and attempt to estimate the neuronal spike train that triggered them (Vogelstein  
546 et al., 2010; Pnevmatikakis et al., 2016; Friedrich and Paninski, 2016; Pnevmatikakis et al.,  
547 2013; Pnevmatikakis et al., 2014; Deneux et al., 2016). Part of our motivation for building  
548 this model was to allow us to ask the question: how do the properties of the cell and the  
549 calcium indicator affect the quality of spike inference? In order to trust the conclusions from  
550 our model, we should first be confident that spike inference from our simulated fluorescence  
551 traces is similar to that from the real data. To test this we passed each of the simulated fluores-  
552 cence traces through three previously published spike inference algorithms, quantified their  
553 performance against the ground-truth electrophysiology data, repeated the procedure for the  
554 real calcium fluorescence time series, and compared the accuracy of the inference processes

555 in all cases. The *true positive rate*, also known as the *recall*, the *sensitivity*, or the *probability of detection* of spike inference varied across the three inference algorithms we tried (p  
556 value and statistical test here). The constrained non-negative matrix deconvolution algorithm  
557 (Pnevmatikakis et al., 2016) (CNMD algorithm) correctly detected approximately 45% of the  
558 true spikes, the OASIS algorithm (Friedrich and Paninski, 2016) correctly detected approx-  
559 imately 35% of the true spikes, and the ML spike algorithm (Deneux et al., 2016) correctly  
560 detected approximately 15% of the true spikes (see figure 1.2). Notably, for two of the three  
561 inference algorithms, the quality of inference was also fairly consistent for individual spike  
562 trains, not just the group means ( $p > 0.05$ , paired t-test). This demonstrates that the models  
563 were generating fluorescence time series that were similarly difficult to decode as the real  
564 data, in ways that were not specific to any one inference algorithm. This is evidence that the  
565 models captured real aspects of the spikes-to-fluorescence transform.

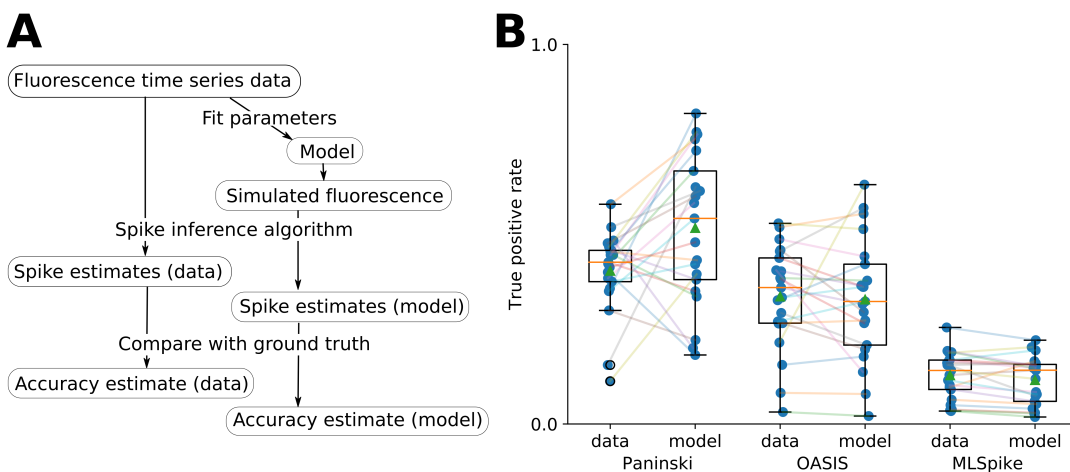


FIGURE 1.2:  
A: Workflow to compare spike inference for real versus simulated fluores-  
cence data.  
B: True positive rates achieved by three different spike inference algorithms  
when applied to observed spike trains, and simulated spike trains. Data  
points overlaid as blue circles. The performance is similar from real and  
simulated data for each of the algorithms.

566

### 567 1.2.3 Relative effects of various buffers to the fluorescence signal

568 One of the benefits of computational models over laboratory experiments is that we can  
569 observe all the variables in the simulation to gain insight into the system's dynamics, which  
570 can be difficult to do in the lab. We plotted the concentrations of the various species over  
571 time for a version of the model fit to one data set, in response to the same train of spikes used  
572 for fitting (figure 1.3). Figure 1.3a shows the absolute values of the species concentrations,

573 summed. Consistent with experimental estimates (Maravall et al., 2000), only a small fraction  
574 ( $\sim 0.1\%$ ) of calcium is free and unbound to any buffer. Of the bound calcium, the vast  
575 majority, ( $\sim 96\%$ ) is bound to the GCaMP indicator. The two types of endogenous buffer  
576 are bound to the remaining calcium ( $\sim 4\%$ ). An influx of calcium from a single spike adds  
577 very little to the total calcium, in relative terms (red line in Figure 3a).

578 When calcium entered the model neuron it was rapidly buffered (Bartol et al., 2015).  
579 However the relative fractions of which buffer molecules bound to the influxed calcium was  
580 dynamic, and changed over time . Figure 1.3 (b-f) shows the time course of the various  
581 species over time in response to a calcium influx event from a single action potential. Cru-  
582 cially, the indicator  $[BCa]$  competed with the endogenous buffers  $[ImCa]$  and  $[ECa]$  – all  
583 three bind calcium on similar timescales. This implies that the timecourse and amplitude of  
584 the  $[BCa]$  variable will also depend on the binding rates and availabilities of the endogenous  
585 buffers. For example if we decreased the concentration of an endogenous buffer, we might  
586 expect both a faster rise time and greater peak amplitude of the  $[BCa]$  signal in response to  
587 a calcium influx event. The slowest component of the decay had a similar time constant for  
588  $[BCa]$ ,  $[ImCa]$  and  $[ECa]$ , which in turn matched the  $[Ca]$  extrusion time constant in our  
589 model ( $\sim 6.29 \times 10^{-22} \text{Ms}^{-1}$ ). This implies that the buffers and the indicator had reached  
590 a dynamic equilibrium and were jointly tracking the free calcium concentration as calcium  
591 was slowly extruded from the cell.

592 Interestingly the excited bound calcium species ( $[BCa^*]$ ) showed a qualitatively different  
593 timecourse in response to a calcium influx event. This concentration is subject to the added  
594 ‘excitation and release’ dynamic, where a certain proportion of the concentration absorbs the  
595 energy from an incoming photon and goes into an ‘excited state’ at each time step. A certain  
596 proportion of the concentration releases a photon and reverts to a ‘relaxed state’ at each  
597 timestep also. This means that the excited bound calcium lags behind the bound calcium  
598 trace. We could think of the excited bound calcium trace as a low pass filtered version of the  
599 bound calcium trace.

600 **1.2.4 Spike inference accuracy is sensitive to indicator properties, and likely  
601 varies within and between cells**

602 The above results imply that the fluorescence signal depends on the relative properties of  
603 both GCaMP and the endogenous buffers. We next used the model to directly ask how  
604 sensitive spike inference was to these components. We focused on three key parameters that

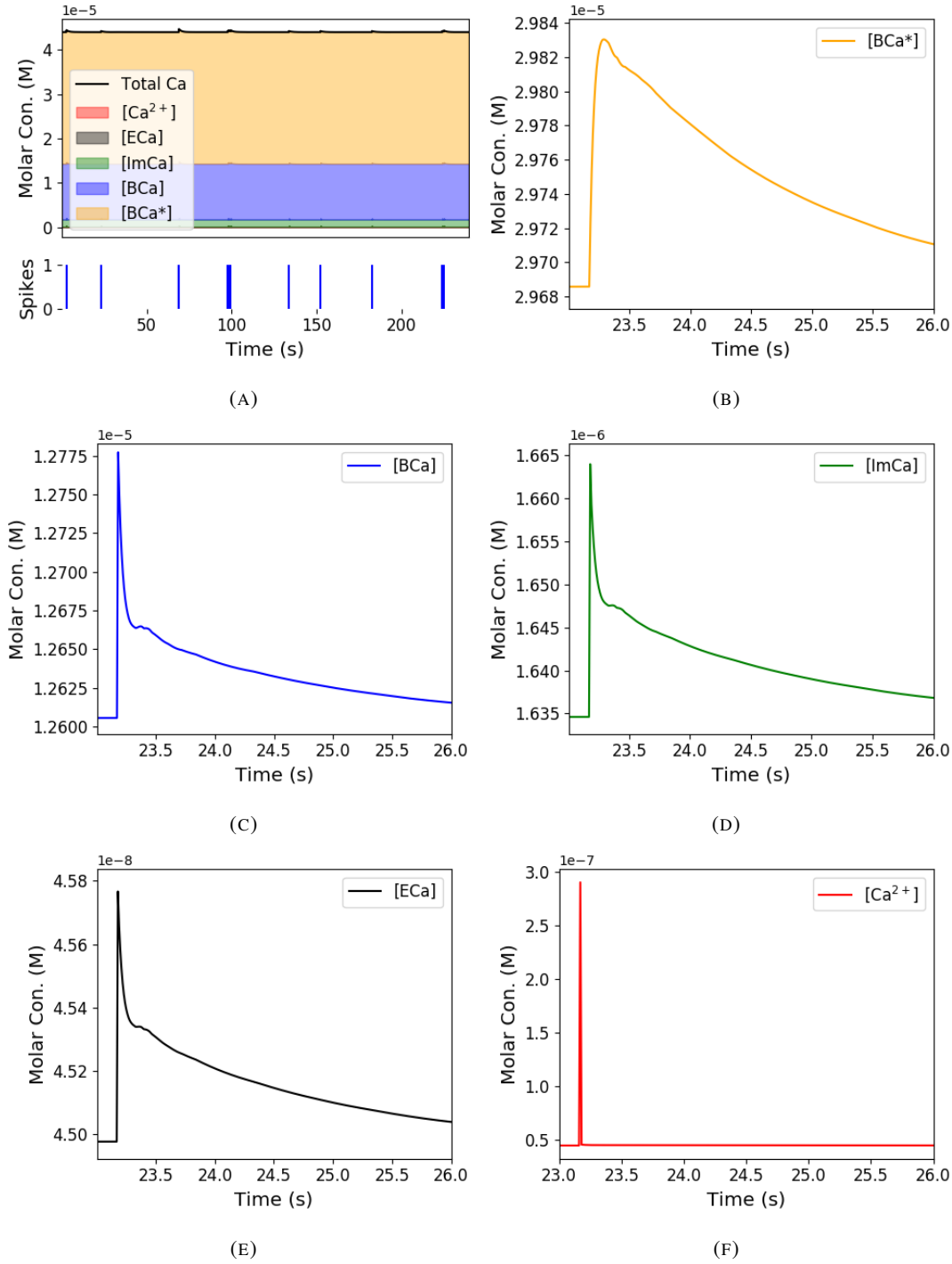


FIGURE 1.3: **Calcium Buffering Dynamics** (a) The proportions of bound and free calcium concentrations within a cell, with the associated spike train. (b)-(f) The dynamics of the concentration of (b) excited indicator bound calcium, (c) indicator bound calcium, (d) immobile endogenous buffer bound calcium, (e) mobile endogenous buffer bound calcium, and (f) free calcium in response to an action potential at  $\sim 23.2$ s.

605 likely vary from cell to cell and experiment to experiment: GCaMP binding kinetics, GCaMP  
606 concentration, and endogenous buffer concentration.

607 Several variants of GCaMP itself have been made that differ in calcium binding kinetics,  
608 baseline fluorescence, fluorescence efficiency, and other factors. For example, GCaMP6f has  
609 a decay time constant of  $\sim 1\text{s}$ , while GCaMP6s has a decay time constant of  $\sim 2\text{s}$  (Chen  
610 et al., 2013). Here we asked how these differences in binding kinetics affect spike inference.  
611 We jointly varied the calcium binding and unbinding rates of the indicator by the same factor  
612 over a range from 100-fold slower to 100-fold faster from the fitted values, and simulated the  
613 fluorescence response for each of the parameter settings in response to the same spike trains  
614 as before (figure 1.4). Notably this manipulation does not affect the indicators affinity, and  
615 therefore would not affect steady-state responses to prolonged changes in calcium. Instead  
616 it is likely to affect its sensitivity to the spike train dynamics. We computed two summary  
617 measures from the simulated fluorescence traces: the signal-to-noise ratio for a single spike  
618 (Methods, section 1.4.6), and the accuracy of spike inference for each of the spike trains. We  
619 observed a reduction in the signal-to-noise ratio and the spike inference quality when we set  
620 the binding and unbinding rates were set to one hundredth of their fitted values, and to one  
621 tenth of their fitted values. When we increased the value of both binding rates, we observed  
622 no change in these measurements. The reduction in both rates lead to smaller increases in  
623 fluorescence in response to an action potential and a longer decay time (figure 1.4a), this  
624 caused the reduction in signal-to-noise ratio. As both rates were increased, the change in  
625  $\Delta F/F_0$  in response to an action potential increased and the decay time decreased slightly,  
626 but the fluorescence trace created by these values was very similar to the trace created by the  
627 fitted values.

628 Second, the overall concentrations of GCaMP often varies from cell to cell. For exam-  
629 ple different cells, even of the same type in the same tissue, can express different levels of  
630 GCaMP, due to proximity to the infection site, or the cell becoming ‘nuclear-filled’ (Tian et  
631 al., 2009; Chen et al., 2013). Also, GCaMP is often used for longitudinal experiments where  
632 the same cells are re-imaged across multiple days or weeks. However since GCaMP expres-  
633 sion typically ramps up over time (Chen et al., 2013), the accuracy of spike inference may  
634 differ across multiple longitudinal recordings in the same cell. We addressed this by varying  
635 the concentration of calcium indicator in the model, simulating spike trains and measuring  
636 signal-to-noise ratio and spike inference accuracy on the resulting fluorescence traces. Both  
637 increasing and decreasing the concentration of the indicator had effects on the fluorescence

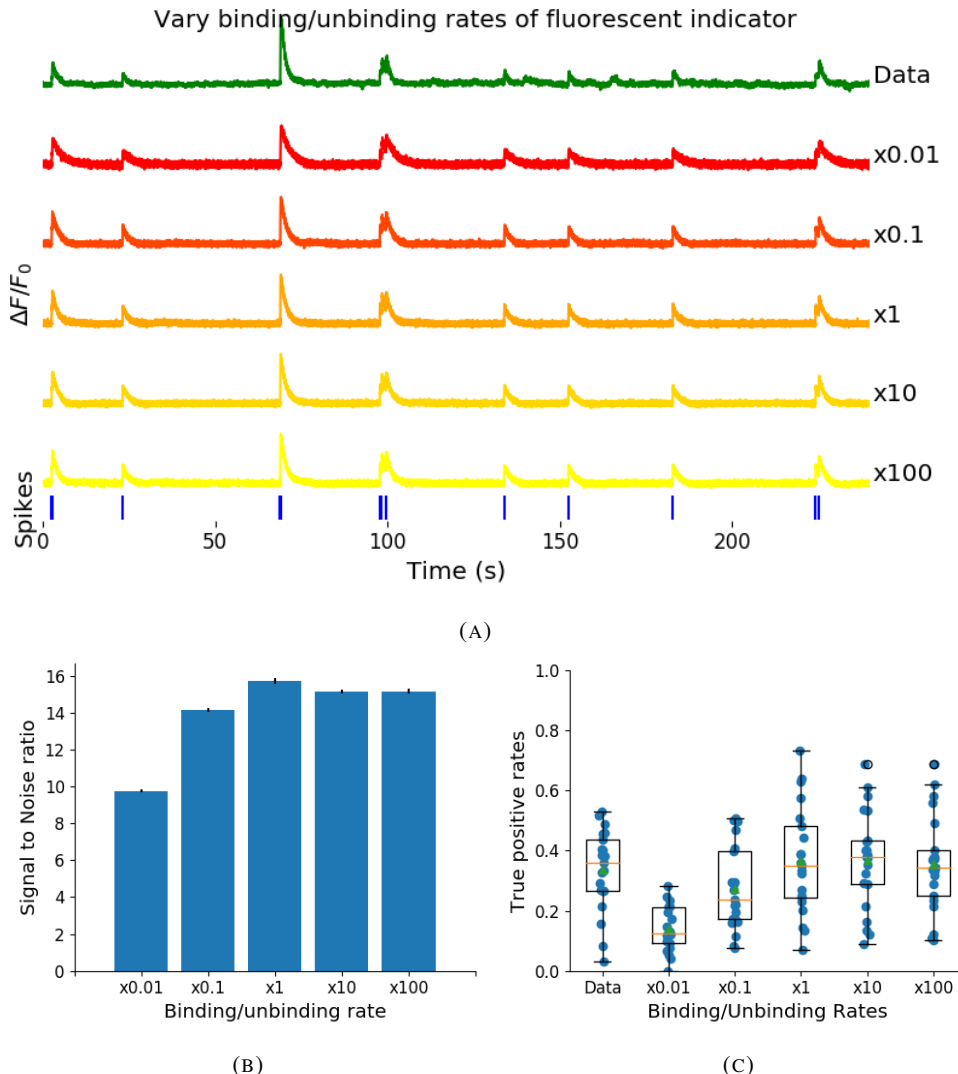


FIGURE 1.4: (a) An example trace for each of the five pairs of values used for the binding and unbinding rates of the fluorescent calcium indicator. (b) The signal-to-noise ratio of the modelled fluorescence traces using each of the four perturbed values, and the experimental value. The SNRs for the two pairs with values lower than the experimental value are lower than the experimental pair or the higher value pairs. (c) The true-positive rates of the deconvolution algorithm's predictions when inferring from the observed data, and inferring from modelled traces using the perturbed and experimental values.

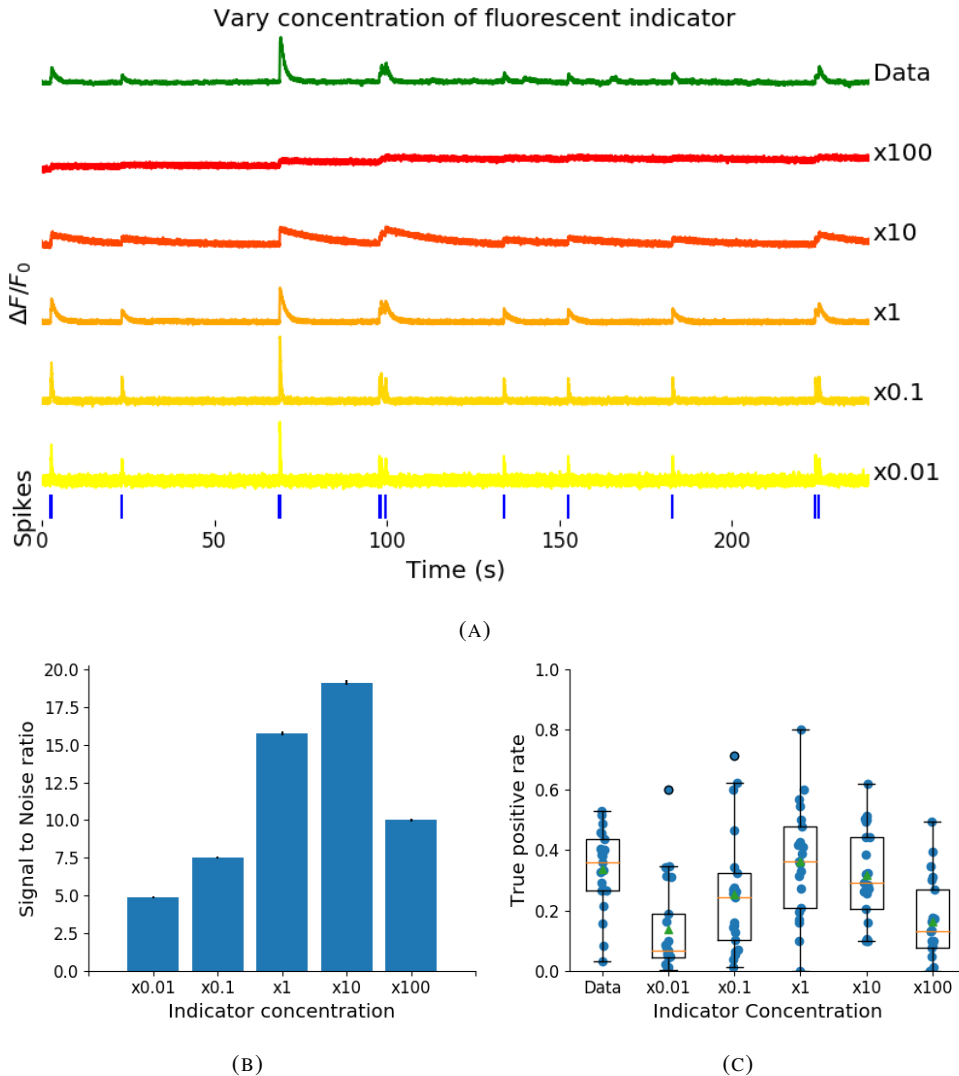


FIGURE 1.5: (a) An example trace for each of the five perturbed values for the concentration of fluorescent calcium indicator. The top two traces are produced by the lower perturbed values, the middle trace is produced by the experimental value, and the lowest two traces are produced when using the higher perturbed values. (b) The signal-to-noise ratio of the modelled fluorescence traces using each of the four perturbed values, and the experimental value. Extreme perturbations of the concentration either above or below the experimental level lowered the SNR. (c) The true-positive rates of the deconvolution algorithm's predictions when inferring from the observed data, and inferring from modelled traces using the perturbed and experimental values. We found that the algorithms performs equally badly on the two most extreme values, and performs equally well on the experimental value, and the next higher perturbed value.

trace, signal-to-noise ratio, and spike inference. The signal-to-noise ratio and spike inference quality decreased with decreased indicator concentration, and both showed a decrease when the indicator concentration was increased to 100 times its fitted value (figure 1.5). The signal-to-noise ratio showed an increase when the indicator concentration was increased to 10 times its fitted value, but there was no corresponding change in the spike inference quality. The decrease in indicator concentration caused a reduction in the increase in  $\Delta F / F_0$  in response to an action potential, and an increase in the decay time of this increase (figure 1.5a). The increase in indicator concentration had the opposite effect, it caused an increase in the change in  $\Delta F / F_0$  in response to an action potential, and a decrease in the decay time.

Third, the concentration and types of endogenous calcium buffers also vary from neuron to neuron, both within and between cell types (Bartol et al., 2015; Maravall et al., 2000; Neher and Augustine, 1992). Since the calcium buffer capacity of neurons is high, around 50-70 (Lee et al., 2000) in excitatory hippocampal pyramidal cells, around 100-250 (Lee et al., 2000) in inhibitory hippocampal pyramidal cells, and 900-200 in Purkinje cells (depending on the age of the subject), these endogenous buffers compete with GCaMP for binding to calcium, and variations in endogenous buffer concentration may affect GCaMP signal and therefore spike inference. To address this we varied the concentration of the endogenous buffer in the model neuron over five orders of magnitude from 0.8 to 8000  $\mu\text{M}$ , simulated calcium fluorescence traces in response to the same set of spike trains, and performed spike inference on the resulting fluorescence time series. Increasing the endogenous buffer concentration had a substantial effect on the GCaMP fluorescence signal, both decreasing its amplitude and slowing its kinetics (figure 1.6(a)). This corresponded with a decrease in both single-spike signal-to-noise ratio (figure 1.6(b)) and spike inference accuracy (figure 1.6(c)). In contrast, decreasing endogenous buffer capacity from the fitted value had little effect on either the GCaMP signal or spike inference (figure 1.6).

1.2.5 Single spike inference accuracy drops for high firing rates, but firing rate  
itself can be estimated from mean fluorescence amplitude

The fluorescence signal recorded from neurons using calcium indicators is typically much slower than changes in membrane potential for two reasons: first, because the calcium and the indicator have slow binding and unbinding kinetics, the signal is a low-pass filtered version of the membrane potential. Second, neuronal two-photon imaging experiments are often performed in scanning mode, which limits their frame rate to  $\sim 10\text{Hz}$  or slower. This implies that multiple spike events that occur close in time might be difficult to resolve from a

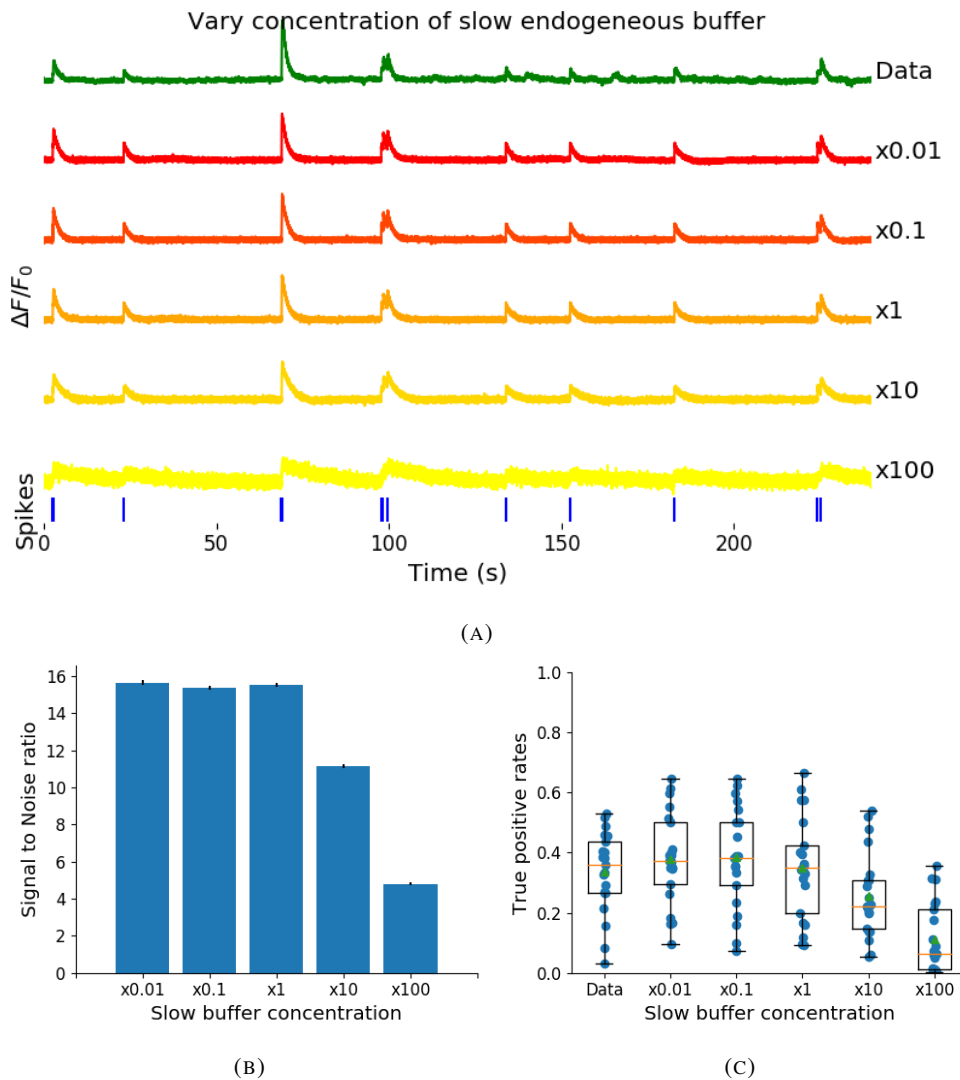
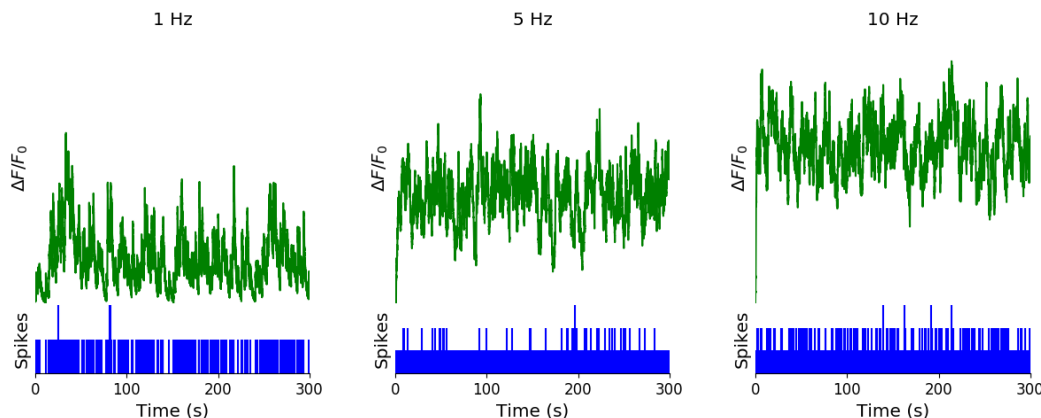


FIGURE 1.6: (a) An example trace for each of the five perturbed values for the concentration of immobile endogenous buffer. (b) The signal-to-noise ratio of the modelled fluorescence traces using each of the four perturbed values, and the experimental value. The lower values for the immobile buffer produce the same SNR as the experimental value. But the higher perturbed values produce fluorescence traces with a lower SNR. (c) The true-positive rates of the deconvolution algorithm's predictions when inferring from the observed data, and inferring from modelled traces using the perturbed and experimental values.

calcium indicator time series. Many cells, especially several types of inhibitory interneurons, fire tonically at rates higher than 10Hz. We used the model to test whether spike inference accuracy depended on the neuron's firing frequency by driving the cell with spike trains sampled from a Poisson processes of varying frequency. We simulated a variable firing rate using an Ornstein-Uhlenbeck process, and simulated the spike trains using a Poisson distribution with its rate taken from this process. Because of the high frequency firing rate of these spike trains, we used the accuracy as the measure of spike inference quality. We simulated 30 spike trains at average firing rate of 1, 5, and 10Hz, and measured the spike inference quality of all these traces. Spike inference accuracy decreased with increasing firing rate, for up to 10Hz Poisson spike trains (figure 1.8(left)). Although, the accuracy remained above 90% for each of the three frequencies. We also plotted the average  $\Delta F/F_0$  as a function of stimulation firing rate. We found that it increased monotonically as a function of firing rate (figure 1.8(right)).

We expected lower spike inference quality as the average spiking frequency increased. Since the fluorescence trace, in some sense, is a low pass filtered version of the spike train, a tightly packed groups of spikes will be more difficult to infer than isolated spikes. However, the increasing amplitude of the fluorescence trace with increasing frequency suggests that some spike inference algorithm could be developed based on this amplitude.



**FIGURE 1.7: Simulating fluorescence traces at different firing rates** Example modelled traces created using simulated spike trains with a mean firing rate of 1Hz (left column), 5Hz (middle column), and 10Hz (right column). Note the difference in amplitude with different mean firing rates.

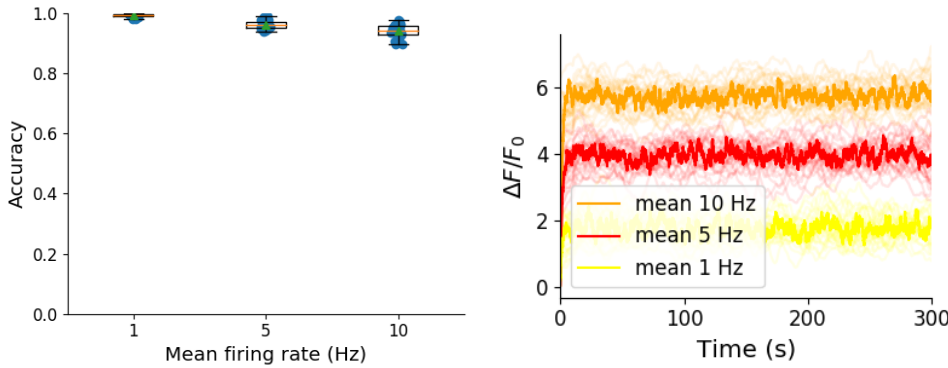


FIGURE 1.8: **Inference quality and  $\Delta F/F_0$  vs Firing rate** (left) The spike inference accuracy when applied to 30 traces created using simulated spike trains with mean firing rates of 1, 5, and 10 Hz. (right) The mean  $\Delta F/F_0$  across those 30 traces for each frequency.

### 689 1.3 Discussion

690 We designed a biophysical model for the changes in free calcium and bound calcium con-  
 691 centrations within a cell soma with a fluorescent calcium indicator. We used this model to  
 692 model the fluorescence trace resulting from a spike train in this cell. We fit the free parame-  
 693 ters of the model by matching the power spectrum and amplitude of fluorescence traces with  
 694 simultaneously measured spike trains. We inferred spikes from real fluorescence traces and  
 695 modelled fluorescence traces, and measured the quality of the spike inference in both cases.  
 696 We found that the spike inference quality was similar in both cases. We perturbed the concen-  
 697 tration of the calcium buffers in the model, and the binding/unbinding rates of those buffers  
 698 in the model, and measured the effect on the signal-to-noise ratio (SNR) of the modelled  
 699 fluorescence traces and the spike inference quality.

700 For the fluorescent calcium indicator, we found that any large perturbation away from  
 701 the experimental value led to a reduction in SNR, and spike inference quality. For the bind-  
 702 ing/unbinding rates, we kept the ratio of these rates constant, but altered their values in paral-  
 703 lel. The lower values caused a reduction in SNR, and a reduction in spike inference quality.  
 704 For the endogenous buffer concentration, an increase above the experimental value caused a  
 705 reduction in SNR and spike inference quality.

706 Although the model produced visually similar time series to the real data, there were a  
 707 few aspects it did not capture. First, the real data featured some low-frequency components  
 708 that did not appear related to the spike events. These were not captured by the models we  
 709 used in this study, but could be added in future by adding a suitable low-frequency term to the  
 710 resulting time series. Second, the real data seemed to have some nonlinearities not captured in

the model, for example the response to two nearby spikes was greater than expected from the linear sum of two single spikes. This may be due to the co-operative binding of Calmodulin to calcium, which gives calmodulin a supra-linear sensitivity to calcium concentration. The model, in contrast behaved much more linearly, but could be extended in future to include such nonlinearities. Third, in the real data the fluorescence peak amplitude seemed to vary from spike to spike, even for well-isolated spike events. However in our model we assumed each spike lead to the same fixed-amplitude injection of calcium to the cell, leading to much greater regularity in fluorescence peak amplitudes. This variability could be added in future versions of the model by making the injected calcium peak a random variable. Fourth, we modelled the soma as a single compartment, but in reality there is likely a non-uniform spatial profile of calcium concentration. This may matter because some endogenous buffers might access calcium right as it influxes from the extracellular space, whereas the majority of the fluorescence signal is more likely coming from the bulk of the cytoplasm. Future models could attempt to model these spatial dependencies to assess whether they affect the overall spike inference procedure.

As well as the optimised parameters, the model has 14 fixed parameters than can be changed to simulate different types of calcium indicators. This model could be used to test the theoretical performance of proposed new types of calcium indicator. The model could also be used by developers of spike inference algorithms to test the effects of changing calcium indicator parameters on spike inference, or to test the affects of changing spiking characteristics on spike inference. For example, high firing rate vs low firing rate, or bursting vs no bursting. Given the increasing amplitude of the fluorescence trace with increasing mean firing rate, it would be possible to build a spike inference algorithm on this principle at least in part.

Our model has already been used as a tool by our colleagues, for simulating fluorescence traces in response to cells that can fire with a continuous rate between 10 and 20Hz, but do not always do so. Our colleagues found that a combination of the amplitude and the variance of the simulated fluorescence trace was the best indicator of firing rate. For example, when a cell was not firing, the amplitude and variance of the fluorescence trace was relatively low. When the cell fired with a low firing rate  $\sim 1\text{Hz}$ , the mean amplitude was still low but the variance of the fluorescence trace was high, and for high firing rate  $\sim 10 - 20\text{Hz}$ , the fluorescence amplitude was high, and the variance was low. In this way, our model may be useful for investigating firing rates underlying real fluorescence traces in response to cells which can fire in these rage ranges.

745 A recent paper by Greenberg et al (2018) described a biophysical model for spike train  
746 inference called the ‘Sequential binding model’. Similar to our model, this model included  
747 parameters for two types of endogenous buffer. But this model also included dynamics for  
748 calcium binding to and unbinding from these endogenous buffers. Furthermore, this model  
749 included dynamics for calcium binding to and unbinding from the four binding sites present  
750 on a GCaMPs6 molecule. In the accuracy measurements specified in that paper, this model  
751 performed better than the MLspike algorithm, which is also partially a biophysically model,  
752 and it performed better than the constrained non-negative deconvolution algorithm. The se-  
753 quential binding model also biophysically interpretable parameters, and its fitted parameters  
754 for quantites such as buffering capacity and calcium influx upon action potential firing fall in  
755 line with experimental values (Greenberg et al., 2018). Biophysical models like this appear  
756 to be the way forward for spike inference algorithms.

## 757 1.4 Methods

### 758 1.4.1 Calcium dynamics model

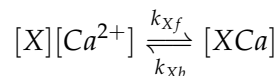
759 We wrote a biophysical model of the calcium dynamics within a cell soma. When a neu-  
760 ron fires an action potential, voltage-dependent calcium ion-channels open up that allow a  
761 current of  $\text{Ca}^{2+}$  to flow into the neuron (Koch, 1999). The increase in the free calcium ion  
762 concentration inside of the cell, along with changes in the concentration of potassium and  
763 sodium, causes the change in cell membrane potential, which must be depolarised. The de-  
764 polarising process consists of free calcium ions leaving the cell through open ion channels,  
765 or binding to molecules within the cell called buffers, or calcium storage by organelles such  
766 as the endoplasmic reticulum. A diagram illustrating the cell, its channels, and its buffers  
767 can be seen in figure 1.1A. There are several different types of calcium buffer, each with  
768 different dynamics and different concentrations within different types of excitable cell. The  
769 fluorescent calcium indicator is another calcium buffer, with the useful property that when it  
770 is bound to a calcium ion, the bound molecule may become excited by a photon and release  
771 a photon in return. This is what creates the fluorescence. After the action potential has taken  
772 place, the free calcium concentration within the cell will return to a baseline level (Maravall  
773 et al., 2000).

774 We modelled the the dynamics of five molecular concentrations,

- 775 • Free calcium ion concentration,  $[\text{Ca}^{2+}]$

- 776 • Fluorescent indicator bound calcium,  $[BCa]$
- 777 • Endogenous mobile buffer bound calcium,  $[ECa]$
- 778 • Endogenous immobile buffer bound calcium,  $[ImCa]$
- 779 • Excited buffered calcium,  $[BCa^*]$

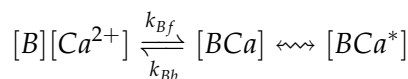
The term ‘buffering’ refers to free calcium ions coming into contact with buffer molecules and binding together. Diagrammatically:



780 where  $[X]$  represents any buffer molecule, and  $k_{X_f}$  and  $k_{X_b}$  represent the binding and un-  
781 binding (dissociation) rates in units of per molar concentration per second ( $M^{-1} s^{-1}$ ) and per  
782 second ( $s^{-1}$ ) respectively. The speed of this chemical reaction is determined by the binding  
783 and unbinding rates.

784 There are a number different endogenous buffers in any neuron. Which buffers are  
785 present, and the buffers’ concentrations vary from cell to cell. In order to capture the ef-  
786 fects of mobile and immobile endogenous buffers without introducing several parameters,  
787 they were modelled as two buffers. One representing mobile buffers and the other represent-  
788 ing immobile buffers. Each with their own binding and unbinding rates.

The fluorescent calcium indicator behaves similarly to the other calcium buffers. The calcium is buffered by the indicator in the same way. But an indicator bound calcium molecule can become excited by absorbing the energy from a photon. An excited indicator bound calcium molecule can then release a photon to go back to its ‘relaxed’ state.



789 The released photons are captured by a photon collector. This gives us the fluorescence trace.  
790 Ignoring the baseline level of free calcium in a neuron, the system of equations we used  
791 to model all of these interactions is as follows:

$$\begin{aligned} \frac{d[Ca^{2+}]}{dt} = & k_{Bb}[BCa] + k_{Eb}[ECa] + k_{Imb}[ImCa] \\ & - k_{Bf}[B][Ca^{2+}] - k_{Ef}[E][Ca^{2+}] - k_{Imf}[Im][Ca^{2+}] \\ & + \beta([Ca_0^{2+}] - [Ca^{2+}]) \end{aligned} \quad (1.1)$$

$$\frac{d[BCa]}{dt} = k_{Bf}[B][Ca^{2+}] - k_{Bb}[BCa] + r[BCa^*] - e[BCa] \quad (1.2)$$

$$\frac{d[ECa]}{dt} = k_{Ef}[E][Ca^{2+}] - k_{Eb}[ECa] \quad (1.3)$$

$$\frac{d[ImCa]}{dt} = k_{Imf}[Im][Ca^{2+}] - k_{Imb}[ImCa] \quad (1.4)$$

$$\frac{d[BCa^*]}{dt} = \eta[BCa] - r[BCa^*] \quad (1.5)$$

where  $[Ca_0^{2+}]$  is the baseline calcium concentration within the cell soma,  $\beta$  is a rate defining how quickly free calcium enters or leaves the cell in the absence of an action potential,  $\eta$  is the excitation rate for indicator bound calcium,  $r$  is the photon release rate for the excited indicator bound calcium, and  $f$  and  $b$  are used to indicate the forward and backward rates for chemical reactions respectively. The excitation rate defines the proportion of indicator bound calcium that becomes excited at each time step. The photon release rate defines the proportion of excited indicator bound calcium that releases a photon and returns to its relaxed state at each time step. An action potential is modelled as a discontinuous increase in the free calcium concentration to an appropriate value (Maravall et al., 2000).

Note that each of the three pairs of binding and unbinding terms in the first equation has a corresponding pair in one of the subsequent three equations. Binding removes a free calcium molecule and adds a bound calcium molecule, and unbinding does the opposite.

When using this model to simulate a fluorescence trace, the system of equations above are first solved over a period of 25s without action potentials. This lets each of the five tracked chemical concentrations reach their steady state. Then we use the given spike train and the parameters to model the fluorescence trace.

Note that since the model has no spatial component, the mobile and immobile buffers only differ in their binding and unbinding rates.

## Photon release & capture

We used a simple model for the photon release. The number of photons released at each time step was controlled by the number of excited indicator bound calcium molecules in the cell and a parameter called the ‘release rate’. The release rate is an optimised free parameter of the model.

As for the photon capture, in two-photon excitation microscopy the photons scattered by the fluorescent indicator get scattered in all directions. Therefore the number of photons detected is stochastic. This made the process for capturing photons the natural source of noise in the system. The number of photons captured, and therefore the intensity of the

819 fluorescence, is modelled using a binomial distribution. The number of photons released was  
820 used as the number of trials. The probability of success, or ‘capture rate’ was a free parameter  
821 of the model that we optimised.

822 **1.4.2 Parameter optimisation**

823 The free parameters of the model are as follows:

824 **Calcium rate,  $\beta$**  Controls how quickly the concentration of free calcium will be driven to  
825 the baseline concentration.

826 **Capture rate,  $p$**  The average proportion of photons captured by the photon detector.

827 **Excitation rate,  $\eta$**  The number of indicator bound calcium molecules that become excited  
828 by photon bombardment at each time step.

829 **Release rate,  $r$**  The number of excited indicator bound calcium molecules that release a  
830 photon at each time step.

831 To optimise the free parameters given a fluorescence trace, we applied the following proce-  
832 dure:

833 1. The frequency power spectrum of the trace was measured.

834 2. The power spectrum was smoothed using a boxcar smoother (aka. sliding average, box  
835 smoother).

836 3. The log of the smoothed power spectrum was measured.

837 4. Use the model to create a modelled fluorescence trace.

838 5. Apply steps 1, 2, and 3 to the modelled fluorescence trace.

839 6. Calculate the root mean squared difference between the log power of the actual fluo-  
840 rescence trace, and the log power of the modelled fluorescence trace.

841 7. Calculate the root mean squared difference between the actual fluorescence trace and  
842 the modelled fluorescence trace.

843 8. Use an optimisation algorithm to reapply this process, attempting to minimize the sum  
844 of the two root mean squared differences at each iteration.

845 Using the root mean squared difference of the log power spectra as part of the objective  
846 function forces the model to match the noise frequency of the actual fluorescence. Using  
847 the root mean squared difference of the traces themselves forces the model to match the  
848 amplitude of the fluorescence trace more accurately.

849 In order to minimise the objective function, a suite of meta-heuristic optimisation (aka.  
850 black-box optimisation) algorithms were implemented on each of the traces in the dataset.  
851 These methods were chosen because they don't require a gradient for the objective function  
852 (gradient-free) and they are particularly useful for minimising stochastic objective functions  
853 like the one we used here. The free parameters were optimised for each individual fluores-  
854 cence trace. The most successful method for each trace was recorded. The method that was  
855 most often successful was probabilistic descent, and the second most successful method was  
856 generating set search. Both of these methods are examples of pattern search. These two  
857 methods were the best optimisers on about 75% of the traces in the dataset.

858 Although this optimisation procedure minimises the value of the optimisation function,  
859 the value never reaches zero for a number of reasons. Firstly, the fluorescence traces carry low  
860 frequency fluctuations that cannot be captured by the model. Secondly, the model assumes  
861 that the process of calcium binding to the fluorescent indicator is linear in time (see equation  
862 1), but there are more complicated dynamics involved here. Fluorescent calcium indicators  
863 are often built upon the calcium binding protein called 'calmodulin'. This protein has four  
864 calcium binding sites. These sites are locally split into two pairs. Each pair has a different  
865 affinity for calcium, and the affinity of the binding sites is affected by the occupancy of  
866 the other binding sites (Kilhoffer et al., 1992). So the calcium to calcium indicator binding  
867 process is non-linear, but the model does not take this into account.

868 **Fixed parameters**

869 As well as the optimised parameters mentioned in section 1.4.2, the model also has thirteen  
870 fixed parameters. Please see table 1.1 for details of these parameters and their values. In  
871 an application of the model, these parameters can be changed in order to model any given  
872 fluorescent calcium indicator.

873 **1.4.3 Julia**

874 The programming language used to write and execute the model was 'Julia'. Julia is a dy-  
875 namic programming language designed for technical computing. Julia was designed specif-  
876 ically to provide a convenient high-level dynamic language similar to MATLAB, or Python,

Parameter	Description	Value	Source
baseline	The baseline concentration of free calcium within the cell soma	$4.5 \times 10^{-8} \text{M}$	(Maravall et al., 2000)
cell radius	The radius of the soma (assumed to be spherical)	$10^{-5} \text{M}$	(Fiala and Harris, 1999)
endogenous	The concentration of endogenous mobile buffer within the cell soma	$10^{-4} \text{M}$	(Faas et al., 2011)
frequency	The frequency at which the spike trains are sampled.	100Hz	
immobile	The concentration of endogenous immobile buffer within the cell soma	$7.87 \times 10^{-5} \text{M}$	(Bartol et al., 2015)
indicator	The concentration of fluorescent indicator within the cell soma	$10^{-4} \text{M}$	(Maravall et al., 2000)
$k_{Bb}$	The unbinding rate of the fluorescent calcium indicator	$160 \text{s}^{-1}$	(Bartol et al., 2015)
$k_{Bf}$	The binding rate of the fluorescent calcium indicator	$7.77 \times 10^8 \text{s}^{-1} \text{M}^{-1}$	(Bartol et al., 2015)
$k_{Eb}$	The unbinding rate of the endogenous mobile buffer	$10^4 \text{s}^{-1}$	(Bartol et al., 2015)
$k_{ef}$	The binding rate of the endogenous mobile buffer	$10^8 \text{s}^{-1} \text{M}^{-1}$	(Bartol et al., 2015)
$k_{Imb}$	The unbinding rate of the endogenous immobile buffer	$524 \text{s}^{-1}$	(Bartol et al., 2015)
$k_{Imf}$	The binding rate of the endogenous immobile buffer	$2.47 \times 10^8 \text{s}^{-1} \text{M}^{-1}$	(Bartol et al., 2015)
peak	The increase in free calcium concentration within the cell induced by an action potential	$2.9 \times 10^{-7} \text{M}$	(Maravall et al., 2000)

TABLE 1.1: **Fixed parameters** A table of the parameters fixed before optimising the model. The values of these parameters could be changed to model different fluorescent calcium indicators.

877 with improved performance. Julia’s type system and Julia’s direct interfaces with C and  
878 Fortran allow this aim to be achieved (Bezanson et al., 2012). The Julia version of the  
879 ‘Sundials’ package for ODE solving was used to solve the system of equations above. The  
880 BlackBoxOptim.jl package for Julia was used to perform the optimisation.

881 **1.4.4 Spike inference**

882 We used spike inference algorithms to compare the quality of spike inference using the mod-  
883 elled traces to the quality of spike inference using the observed traces. We also used the  
884 spike inference algorithms to assess the effect of parameter perturbation on the spike infer-  
885 ence. Three algorithms were used:

886 **Constrained non-negative deconvolution algorithm (aka Pnevmatikakis algorithm)** This  
887 algorithm uses a constrained version of non-negative Weiner deconvolution to infer a  
888 calcium signal and a ‘spiking activity signal’ from the fluorescence trace (Vogelstein  
889 et al., 2010; Pnevmatikakis et al., 2016). The spiking activity signal is a non-negative  
890 vector of real numbers reflecting the cell’s activity rather than an actual spike train. We  
891 inferred a spike train by choosing an optimised threshold for the spiking activity sig-  
892 nal. Whenever the spiking activity signal exceeded that threshold, an action potential  
893 was inferred. The threshold was optimised by minimising the difference between the  
894 number of spikes observed and the number of spikes predicted.

895 **ML-Spike algorithm** This algorithm uses a generalised version of the Viterbi algorithm to  
896 return the spike train that maximises the likelihood of producing the given fluorescence  
897 trace. The Viterbi algorithm is an algorithm for estimating the most likely sequence  
898 of hidden states resulting in a sequence of observed states in a discrete-time finite-  
899 state Markov process (Forney, 1973). In this case, each hidden state is defined by the  
900 presence or absence of an action potential, and each observed state is the value of the  
901 fluorescence trace at each time step. This algorithm assumes that the concentration of  
902 calcium within the cell will decay to a drifting baseline, rather than a fixed baseline  
903 (Deneux et al., 2016).

904 **Online Active Set method to Infer Spikes (OASIS)** This algorithm is once again based on  
905 an auto-regressive model of the fluorescence trace, but can be generalised to any or-  
906 der. The algorithm itself is a generalisation of the pool adjacent violators algorithm  
907 (PAVA) that is used in isotonic regression. The OASIS algorithm works through the

908 fluorescence trace from beginning to end, this combined with the speed of the algo-  
909 rithm means that it could be used for real-time online spike inference (Friedrich and  
910 Paninski, 2016). Given a fluorescence trace, the algorithm will return the most likely  
911 spike train and an inferred denoised fluorescence signal.

912 In order to quantify the quality of spike inference for a given algorithm, we ran that algorithm  
913 on all of the fluorescence traces in dataset number eight of the spike finder datasets. Then we  
914 measured some binary classification measures on the results. These measures included

- 915     ● Accuracy
- 916     ● True positive rate (aka recall, sensitivity, hit rate)
- 917     ● True negative rate (aka specificity)
- 918     ● Precision
- 919     ● Negative predicted value
- 920     ● False negative rate (aka miss rate)
- 921     ● False positive rate (aka fall-out)
- 922     ● False discovery rate
- 923     ● False omission rate

924 In making these measurements, we allowed a tolerance of two subsequent time bins for spike  
925 prediction. For example, the spike train data is a vector of 0s and 1s, with one element for  
926 each time bin. A ‘0’ denotes inactivity, a ‘1’ denotes the presence of at least one action  
927 potential. The inferred spike trains produced by the spike inference algorithms take the same  
928 form. In our analysis, if a spike appeared in the inferred spike train up to two time frames  
929 after a spike in the observed spike train, that spike was considered correctly inferred i.e. a true  
930 positive. However, once a spike in the inferred spike train was matched to a spike from the  
931 observed spike train, the inferred spike could not be matched to another observed spike. To  
932 illustrate, if two spikes were inferred in the two time bins following an isolated observed  
933 spike, the first inferred spike was considered correctly inferred, but the second inferred spike  
934 was considered incorrectly inferred, i.e. a false positive.

935 The most useful measure was the true positive rate. This is because the spiking is sparse  
936 and this measurement is sensitive to the number of spikes observed and inferred, but is not  
937 affected by the true negative or false negative rates. After optimising the parameters for each

938 fluorescence trace we measured the spike inference quality for the observed fluorescence  
939 traces, and compared this to the spike inference quality for the modelled traces.

940 When measuring the spike inference quality for higher frequency spike train (1 – 10Hz),  
941 we used the accuracy as our binary classification measure. At these frequencies the variance  
942 of the fluorescence trace was much higher than for sparser spiking regimes, therefore we  
943 wanted to take into account the number of false negatives inferred by the algorithm.

944 **Comparing spike inference quality**

945 In order to compare spike inference quality we had to use methods for comparing samples.  
946 When comparing the true positive rate distributions arising from two different datasets, or  
947 two different algorithms on the same dataset, we compared the distributions using a paired  
948 t-test.

949 **1.4.5 Perturbation analysis**

950 In order to measure the sensitivity of spike inference to changes in a given model parameter,  
951 we perturbed the parameter and compared the quality of spike inference with the perturbed  
952 parameters to the quality of spike inference with the experimental or optimised parameters.  
953 In order to maximise the possibility of observing a difference due to the perturbation, we  
954 perturbed the chosen parameter by a relatively large amount. For example, the experimen-  
955 tal value for the molar concentration of the fluorescent indicator within the cell was  $10^{-4}\text{M}$   
956 (Maravall et al., 2000). The perturbed values used for this parameter were  $10^{-2}\text{M}$ ,  $10^{-3}\text{M}$ ,  
957  $10^{-5}\text{M}$ , and  $10^{-6}\text{M}$ . The quality of the inference was compared by measuring the true posi-  
958 tive rate for each perturbed value and using a t-test to compare the distributions of the results.

959 This analysis was performed firstly without any optimisation of the free parameters for  
960 use with the perturbed parameters. Then the analysis was performed after the optimised  
961 parameters for each perturbed value were calculated.

962 **1.4.6 Signal-to-noise ratio**

963 To assess the effect of perturbation on the modelled traces, we measured and compared the  
964 signal to noise ratio (SNR) on each of the modelled traces. We calculated the SNR as the  
965 peak change in fluorescence divided by the standard deviation of the baseline fluctuation of  
966 the fluorescence trace (Tada et al., 2014). We measured these values by running the model  
967 on a spike train consisting a long period of inactivity followed by one action potential. We  
968 ran the model on this spike train one hundred times. We then measured the mean change

969 in fluorescence and standard deviation of baseline activity across the one hundred modelled  
970 fluorescence traces, and calculated the SNR.

971 **1.4.7 Data sources**

972 All of the data used in this project was sourced from the ‘Spike Finder’ project ([spikefinder.codeneuro.org](http://spikefinder.codeneuro.org)).  
973 The data consisted of a collection of datasets with simultaneously measured fluorescence  
974 traces and action potentials (Berens et al., 2018).

<sup>975</sup> **Chapter 2**

<sup>976</sup> **Functional networks expand across  
anatomical boundaries as correlation  
time-scale increases**

<sup>977</sup>

<sup>978</sup>



979

## *Abstract*

980 Decades of research has established that correlated spiking plays a crucial role in represent-  
981 ing sensory information. One drawback associated with the recent improvement in recording  
982 technology and consequent large datasets is the difficulty in analysing higher order correla-  
983 tions in large neuronal ensembles. One benefit of these datasets that has not yet been explored  
984 is the opportunity to compare correlations within anatomical regions to correlations across  
985 anatomical regions. In this work, we measured correlations between neurons residing in  
986 nine different brains regions in three awake and behaving mice. Using the these correlation  
987 measurements, we created weighted undirected graph networks and applied network science  
988 methods to detect functional communities in our neural ensembles. We compared these func-  
989 tional communities to their anatomical distribution. We repeated the analysis, using different  
990 timescales for our correlation measurements, and found that functional communities were  
991 more likely to be dominated by neurons from a single brain region at shorter timescales  
992 (< 100ms).

## 993 2.1 Introduction

994 Decades of research has established that correlations play a crucial role in representing sen-  
995 sory information. For example, the onset of visual attention has been shown to have a greater  
996 affect on the correlations in the macaque V4 region than on the firing rates in that region  
997 (Cohen and Maunsell, 2009). Recent findings show that spontaneous behaviours explain cor-  
998 relations in parts of the brain not associated with motor control (Stringer et al., 2019), that  
999 satiety state appears to have a brain wide representation (Allen et al., 2019), and that subject  
1000 exploratory and non-exploratory states are represented in the amygdala (Gründemann et al.,  
1001 2019). So, behavioural states are likely represented across many regions of the brain, not just  
1002 motor related areas. In order to understand the brain, we must understand the interactions  
1003 between neurons and regions.

1004 Because of limitations in recording technology almost all research has explored corre-  
1005 lations between neurons within a given brain region, or within only two regions at most  
1006 (Wierzynski et al., "2009"; Patterson et al., 2014; Girard, Hupé, and Bullier, 2001). Rel-  
1007 atively little is known about correlations between neurons in many different brain regions.  
1008 However, the recent development of ‘Neuropixels’ probes (Jun et al., 2017) has allowed  
1009 extracellular voltage measurements to be collected from multiple brain regions simultane-  
1010 ously routinely, and in much larger numbers than traditional methods. In this project we  
1011 used a publicly-available Neuropixels dataset to analyse correlations between different brain  
1012 regions (Stringer et al., 2019).

1013 A drawback associated with the improvement in recording technology is an increase in  
1014 the difficulty in analysing these data. For example, analysing the  $i$ th order interactions of  
1015  $N$  neurons generally requires estimation of  $N^i$  parameters. A number that becomes astro-  
1016 nomical for large  $N$ . New methods are required for analysing these new large datasets. We  
1017 attempted to address this requirement in this piece of research by applying a cutting-edge  
1018 network science community detection method to neural data.

1019 Another unexplored area of research is the changes in cell interactions at different timescales.  
1020 Studies have shown different timescales for fluctuations in spiking activity (Murray et al.,  
1021 2014), and different time scales for event representation (Baldassano et al., 2017) across dif-  
1022 ferent brain regions. Still most studies focus on quantifying interactions at a given timescale.  
1023 But neurons may interact differently, or may interact with different neurons at different  
1024 timescales. Here we explore correlated communities of neurons at different timescales.

1025 In this work, we measured correlations between binned spike counts from neurons from

1026 nine different regions of the mouse brain. These measurements induced a weighted undi-  
1027 rected graph or network where each neuron is represented by a node, and the strength of  
1028 the connection between these nodes/neurons is the strength of the correlation between their  
1029 spike counts. We then applied newly invented network methods (Humphries et al., 2019)  
1030 to this network to find any community structure, and place the neurons in these correlation  
1031 based communities. Finally, we compared these functional communities to the anatomical  
1032 membership of the neurons.

1033 To investigate the functional communities and their relationship with anatomy at different  
1034 time scales, we repeated these analyses using different length bin widths when binning spike  
1035 times.

1036 To find and analyse functional networks while controlling for the subject’s behaviour, we  
1037 conditioned the binned spike counts on data from a video of the subject’s face, and repeated  
1038 our analysis for spike count correlations (or noise correlations) and signal correlations.

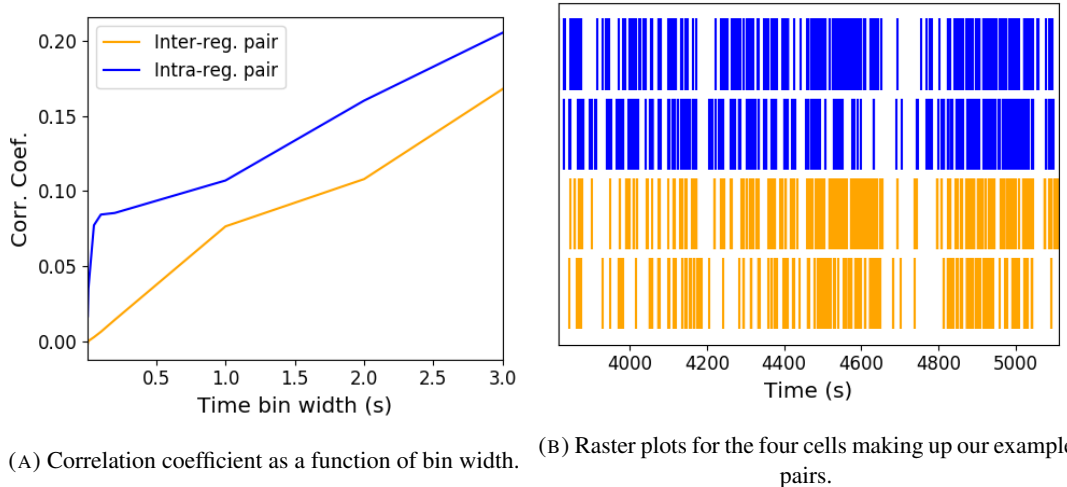
## 1039 2.2 Results

1040 Note that in the following text, we refer to the correlation coefficient between two sequences  
1041 of spike counts from two different cells as the *total correlation*. We refer to the correlation  
1042 between spike counts in response to a certain stimulus as the *spike count correlation* aka  
1043 *noise correlation*, and we refer to the correlation between mean or expected responses to  
1044 different stimuli as the *signal correlation* (Cohen and Kohn, 2011).

1045 The nine different brain regions from which we had data were the caudate putamen (CP),  
1046 frontal motor cortex (FrMoCtx), hippocampus (HPF), lateral septum (LS), midbrain (MB),  
1047 primary visual cortex (V1), superior colliculus (SC), somatomotor cortex (SomMoCtx), and  
1048 thalamus (TH).

### 1049 2.2.1 Average correlation size increases with increasing time bin width

1050 First we inspected the affect of time bin width on total correlations. We know that using short  
1051 time bins results in artificially small correlation measurements (Cohen and Kohn, 2011), so  
1052 we expected to see an increase in correlation amplitude with increasing time bin width. That  
1053 is exactly what we observed. Taking 50 cells at random, we calculated the total correla-  
1054 tion between every possible pair of these cells, using different time bin widths ranging from  
1055 0.005s to 3s. We found that the longer the time bin width, the greater the correlations (see  
1056 figure 2.2a).



(A) Correlation coefficient as a function of bin width. (B) Raster plots for the four cells making up our example pairs.

FIGURE 2.1: (A) An example of the correlation coefficients between two different pairs of cells, one where both cells are in the same brain region (intra-regional pair), and one where both cells are in different brain regions (inter-regional pair). The correlation coefficients have been measured using different time bin widths, ranging from 5ms to 3s. Note the increasing amplitude of the correlations with increasing bin width. (B) A raster plot showing the spike times of each pair of cells.

1057 We also separated the positively correlated pairs from the negatively correlated pairs  
 1058 using the mean correlation of each pair across all bin widths (see section 2.5.2). We found  
 1059 that the positively correlated pairs become more positively correlated with increasing time bin  
 1060 width, and the negatively correlated pairs become more negatively correlated with increasing  
 1061 time bin width (see figures 2.2b and 2.2c).

1062 In figure 2.1a we plot correlations from two example pairs, one pair from within a region,  
 1063 and one pair between regions. It can be seen that the correlation coefficient increases with  
 1064 bin width. The correlations can be observed by eye in the raster plot for these cells in figure  
 1065 2.1b.

1066 When taking the mean across all pairs, the positively correlated pairs dominate in terms  
 1067 of both number of pairs, and amplitude of correlations. Therefore the mean across all pairs  
 1068 is positive.

1069 These results were observed in each of the three mouse subjects from which we had data.

## 1070 2.2.2 Goodness-of-fit for Poisson and Gaussian distributions across increasing 1071 time bin widths

1072 We wanted to investigate if the width of the time bin used to bin spike times into spike counts  
 1073 had an effect on the distribution of spike counts. We used the  $\chi^2$  statistic as a goodness-of-fit  
 1074 measure for Poisson and Gaussian (normal) distributions to the spike count of 100 randomly

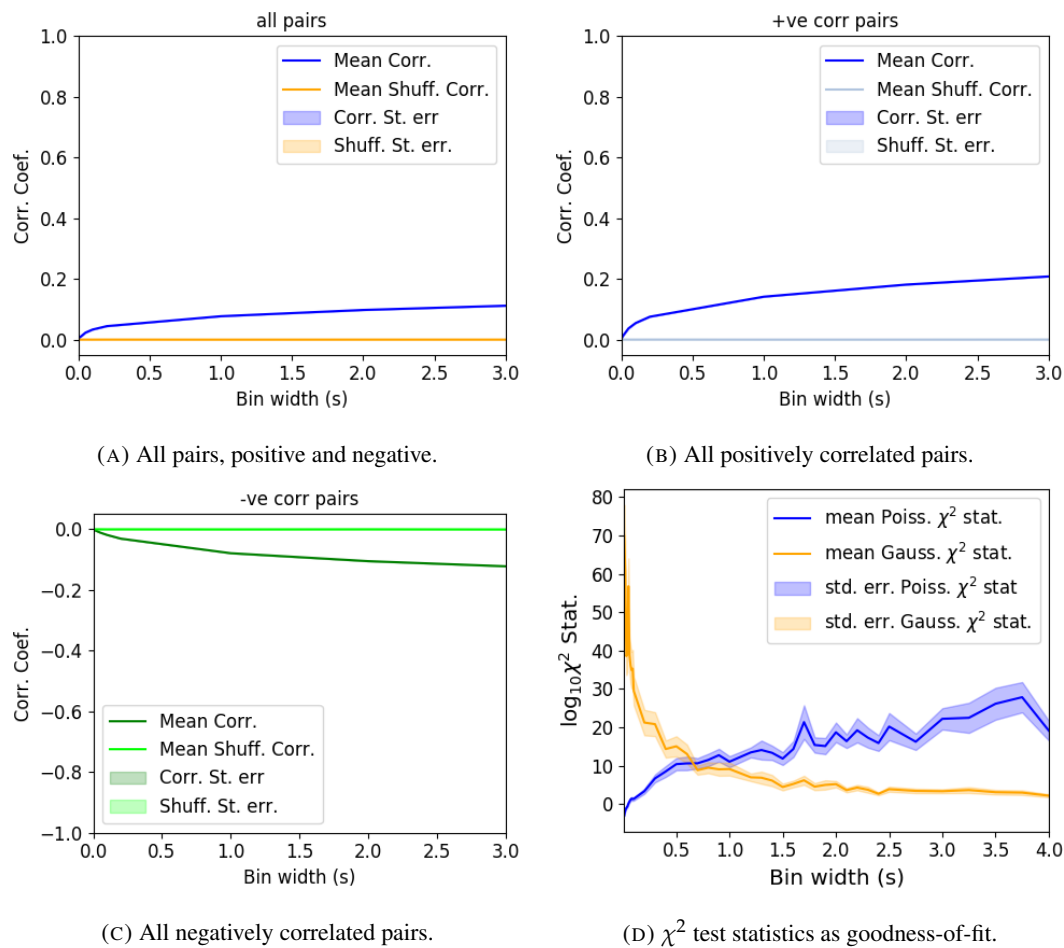


FIGURE 2.2: Mean correlation coefficients measured from pairs of 50 randomly chosen neurons. (A) All possible pairs, (B) positively correlated pairs, and (C) negatively correlated pairs. (D) Mean and standard error of  $\chi^2$  test statistics for Poisson and Gaussian distributions fitted to neuron spike counts.

1075 chosen neurons for a number of bin widths ranging from 0.01s to 4s. For the  $\chi^2$  statistic, the  
1076 higher the value, the worse the fit.

1077 We expected a Poisson distribution to be a better fit for shorter time bin widths because  
1078 spike counts must be non-negative, therefore any distribution of spike counts with mass dis-  
1079 tributed at or close to 0 will be skewed. The distribution of spike counts is more likely to be  
1080 distributed close to 0 when the time bin widths used to bin spike times into spike counts are  
1081 small relative to the amount of time it takes for a neuron to fire an action potential ( $\sim 1\text{ms}$  in  
1082 the case of non-burst firing neurons).

1083 We expected a Gaussian distribution to be a better fit for longer time bin widths, because  
1084 a Poisson distribution with a large rate is well approximated by a Gaussian distribution with  
1085 mean and variance equal to the Poisson rate. Therefore, a Gaussian distribution would ap-  
1086 proximate the mean of a collection of large spike counts, and have more flexibility than a  
1087 Poisson distribution to fit the variance.

1088 We found that that a Poisson distribution is the best fit for shorter time bins less than 0.7s  
1089 in length. Then a Gaussian distribution is a better fit for time bins greater than 0.7s in length  
1090 (see figure 2.2d).

1091 **2.2.3 Differences between and inter- and intra- regional correlations decrease  
1092 with increasing bin width**

1093 We investigated the differences in distribution between inter-regional correlations, i.e. corre-  
1094 lations between neurons in different brain regions, and intra-regional correlations, i.e. corre-  
1095 lations between neurons in the same brain region.

1096 Firstly, we investigated these quantities for all possible pairs of  $\sim 500$  neurons taken  
1097 from across all the 9 brain regions from which we had data. We distributed these neurons as  
1098 evenly as possible across all of the regions, so that cells from one region would not dominate  
1099 our data. We observed that the mean intra-regional correlations were always higher than the  
1100 mean inter-regional correlations for every value of time bin width used. We also observed  
1101 that as the time bin width increased these mean correlations increased and the difference  
1102 between the mean inter-regional and intra-regional correlations grew (see figure 2.3 (Left)).

1103 Stringer et al. (2019) had a similar finding using the same data. They used only one value  
1104 for the time bin width, 1.2s. Using this time bin width to bin spike times and measure total  
1105 correlations, they found that the mean ‘within-region’ correlations were always greater than  
1106 the ‘out-of-region’ correlations (Stringer et al., 2019). The figure from their paper showing  
1107 this result can be seen in figure 2.3 (Right).

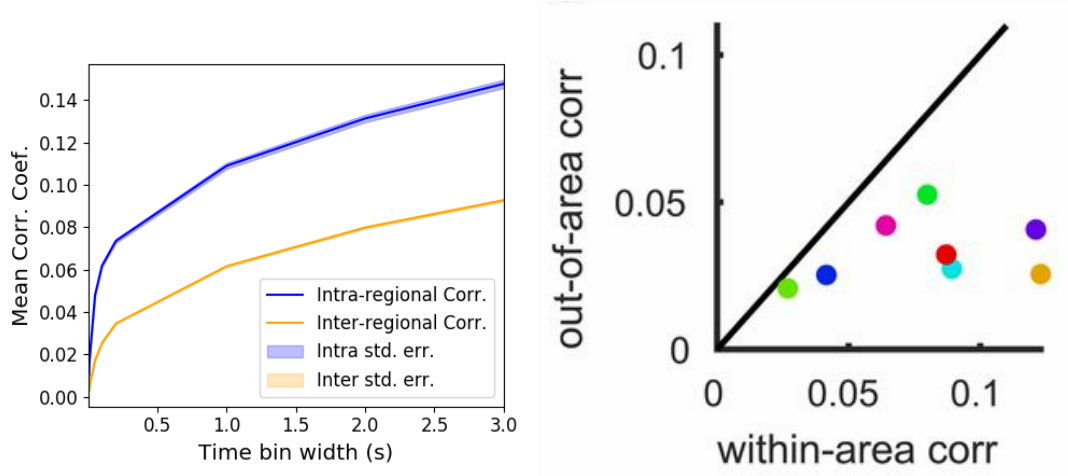


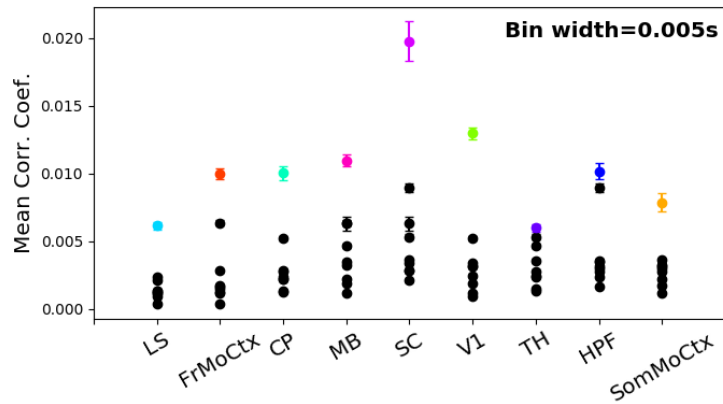
FIGURE 2.3: (Left) The mean intra-region and inter-region correlations using all possible pairs of  $\sim 500$  neurons, spread across 9 different brain regions. (Right) Courtesy of Stringer et al. (2019), mean inter-regional (out-of-area) correlation coefficients vs mean intra-regional (within-area) correlation coefficients for a bin width of 1.2s. Note that the intra-regional coefficients are higher in each case.

1108 Examples of the correlations of one intra-regional pair and one inter-regional pair can be  
 1109 seen in figure 2.1.

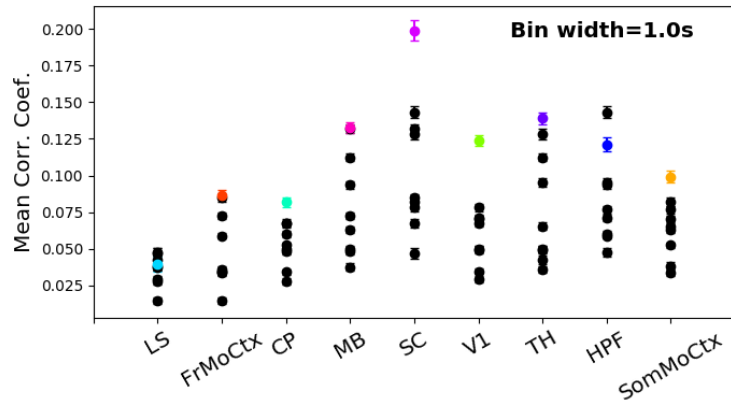
1110 Secondly, we separated those pairs into intra-regional and inter-regional groups. We  
 1111 noted that the mean intra-regional correlations (coloured dots in figures 2.4a and 2.4b) for  
 1112 a given region tended to be higher than the mean inter-regional correlations (black dots in  
 1113 figures 2.4a and 2.4b) involving cells from that region. However, in contrast with our previous  
 1114 result, we noted that the difference between the mean intra-regional correlations and most  
 1115 highly correlated inter-regional correlations reduced as we increased the time bin width (see  
 1116 figures 2.4a and 2.4b). This shows that the mean correlations shown in figure 2.3 are not  
 1117 distributed evenly across all region pair combinations.

1118 Finally, to see these regional mean correlations in a bit more detail, to examine the indi-  
 1119 vidual pair combinations in particular, we displayed these data in a matrix of mean corre-  
 1120 lations (see figure 2.5), showing the mean intra-regional correlations on the main diagonal, and  
 1121 the mean inter-regional correlations off diagonal. Comparing a version of this figure created  
 1122 using a short time bin width of 5ms (figure 2.5a) and a version using a longer time bin width  
 1123 of 1s (figure 2.5b) we observed that the mean intra-regional correlations are always relatively  
 1124 high in comparison to the mean inter-regional correlations, but the mean correlations in some  
 1125 inter-regional pairs are relatively much higher when using the longer time bin width.

1126 This could indicate information being processed quickly at a local or within-region level,  
 1127 and the local representations of this information spreading between regions at longer timescales.

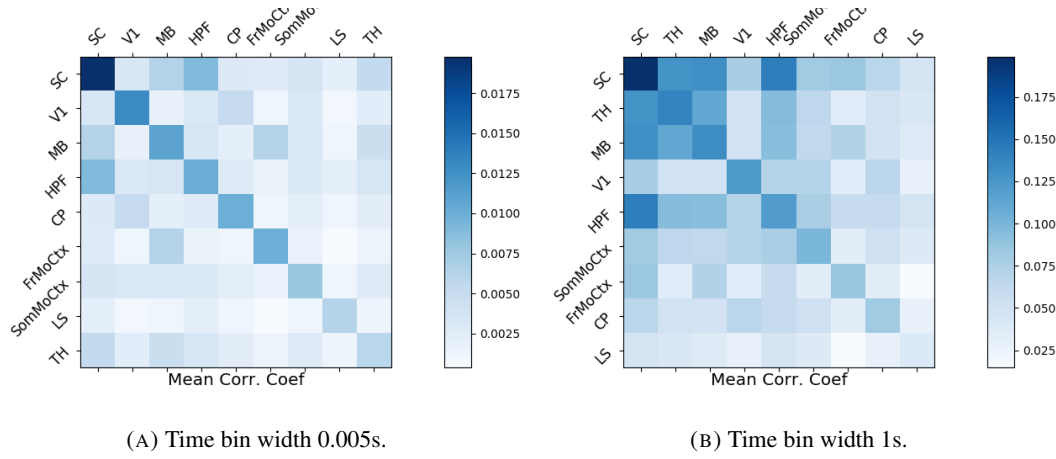


(A) Mean inter-regional and intra-regional correlations using a time bin width of 5ms.



(B) Mean inter-regional and intra-regional correlations using a time bin width of 1s.

FIGURE 2.4: The mean intra-regional correlations (coloured dots) and mean inter-regional correlations (black dots) for a given region, indicated on the x-axis, for different time bin widths. Each black dot represents the mean inter-regional correlations between the region indicated on the x-axis and one other region. (A) shows these measurements when we used a time bin width of 5ms. (B) shows these measurements when we used a time bin width of 1s. Note that the difference between the mean inter-regional correlations and mean intra-regional correlations is smaller for 1s bins.



(A) Time bin width 0.005s.

(B) Time bin width 1s.

FIGURE 2.5: Mean inter-regional (main diagonal) and intra-regional (off diagonal) correlation coefficients. (A) Shows these measurements when spike times were binned using 5ms time bins. (B) Shows the same, using 1s time bins. Note that the matrices are ordered according to the main diagonal values, therefore the ordering is different in each subfigure.

1128 These results were consistent across the three mouse subjects. But, the relative magni-  
 1129 tudes of the mean intra-regional and inter-regional correlations were not consistent. For ex-  
 1130 ample, the region with the highest mean intra-regional correlations when using 1s bin widths  
 1131 for subject one is the superior colliculus (SC), but for subject two it is the midbrain (MB).

1132 **2.2.4 Connected and divided structure in correlation based networks reduces  
 1133 in dimension with increasing bin width**

1134 We used the correlation measurements to create weighted undirected graphs/networks where  
 1135 each node represents a neuron, and the weight of each edge is the pairwise correlation be-  
 1136 tween those neurons represented by the nodes at either end of that edge. We aimed to find  
 1137 communities of neurons within these networks, and compare the structure of these commu-  
 1138 nities to the anatomical division of those neurons. The first step of this process involved  
 1139 applying the ‘spectral rejection’ technique developed by Humphries et al (2019) (Humphries  
 1140 et al., 2019). This technique compares our data network to a chosen null network model, and  
 1141 finds any additional structure in the data network beyond that which is captured in the null  
 1142 network model (if there is any such structure).

1143 By comparing the eigenspectrum of the data network to the eigenspectrum of many sam-  
 1144 ples from the null network model, this technique allows us to estimate the dimensionality of  
 1145 the additional structure in the data network, and gives us a basis for that vector space. It also  
 1146 divides the additional structure into connected structure, and  $k$ -partite (or divided) structure.  
 1147 For example, if our algorithm found two dimensions of additional connected structure, and

1148 one dimension of additional divided structure. We might expect to find three communities,  
1149 that is groups more strongly connected within group than without, and we might expect to  
1150 find bi-partite structure, that is two sets that are more strongly connected between groups  
1151 than within groups.

1152 The technique also finds which nodes contribute to this additional structure, and divides  
1153 our data network into signal and noise networks. The details of spectral rejection and node  
1154 rejection can be found in sections 2.5.5 and 2.5.5 respectively, and a full overview can be  
1155 found in (Humphries et al., 2019).

1156 We chose the sparse weighted configuration model (see section 2.5.5) as our null network  
1157 model. This model matches the sparsity and the total weight of the original network but  
1158 distributes the weight at random across the sparse network.

1159 We applied the spectral rejection method to our networks based on total correlations using  
1160 different values for the time bin width. We observed that for smaller time bin widths, our data  
1161 networks had both  $k$ -partite structure, and community structure. As the width of the time bin  
1162 increased, we found that the  $k$ -partite structure disappeared from our data networks, and the  
1163 dimension of the community structure reduced in two of the three mice from which we had  
1164 data (see figure 2.6).

### 1165 2.2.5 Detecting communities in correlation based networks

1166 We applied the community detection procedure described in section 2.5.5 to our signal net-  
1167 works for our various time bin widths. We detected a greater number of smaller communities  
1168 at shorter time bin widths, and a smaller number of larger communities for longer time bin  
1169 widths (see figure 2.7). This was expected after the results found in section 2.2.4. We found  
1170 more dimensions of additional structure at shorter time bin widths, therefore we found more  
1171 communities at shorter time bin widths.

1172 We also noticed that at short time bin widths the communities detected tended to be  
1173 dominated by cells from one region. Whereas communities existing in networks created  
1174 using wider time bin widths tended to contain cells from many different brain regions. More  
1175 on this in the next section.

### 1176 2.2.6 Functional communities resemble anatomical division at short timescales

1177 In order to quantify the similarity of the communities detected to the anatomical division of  
1178 the cells. We treated both the anatomical division and the communities as clusterings of these  
1179 cells. We then used measures for quantifying the difference or similarity between clusterings

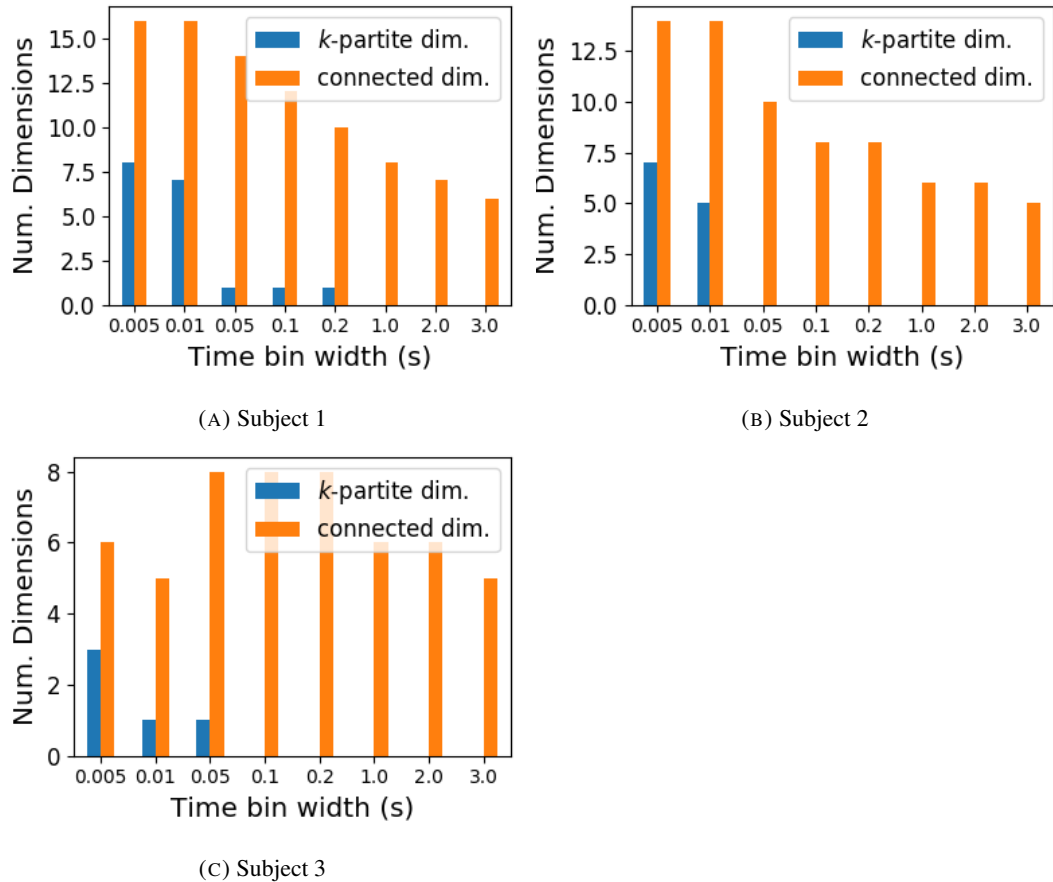


FIGURE 2.6: The number of dimensions in the *k*-partite and connected structure in the correlation based networks beyond the structure captured by a sparse weighted configuration null network model (see section 2.5.5), shown for different time bin widths. Note that the *k*-partite structure disappears for time bin width greater than 200ms for all three subjects. The dimension of the connected structure reduces with increasing bin width for 2 of the 3 subjects (top row).

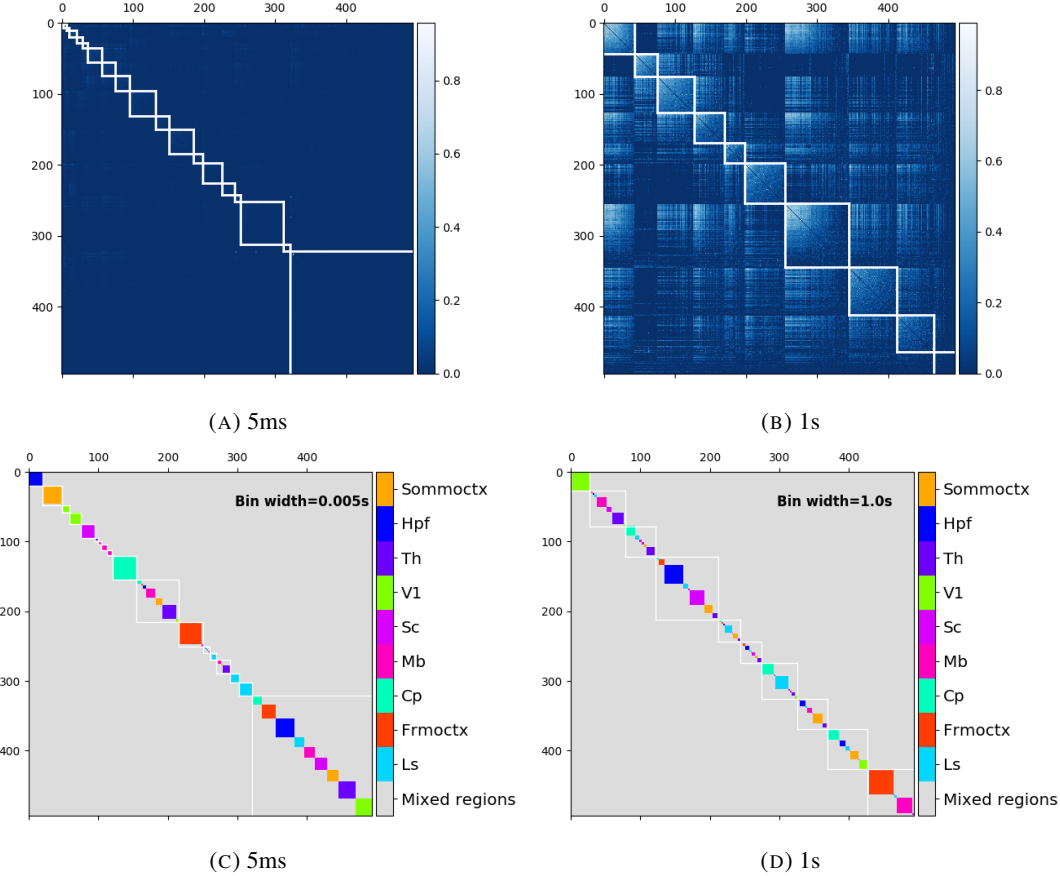


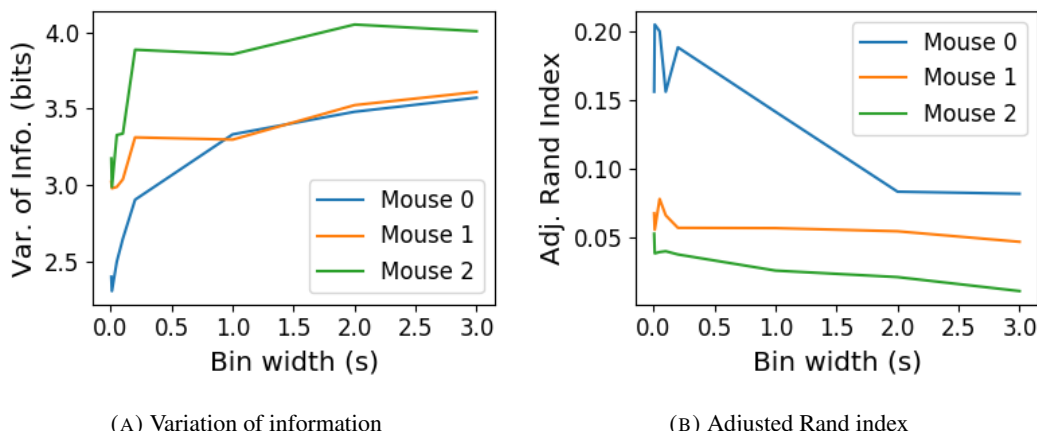
FIGURE 2.7: (A-B) Correlation matrices with detected communities indicated by white lines. Each off main diagonal entry in the matrix represents a pair of neurons. Those entries within a white square indicate that both of those neurons are in the same community as detected by our community detection procedure. Matrices shown are for 5ms and 1s time bin widths respectively. Main diagonal entries were set to 0. (C-D) Matrices showing the anatomical distribution of pairs along with their community membership. Entries where both cells are in the same region are given a colour indicated by the colour bar. Entries where cells are in different regions are given the grey colour also indicated by the colour bar.

to quantify the difference or similarity between the detected communities and the anatomical division. Details of these measures can be found in section 2.5.6 or in (Vinh, Epps, and Bailey, 2010).

We used two different types of measures for clustering comparison; information based measures (see section 2.5.6) and pair counting based measures (see section 2.5.6). We include one example of each in figure 2.8.

The variation of information is the information based measure included in figure 2.8a. This measure forms a metric on the space of clusterings. The larger the value for the variation of information, the more different the clusterings.

The adjusted Rand index is the pair counting based measure included in figure 2.8b. In contrast with the variation of information, the adjusted Rand index is a normalised similarity measure. The adjusted Rand index takes value 1 when the clusterings are identical, and takes value 0 when the clusterings are no more similar than chance.



(A) Variation of information

(B) Adjusted Rand index

FIGURE 2.8: (A) The variation of information is a measure of distance between clusterings. The distance between the anatomical ‘clustering’ and community detection ‘clustering’ increases with increasing time bin width. (B) The adjusted Rand index is a normalised similarity measure between clusterings. The anatomical and community detection clusterings become less similar as the time bin width increases.

Both measures indicated that the detected communities and the anatomical division of the cells were more similar when we used shorter time bins widths (see figure 2.8). This indicates that correlated behaviour in neuronal ensembles is more restricted to individual brain regions at short timescales (< 250ms), and the correlated activity spreads out across brain regions over longer time scales.

1198 **2.2.7 Conditional correlations & signal correlations**

1199 In light of the excellent research of Stringer et al (2019) showing that spontaneous behaviours  
 1200 can drive activity in neuronal ensembles across the visual cortex and midbrain (Stringer et  
 1201 al., 2019), we decided to control for the mouse’s behaviour when performing our analyses.  
 1202 It is possible that our community detection process may be detecting communities across  
 1203 multiple brain regions at longer time scales due to aggregating neuronal activity driven by  
 1204 several spontaneous behaviours occurring during the time interval covered by a given time  
 1205 bin. A time bin of 1s, for example, could contain a spike count where those spikes were driven  
 1206 by different spontaneous behaviours. We aimed to investigate this possibility by applying our  
 1207 community detection analysis to conditional correlation measures.

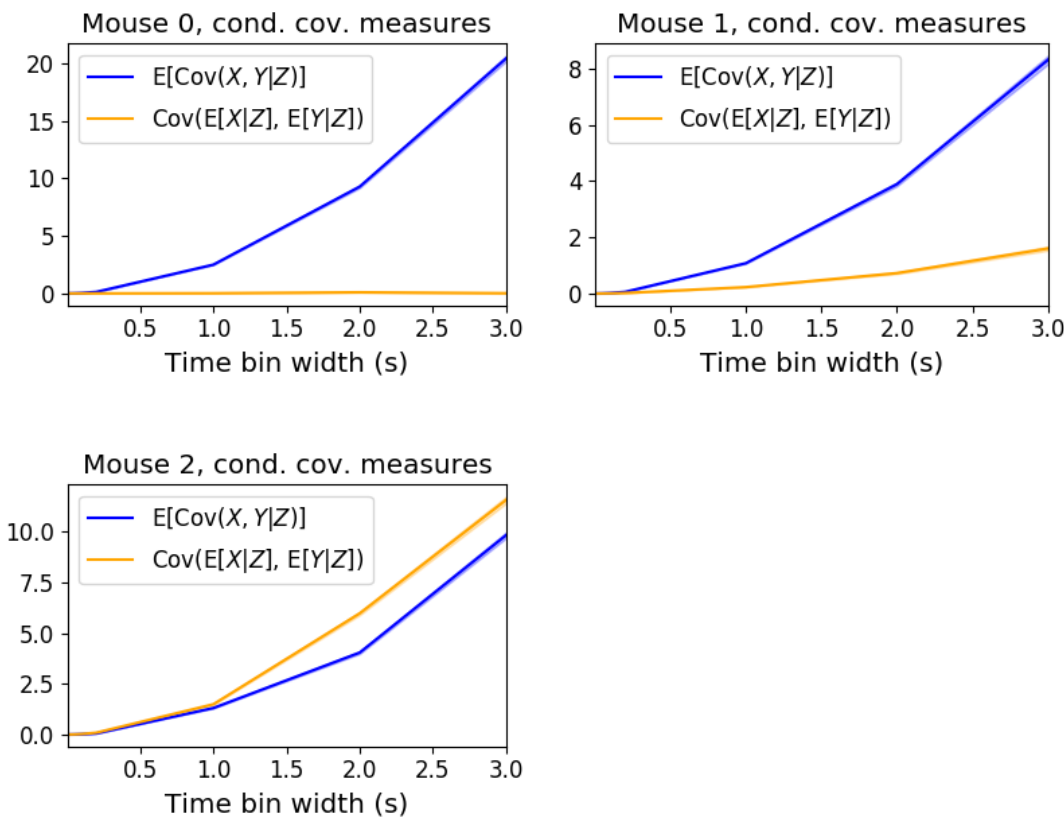


FIGURE 2.9: Comparing the components of the total covariance across different values for the time bin width. We observed a consistent increase in  $E[\text{cov}(X, Y|Z)]$  as the time bin width increased. But we saw different trends for  $\text{cov}(E[X|Z], E[Y|Z])$  for each mouse.

1208 We used the top 500 principal components of a video of the mouse’s face as a measure of  
 1209 the mouse’s behaviour (see section 2.4.2). We modelled the spike counts as a linear combi-  
 1210 nation of the principal components using linear regression with ElasticNet regularisation (see

section 2.5.3). Using this model, we quantified the expected spike count given the mouse’s behaviour  $E[X|Z_1, \dots, Z_{500}]$ .

We used these expected values to measure  $\text{cov}(E[X|Z], E[Y|Z])$ , and we used that value, the covariance  $\text{cov}(X, Y)$ , and the *law of total covariance* (see section 2.5.3) to measure  $E[\text{cov}(X, Y|Z)]$ . Here  $X$  and  $Y$  represent spike counts from individual cells, and  $Z$  is shorthand for the 500 principal components mentioned above. The two components of the covariance,  $\text{cov}(E[X|Z], E[Y|Z])$  and  $E[\text{cov}(X, Y|Z)]$ , represent a ‘signal covariance’ and expected value of a ‘spike count covariance’ respectively, analogous to the signal correlation and spike count correlation (Cohen and Kohn, 2011).

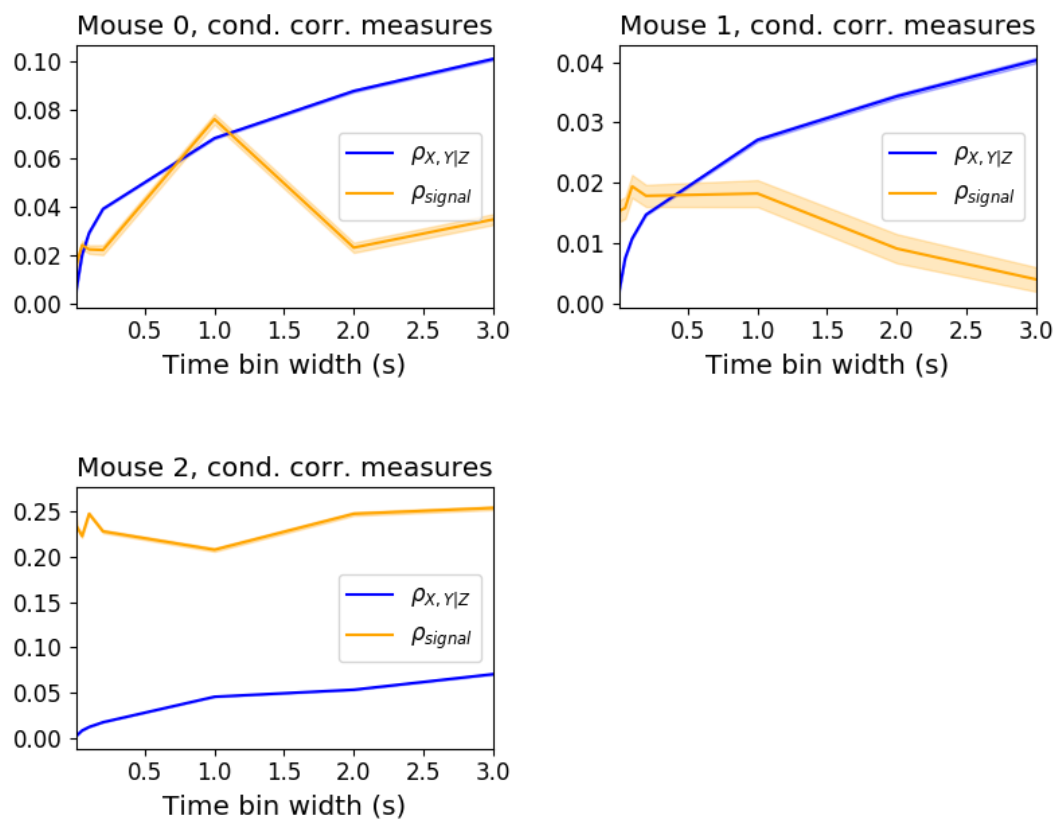


FIGURE 2.10: Comparing the components of the total covariance across different values for the time bin width. We saw a consistent increase in  $\rho_{X,Y|Z}$  as the time bin width increased in all three subjects. But we saw different trends in  $\rho_{\text{signal}}$  for each of the subjects.

We examined the means of these components for different values of the time bin width (see figure 2.9). We observed a consistent increase in  $E[\text{cov}(X, Y|Z)]$  as the time bin width increased. But we saw different trends for  $\text{cov}(E[X|Z], E[Y|Z])$  for each mouse.

Using  $\text{cov}(E[X|Z], E[Y|Z])$  we measured the signal correlation,  $\rho_{\text{signal}}$ , and using  $E[\text{cov}(X, Y|Z)]$  we measured the event conditional correlation,  $\rho_{X,Y|Z}$  (see section 2.5.3 for more details).

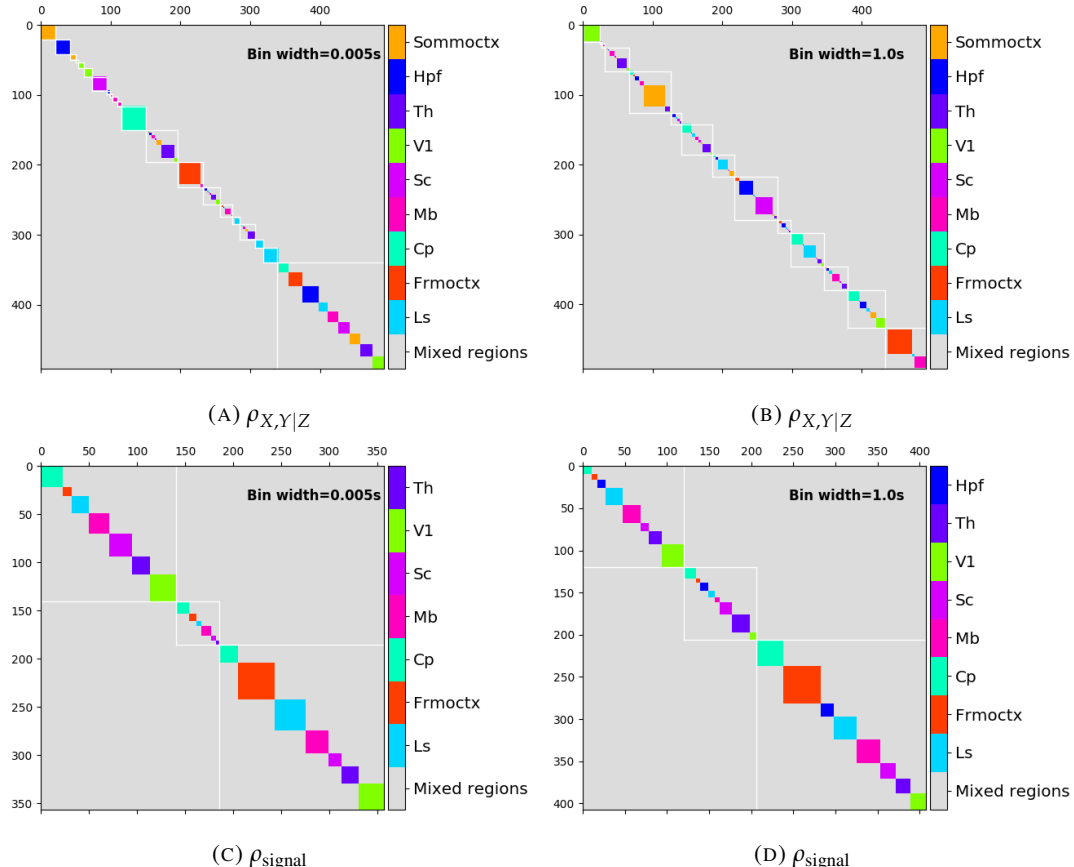


FIGURE 2.11: Matrices showing the regional membership of pairs by colour, and the communities in which those pairs lie. (A-B) Detected communities and regional membership matrix for network based on rectified spike count correlation  $\rho_{X,Y|Z}$ , using time bin widths of 0.005s and 1s respectively. (C-D) Detected communities and regional membership matrix for network based on rectified signal correlation  $\rho_{\text{signal}}$ , using time bin widths of 0.005s and 1s respectively.

1225 We saw a consistent increase in  $\rho_{X,Y|Z}$  as the time bin width increased, this corresponds to  
 1226 the result for  $E[\text{cov}(X, Y|Z)]$ . We observed different trends for  $\rho_{\text{signal}}$  for each mouse, this  
 1227 corresponds to the result for  $\text{cov}(E[X|Z], E[Y|Z])$ .

1228 We applied our network noise rejection and community detection process to networks  
 1229 based on the spike count correlations  $\rho_{X,Y|Z}$  and the signal correlations  $\rho_{\text{signal}}$ . We noted that  
 1230 the community detection on  $\rho_{X,Y|Z}$  behaved similarly to the community detection on the total  
 1231 correlation. We can see this in figures 2.11a and 2.11b. At very short time bin widths, we  
 1232 detect more communities, and those communities often contain cells from one brain region  
 1233 only. At longer time bin widths, we detect fewer communities, and those communities tend  
 1234 to contain cells from multiple brain regions. When we examine the distance between (or  
 1235 similarity between) the anatomical division of the cells, and the detected communities we  
 1236 notice that the two clusterings are more similar at shorter time bin widths (see figure 2.12).

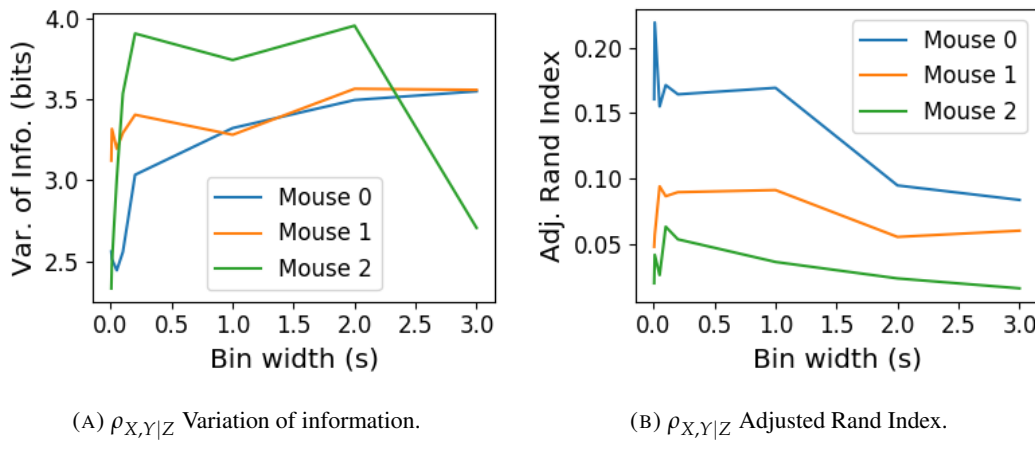
(A)  $\rho_{X,Y|Z}$  Variation of information.(B)  $\rho_{X,Y|Z}$  Adjusted Rand Index.

FIGURE 2.12: Distance and similarity measures between the anatomical division of the neurons, and the communities detected in the network based on the spike count correlations  $\rho_{X,Y|Z}$ . (A) The variation of information is a ‘distance’ measure between clusterings. The distance between the anatomical ‘clustering’ and the community clustering increases as the time bin width increases. (B) The adjusted Rand index is a similarity measure between clusterings. The detected communities become less similar to the anatomical division of the cells as the time bin width increases.

1237 When we applied the network noise rejection and community detection process to the  
 1238 networks based on the signal correlations  $\rho_{\text{signal}}$  we found the number of communities we  
 1239 detected reduced with increasing time bin width. But the number of communities detected  
 1240 was less than that for the total correlations or the spike count correlations. The communi-  
 1241 ties detected always tended to contain cells from multiple regions at both short and long  
 1242 timescales (see figures 2.11c and 2.11d). The communities detected bore very little relation  
 1243 to the anatomical division of the cells. The adjusted Rand index between the community

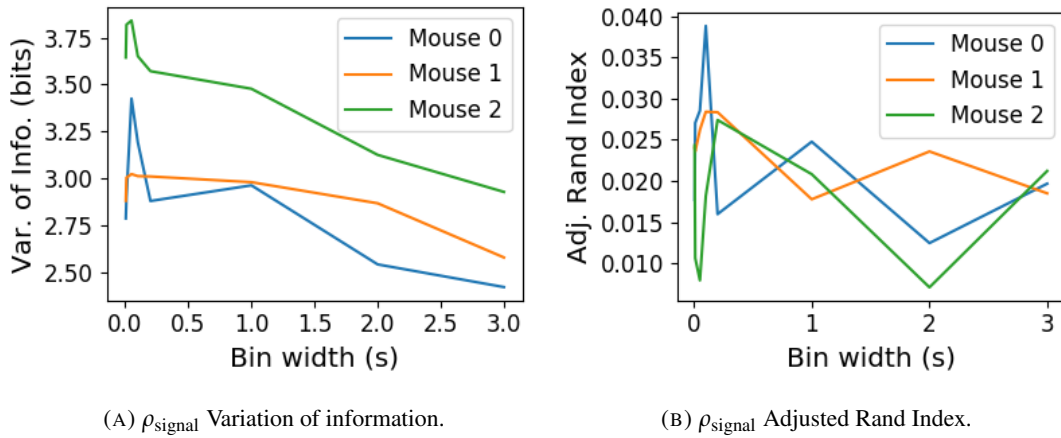
(A)  $\rho_{\text{signal}}$  Variation of information.(B)  $\rho_{\text{signal}}$  Adjusted Rand Index.

FIGURE 2.13: Distance and similarity measures between the anatomical division of the neurons, and the communities detected in the network based on the signal correlations  $\rho_{\text{signal}}$ . (A) The variation of information is a ‘distance’ measure between clusterings. The distance between the anatomical ‘clustering’ and the community clustering increases as the time bin width increases. (B) The adjusted Rand index is a similarity measure between clusterings. The detected communities become less similar to the anatomical division of the time bin width increases.

1244 clustering and the anatomical ‘clustering’ is close to zero for every time bin width (see figure  
 1245 2.13b). This indicates that the similarity between the clusterings is close to chance. We did  
 1246 observe a slight downward trend in the variation of information with increasing bin width  
 1247 (see figure 2.13a), but this is more likely due to a decrease in the number of communities  
 1248 detected rather than any relationship with anatomy.

1249 We also observed that the network noise rejection process rejected some of the cells  
 1250 when applied to the network based on the signal correlations. This means that those cells  
 1251 did not contribute to the additional structure of the network beyond that captured by the  
 1252 sparse weighted configuration model. This is why the matrices in figures 2.11c and 2.11d are  
 1253 smaller than their analogues in figures 2.11a and 2.11b.

## 1254 2.2.8 Absolute correlations and negative rectified correlations

1255 At the moment, the network noise rejection protocol can only be applied to weighted undi-  
 1256 rected graphs with non-negative weights. This meant that we had to rectify our correlated  
 1257 networks before applying the network noise rejection and community detection process. We  
 1258 wanted to investigate what would happen if instead of rectifying the correlations, we used the  
 1259 absolute value, or reversed the signs of the correlations and then rectified.

1260 When we used the absolute value of the correlations, we found very similar results to

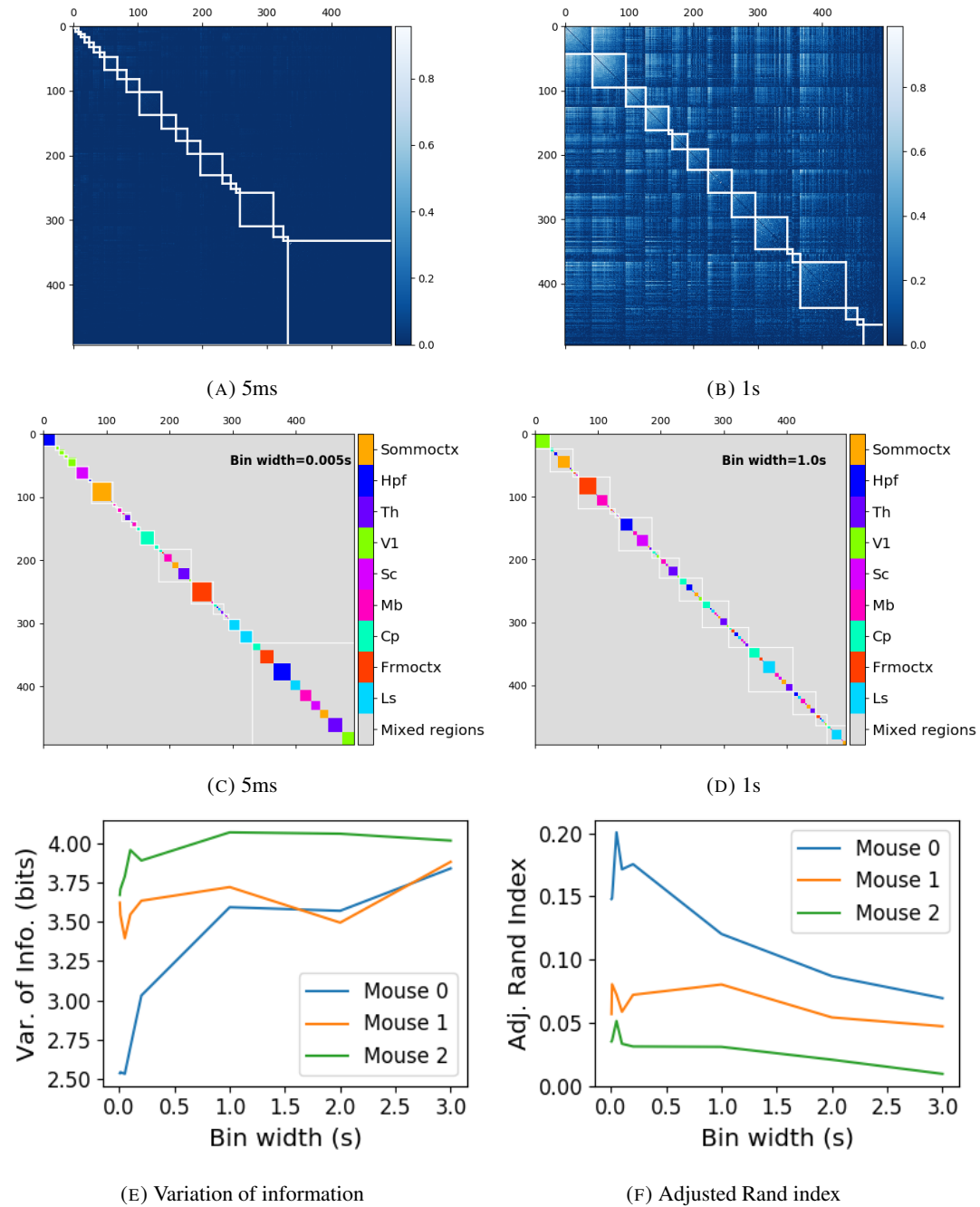


FIGURE 2.14: (A-B) Absolute correlation matrices with detected communities indicated by white lines. These communities are based on the absolute value of the total correlation between each pair of cells. Those entries within a white square indicate that both of those neurons are in the same community. Matrices shown are for 5ms and 1s time bin widths respectively. Main diagonal entries were set to 0. (C-D) Matrices showing the anatomical distribution of pairs along with their community membership. Regional membership is indicated by the colour bar. (E) Variation of information between the anatomical division of the cells, and the detected communities. (F) Adjusted Rand index between the anatomical division, and the detected communities.

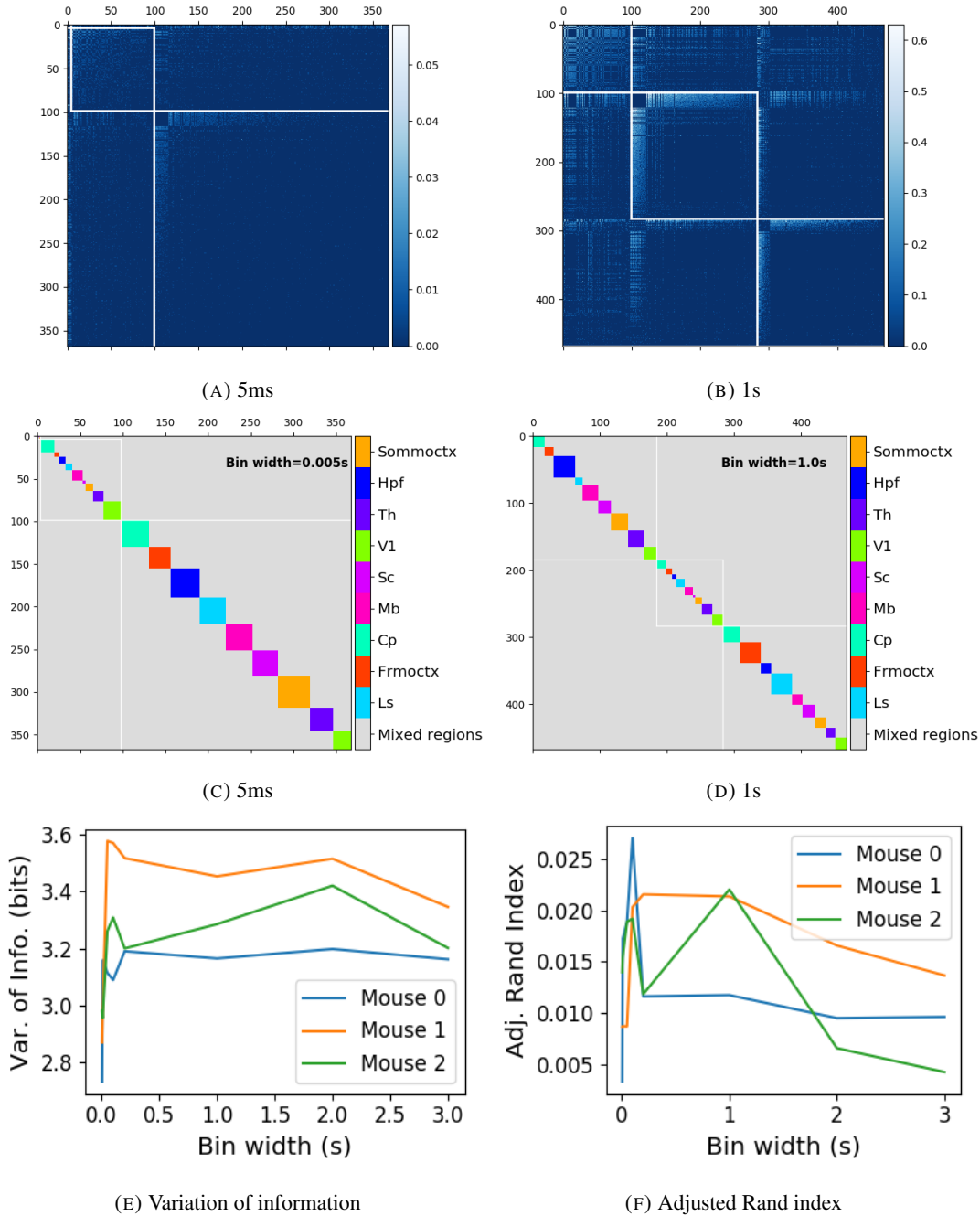


FIGURE 2.15: (A-B) Sign reversed rectified correlation matrices with detected communities indicated by white lines. Those entries within a white square indicate that both of those neurons are in the same community. Matrices shown are for 5ms and 1s time bin widths respectively. Main diagonal entries were set to 0. (C-D) Matrices showing the anatomical distribution of pairs along with their community membership. Regional membership is indicated by the colour bar. (E) Variation of information between the anatomical division of the cells, and the detected communities. (F) Adjusted Rand index between the anatomical division, and the detected communities.

1261 those shown above for the rectified total correlations and the rectified spike count corre-  
1262 lations. We detected more communities using shorter bin widths, and these communities  
1263 were more similar to the brain's anatomy than those communities detected using a longer bin  
1264 width (see figure 2.14). The only exception being that we detected more communities. This  
1265 could indicate that we detected both positively and negatively correlated communities, but  
1266 we haven't done any further investigation so we cannot say for sure.

1267 When we used the sign reversed rectified correlated networks, we tended to find fewer  
1268 communities. Each community contained cells from many different anatomical regions, at  
1269 both long and short bin widths (see figures 2.15a, 2.15b, 2.15c, 2.15d). The communities  
1270 bore little relation to the anatomical distribution of the cells, this can be seen in figure 2.15f,  
1271 the values close to zero indicate that the similarity between the two clusterings are around  
1272 chance level. This indicates that there was not much structure in the negatively correlated  
1273 networks beyond that captured by the sparse weighted configuration model.

## 1274 2.3 Discussion

1275 It is well established that the brain uses correlated behaviour in neuronal ensembles to repre-  
1276 sent the information taken in through sensation (Cohen and Maunsell, 2009; Litwin-Kumar,  
1277 Chacron, and Doiron, 2012; deCharms and Merzenich, 1996). However, most studies that  
1278 examine the nature of these correlations in-vivo, study an ensemble of cells from only one or  
1279 two brain regions (Cohen and Kohn, 2011; Wierzynski et al., "2009"; Patterson et al., 2014;  
1280 Girard, Hupé, and Bullier, 2001). Furthermore, recent results have shown that behaviour can  
1281 drive correlated activity in multiple brain regions, including those not normally associated  
1282 with motor control (Stringer et al., 2019; Gründemann et al., 2019; Allen et al., 2019). In this  
1283 study, we utilised one of the newly recorded large datasets containing electrophysiological  
1284 recordings from multiple brain regions simultaneously. We investigated correlated behaviour  
1285 in these different brain regions and we investigated correlated behaviour between neurons in  
1286 different regions, during spontaneous behaviour.

1287 A number of studies have found that the timescale of correlated behaviour induced by a  
1288 stimulus can be modulated by the stimulus structure and behavioural context. For example,  
1289 the spike train correlations between cells in weakly electric fish are modulated by the spa-  
1290 tial extent of the stimulus (Litwin-Kumar, Chacron, and Doiron, 2012), and neurons in the  
1291 marmoset primary auditory cortex modulate their spike timing (and therefore correlation) in  
1292 response to stimulus features without modulating their firing rate (deCharms and Merzenich,

1293 1996). Furthermore, the width of the time bins over which spike counts are measured has  
1294 been shown to have an effect on the magnitude of those correlations (Cohen and Kohn, 2011).  
1295 Despite this, very little research has been done comparing correlation measures from the same  
1296 dataset at different timescales. We investigated this by varying the time bin width used to bin  
1297 spike times into spike counts from as short as 5ms up to 3s.

1298 In order to further investigate the effect of these correlations at different timescales, we  
1299 regarded our neuronal ensemble as a weighted undirected graph, where each neuron is rep-  
1300 resented by a node, and the weight on each edge is the correlation between the neurons  
1301 connected by that edge. We then applied a novel clustering method from network science  
1302 (Humphries et al., 2019) to identify communities in these networks. Communities in a net-  
1303 work graph refer to sets of nodes that are more strongly connected to each other than the  
1304 nodes outside of their set. Another way to put this is to say that the nodes in a community  
1305 are more strongly connected than *expected*. What connection strength might be expected is  
1306 defined by a null network model. We chose a null network model that matched the sparsity  
1307 and total strength of our correlation based data networks. So, if two cells were in the same  
1308 community, those cells were more correlated than would be expected given the correlation  
1309 strength of their ensemble.

1310 These networks, and the community detection process, were completely agnostic of the  
1311 anatomical division of the cells in our ensemble. When we compared the detected commu-  
1312 nities with the anatomical division of the cells using distance and similarity measures for  
1313 clusterings, we found that the detected communities were more similar to the anatomical  
1314 division at shorter timescales. That is, when we used a wider time bin to count spikes, and  
1315 computed pairwise correlations with these spike counts, the correlated communities tended to  
1316 exist within anatomical regions at shorter timescales, and tended to span anatomical regions  
1317 at longer timescales. This could reflect localised functional correlations at short time scales  
1318 rippling outwards across brain regions at longer timescales. The brain may be processing  
1319 some information quickly locally, and carrying out further, perhaps more detailed, represen-  
1320 tation over a longer timescale across many regions using the representations that were just  
1321 built locally.

1322 These changes in communities across timescales could also be driven by the anatomy  
1323 of the individual cells. For example, it may simply take longer to transmit action potentials  
1324 over longer distances, hence correlated activity over longer timescales will exist between  
1325 anatomical regions, rather than within. However, the switch to almost exclusively multi-  
1326 regional functional networks at 1s bin widths, rather than a mixture of multi-region, and

single-region suggests that the inter-regional correlations either overpower, or inhibit the local correlations. So there may be more at play than just timescales.

We acknowledged that the region spanning correlated communities that we detected at longer time scales could exist due to collating activity driven by distinct spontaneous activities. In order to account for this, we modelled the spike counts as a linear function of the top 500 principal components of a video of the mouse's face filmed simultaneously with the electrophysiological readings. We applied our network noise rejection and community detection process to the weighted undirected networks formed by the spike count correlations (or noise correlations) and the signal correlations that we calculated using our model. For the spike count correlation networks, we found much the same results as for the total correlations as described above. For the signal correlations, the communities detected in these networks bore little relation to the anatomical division of the cells. Recent findings have shown that behavioural data accounts for correlations in many brain regions that would otherwise be dismissed as noise (Stringer et al., 2019), our finding to shows that these correlations are still governed by the timescale division between local communication and across-region communication.

There is a lot of room for further investigation based on this research. For a start, the data that we used here were collected from nine different regions in the mouse brain, but none of these regions were part of the somatosensory cortex. Given that a mouse experiences so much of its environment through its sense of smell, some data from this region would be interesting to investigate. On the same theme, the mice in the experiment from which the data were collected were headfixed and placed on a rotating ball, but were otherwise behaving spontaneously. Had these mice been exposed to a visual, aural, or olfactory stimulus, we could have examined the responses of the cells in the brain regions corresponding to vision, hearing, and olfaction, and compared these responses to the responses from the other brain regions. Furthermore, we could have investigated the interaction between the sets of responses.

Another space for further investigation is the community detection. The algorithm that we used here never detects overlapping communities. But functional communities could indeed have overlaps. Clustering methods that detect overlapping clusters do exist (Baadel, Thabtah, and Lu, 2016). Applying one of those algorithms could yield some interesting results. Also, the community detection algorithm that we used here cannot process graphs with negative weights, this forced us to separate positive and negative correlations before applying our network noise rejection and community detections process, or use the absolute value of our

1361 correlations. A community detection algorithm that can work on weighted undirected graphs  
1362 with negative weights could yield some interesting results here.

## 1363 2.4 Data

1364 The data that we used in this project were collected by Nick Steinmetz and his lab members  
1365 (Stringer et al., 2019).

### 1366 2.4.1 Brain regions

1367 Neuropixels probes were used to collect extracellular recordings (Jun et al., 2017) from three  
1368 different mice. The mice were awake, headfixed, and engaging in spontaneous behaviour.  
1369 The mice were of different sexes and different ages. One mouse was ‘wild-type’, the others  
1370 were mutants. Details as follows:

- 1371 1. male, wild type, P73.
- 1372 2. female, TetO-GCaMP6s, Camk2a-tTa, P113
- 1373 3. male, Ai32, Pvalb-Cre, P99

1374 Eight probes were used to collect readings from 2296, 2668, and 1462 cells respectively.

1375 Data were collected from nine brain regions in each mouse:

- 1376 • Caudate Putamen (CP)
- 1377 • Frontal Motor Cortex (Frmoctx)
- 1378 • Hippocampal formation (Hpf)
- 1379 • Lateral Septum (Ls)
- 1380 • Midbrain (Mb)
- 1381 • Superior Colliculus (Sc)
- 1382 • Somatomotor cortex (Sommocortex)
- 1383 • Thalamus (Th)
- 1384 • Primary visual cortex (V1)

1385 Readings were continuous and lasted for about 1 hour (Stringer et al., 2019). Locations of  
1386 each of the probes can be seen in figure 2.16.

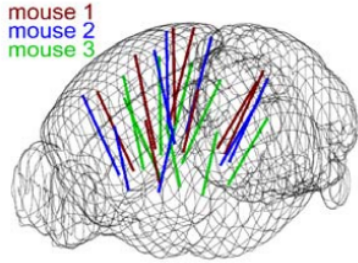


FIGURE 2.16: **Probe Locations:** The locations of the probes in each of the three mouse brains (Stringer et al., 2019).

### 1387 2.4.2 Video recordings

1388 Video recordings of the mouse's face were taken during the spontaneous behaviour. We had  
 1389 access to the top 500 principle components and top 500 eigenvectors of the processed videos.  
 1390 The frequency of recording was slightly less than 40Hz. Each frame contained  $327 \times 561$   
 1391 pixels. These principal components were used as behavioural data. We controlled for these  
 1392 components when taking measurements conditioned on behaviour.

## 1393 2.5 Methods

### 1394 2.5.1 Binning data

1395 We transformed the spike timing data into binned spike count data by dividing the exper-  
 1396 imental period into time bins and counting the spikes fired by each cell within the time period  
 1397 covered by each of those bins. The data were divided into time bins of various widths ranging  
 1398 from 0.01s to 4s.

1399 If the total length of the recording period was not an integer multiple of the time bin  
 1400 width, we cut off the remaining time at the end of the recording period. This period was at  
 1401 most 3.99s. This is far less than the total recording time of around 1 hour. So, this detail  
 1402 would not affect our results.

### 1403 2.5.2 Correlation coefficients

We calculated Pearson's correlation coefficient for pairs of spike counts from pairs of neurons. For jointly distributed random variables  $X$  and  $Y$ , Pearson's correlation coefficient is

defined as:

$$\rho_{XY} = \frac{\text{cov}(X, Y)}{\sigma_X \sigma_Y} \quad (2.1)$$

$$= \frac{E[(X - \mu_X)(Y - \mu_Y)]}{\sigma_X \sigma_Y} \quad (2.2)$$

1404 where  $E$  denotes the expected value,  $\mu$  denotes the mean, and  $\sigma$  denotes the standard deviation.  
 1405 The correlation coefficient is a normalised measure of the covariance. It can take values  
 1406 between 1 (completely correlated) and  $-1$  (completely anti-correlated). Two independent  
 1407 variables will have a correlation coefficient of 0. But, having 0 correlation does not imply  
 1408 independence.

If we do not know the means and standard deviations required for equation 2.1, but we have samples from  $X$  and  $Y$ , Pearson's sample correlation coefficient is defined as:

$$r_{XY} = \frac{\sum_{i=1}^n (x_i - \bar{x})(y_i - \bar{y})}{\sqrt{\sum_{i=1}^n (x_i - \bar{x})^2} \sqrt{\sum_{i=1}^n (y_i - \bar{y})^2}} \quad (2.3)$$

1409 where  $\{(x_i, y_i)\}$  for  $i \in \{1, \dots, n\}$  are the paired samples from  $X$  and  $Y$ , and  $\bar{x} = \frac{1}{n} \sum_{i=1}^n x_i$ ,  
 1410 and  $\bar{y} = \frac{1}{n} \sum_{i=1}^n y_i$  are the sample means.

1411 In practice we used the python function `scipy.stats.pearsonr` to calculate the  
 1412 correlation coefficients.

### 1413 Total correlations, $r_{SC}$

1414 The total correlation ( $r_{SC}$ ) of two cells is the correlation between the spike counts of those  
 1415 cells in response to a given stimulus condition.

### 1416 Shuffled total correlations

1417 We measured the shuffled total correlations between two neurons by randomly permuting one  
 1418 of the neuron's spike counts and measuring the total correlations. These shuffled correlations  
 1419 were useful when measuring the effect of time bin width on correlations, and when decid-  
 1420 ing which correlations should be preserved when creating correlation networks (see section  
 1421 2.5.5).

### 1422 Separating Correlations & Anti-correlations

1423 In order to compare the effect of bin width on measures of negative  $r_{SC}$  (anti-correlation) and  
 1424 positive  $r_{SC}$  separately, we had to separate correlated and anti-correlated pairs. To do this, we

simply measured the mean  $r_{SC}$ , taking the mean across all the bin widths. If this quantity was positive or zero we regarded the pair as positively correlated. If this quantity was negative we regarded the pair as anti-correlated.

### 2.5.3 Conditioning on behavioural data

Our behavioural data consisted of the top 500 principal components (PCs) of a processed video recording of the mouse's face (see section 2.4.2). Denoting the spike count of a given cell by  $X$ , and the PCs by  $Z_1, \dots, Z_{500}$ , we wanted to model  $X$  as a function of  $Z_1, \dots, Z_{500}$  in order to estimate

$$E[X|Z_1, \dots, Z_{500}] = \int_{x \in X} x P(X = x|Z_1, \dots, Z_{500}) dx \quad (2.4)$$

$$= \int_{x \in X} x \frac{P(X = x, Z_1, \dots, Z_{500})}{P(Z_1, \dots, Z_{500})} dx \quad (2.5)$$

Given the 500 components, a naïve estimation of  $P(Z_1, \dots, Z_{500})$  or  $P(X, Z_1, \dots, Z_{500})$  by histogramming was impossible. Therefore we modelled  $X$  as a linear combination of the PCs.

#### Linear regression

We modelled the spike count of a given cell,  $X$ , as a linear combination of the PCs of the video of the mouse's face,  $\mathbf{Z} = Z_1, \dots, Z_{500}$ . We tried three different types of regularization

•  $L1$  or 'Lasso'

•  $L2$  or 'Ridge regression'

• 'Elastic net' regularisation (a linear combination of both  $L1$  and  $L2$  regularisation penalties)

The elastic net regularisation performed the best, so we stuck with that.

#### Elastic net regularisation

Suppose we wish to model  $n$  observations of a random variable  $X$ ,  $\mathbf{x} = (x_1, \dots, x_n)$  using  $n$  instances of  $m$  predictors  $\mathbf{Z} = (Z_1, \dots, Z_m)$ . The naïve elastic net criterion is

$$L(\lambda_1, \lambda_2, \boldsymbol{\beta}) = |\mathbf{x} - \mathbf{Z}\boldsymbol{\beta}|^2 + \lambda_2|\boldsymbol{\beta}|_2 + \lambda_1|\boldsymbol{\beta}|_1 \quad (2.6)$$

where

$$|\boldsymbol{\beta}|_2 = \sum_{j=1}^m \beta_j^2 \quad (2.7)$$

$$|\boldsymbol{\beta}|_1 = \sum_{j=1}^m |\beta_j| \quad (2.8)$$

The naïve elastic net estimator  $\hat{\boldsymbol{\beta}}$  is the minimiser of the system of equations 2.6 (Zou and Hastie, 2005)

$$\hat{\boldsymbol{\beta}} = \arg \min_{\boldsymbol{\beta}} L(\lambda_1, \lambda_2, \boldsymbol{\beta}) \quad (2.9)$$

1441 We implemented the model using the `ElasticNetCV` method of Python's

1442 `sklearn.linear_models` package.

1443 As well as using the PCs, we also tried fitting the models using the raw video data recon-  
1444 structed from the PCs and eigenvectors. These models performed worse than those using the  
1445 PCs. We expected this because each representation contains the same amount of information,  
1446 but the raw video representation spreads this information across many more components.  
1447 This requires more parameter fitting, but given the same information.

1448 **Conditional covariance**

We calculated the expected value of the conditional covariance using the law of total covari-  
ance.

$$\text{cov}(X, Y) = E[\text{cov}(X, Y|Z)] + \text{cov}(E[X|Z], E[Y|Z]) \quad (2.10)$$

1449 where these expected values are calculated with respect to the distribution of  $Z$  as a random  
1450 variable.

1451 The law of total covariance breaks the covariance into two components. The first com-  
1452 ponent  $E[\text{cov}(X, Y|Z)]$  is the expected value, under the distribution of  $Z$ , of the conditional  
1453 covariance  $\text{cov}(X, Y|Z)$ . This covariance could be interpreted as the unnormalised version  
1454 of what Cohen et al. (2011) call the spike count correlation (Cohen and Kohn, 2011), aka.  
1455 the noise correlation. In particular, this is the covariance of the spike counts in response to  
1456 repeated presentation of identical stimuli.

1457 The second component is analogous to what Cohn et al. (2011) call the *signal correlation*  
1458 (Cohen and Kohn, 2011). In particular,  $\text{cov}(E[X|Z], E[Y|Z])$  is the covariance between

1459 spike counts in response to different stimuli.

Using our linear model, we calculated  $E[X|Z_1, \dots, Z_{500}]$  for each cell X. Then we proceeded to calculate

$$E[\text{cov}(X, Y|Z_1, \dots, Z_{500})] = \text{cov}(X, Y) - \quad (2.11)$$

$$\text{cov}(E[X|Z_1, \dots, Z_{500}], E[Y|Z_1, \dots, Z_{500}]) \quad (2.12)$$

1460 **Measures of conditional correlation**

As a measure of expected correlation, we measured the ‘event conditional correlation’ (Maugis, 2014)

$$\rho_{XY|Z} = \frac{E[\text{cov}(X, Y|Z)]}{\sqrt{E[\text{var}(X|Z)]}E[\text{var}(Y|Z)]} \quad (2.13)$$

1461 Although this is not an actual correlation, it is an intuitive analogue to the correlation as a  
1462 normalised version of the covariance.

For comparison, we also measured the ‘signal correlation’

$$\rho_{\text{signal}} = \frac{\text{cov}(E[X|Z], E[Y|Z])}{\sqrt{\text{var}(E[X|Z])}\sqrt{\text{var}(E[Y|Z])}} \quad (2.14)$$

1463 this is an actual correlation.

1464 **2.5.4 Information Theory**

1465 **Entropy  $H(X)$**

The entropy of a random variable X, with outcomes  $x_1, \dots, x_N$ , and corresponding probabilities  $p_1, \dots, p_N$  is defined as

$$H(X) = - \sum_{n=1}^N p_n \log_2 p_n \quad (2.15)$$

1466 This quantity is also known as the information entropy or the ‘surprise’. It measures the  
1467 amount of uncertainty in a random variable. For example, a variable with a probability of 1  
1468 for one outcome, and 0 for all other outcomes will have 0 bits entropy, because it contains no  
1469 uncertainty. But a variable with a uniform distribution will have maximal entropy as it is the  
1470 least predictable. This quantity is analogous to the entropy of a physical system (Shannon,

1471 1948). Note that any base may be used for the logarithm in equation 2.15, but using base 2  
 1472 means that the quantity will be measured in ‘bits’.

The joint entropy of two jointly distributed random variables  $X$  and  $Y$ , where  $Y$  has outcomes  $y_1, \dots, y_M$ , is defined as

$$H(X, Y) = - \sum_{n=1}^N \sum_{m=1}^M P(X = x_n, Y = y_m) \log_2 P(X = x_n, Y = y_m) \quad (2.16)$$

1473 If  $X$  and  $Y$  are independent then  $H(X, Y) = H(X) + H(Y)$ . Otherwise  $H(X, Y) <$   
 1474  $H(X) + H(Y)$ . When  $X$  and  $Y$  are completely dependent  $H(X, Y) = H(X) = H(Y)$ .

The conditional entropy of  $Y$  conditioned on  $X$  is defined as

$$H(Y|X) = - \sum_{n=1}^N \sum_{m=1}^M P(X = x_n, Y = y_m) \log_2 \frac{P(X = x_n, Y = y_m)}{P(X = x_n)} \quad (2.17)$$

1475 When  $X$  and  $Y$  are independent  $H(Y|X) = H(Y)$ . Intuitively, we learn nothing of  $Y$  by  
 1476 knowing  $X$ , so  $Y$  is equally uncertain whether we know  $X$  or not. If  $Y$  is totally dependent  
 1477 on  $X$ , then the fraction in the logarithm is 1, which gives  $H(Y|X) = 0$ .

1478 These entropy measures are the basis of the mutual information measure.

### 1479 Maximum entropy limit

When spiking data is binned into spike counts there is an upper limit on the entropy of these data. The maximum entropy discrete distribution is the discrete uniform distribution. A random variable with this distribution will take values from some finite set with equal probabilities. Binned spike count data will take values between 0 and some maximum observed spike count  $n_{\max}$ . A neuron with responses that maximises entropy will take these values with equal probability, i.e. if  $i \in \{0, \dots, n_{\max}\}$  then  $P(X = i) = \frac{1}{n_{\max}+1}$ . The entropy of this neuron will be

$$\begin{aligned} H(X) &= - \sum_{i=0}^{n_{\max}} P(X = i) \log_2 P(X = i) \\ &= - \sum_{i=0}^{n_{\max}} \frac{1}{n_{\max}+1} \log_2 \left( \frac{1}{n_{\max}+1} \right) \\ &= - \log_2 \left( \frac{1}{n_{\max}+1} \right) \\ &= \log_2 (n_{\max} + 1) \end{aligned}$$

1480 Therefore, the maximum entropy of the binned spike counts of a neuron is  $\log_2(n_{\max} + 1)$ .  
 1481 Of course, it would be very unusual for a neuron to fire in accordance with the discrete  
 1482 uniform distribution. Most measurements of entropy taken on binned spiking data will be  
 1483 much lower than the maximum. See figure 2.17 to see the maximum entropy as a function of  
 1484 the maximum observed spike count.

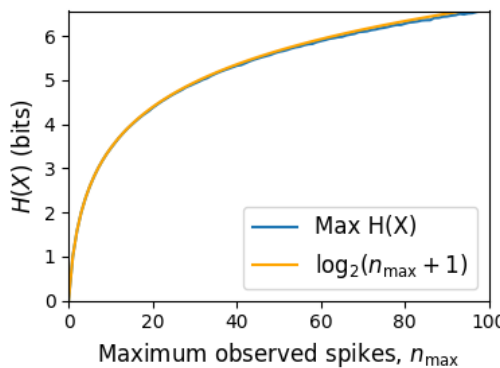


FIGURE 2.17: **Entropy Limit:** The upper limit on entropy of binned spike count data as a function of the maximum observed spike count. The orange line is the analytical maximum. The blue line is the entropy of samples with  $N = 1000$  data points taken from the discrete uniform distribution.

1485 **Mutual Information  $I(X; Y)$**

1486 The mutual information can be defined mathematically in a number of ways, all of which are  
 1487 equivalent. These definitions illustrate the different ways of interpreting the mutual informa-  
 1488 tion.

For two jointly distributed random variables  $X$  and  $Y$ , the mutual information  $I(X; Y)$  is defined as

$$I(X; Y) = H(Y) - H(Y|X) \quad (2.18)$$

$$= H(X) - H(X|Y) \quad (2.19)$$

1489 Equation 2.18 fits with the following intuition: The mutual information between  $X$  and  $Y$  is  
 1490 the reduction in uncertainty about  $X$  gained by knowing  $Y$ , or vice versa. We could also say  
 1491 the mutual information is the amount of information gained about  $X$  by knowing  $Y$ , or vice  
 1492 versa.

Another useful entropy based definition for the mutual information is

$$I(X; Y) = H(X) + H(Y) - H(X, Y) \quad (2.20)$$

1493 This definition is useful because it does not require the calculation of conditional probabilities.  
 1494

The mutual information can also be defined in terms of marginal, joint, and conditional distributions. For example,

$$I(X;Y) = - \sum_{n=1}^N \sum_{m=1}^M P(X = x_n, Y = y_m) \log_2 \frac{P(X = x_n, Y = y_m)}{P(X = x_n)P(Y = y_m)} \quad (2.21)$$

Notice that this can be rewritten as a Kullback–Leibler divergence.

$$I(X;Y) = D_{KL}(P(X,Y) || P(X)P(Y)) \quad (2.22)$$

1495 So, we can also think of the mutual information as a measure of the difference between  
 1496 the joint distribution of  $X$  and  $Y$ , and the product of their marginal distributions. Since the  
 1497 product of the marginal distributions is the joint distribution for independent variables, we  
 1498 can think of the mutual information as a measure of the variables' dependence on one another.

1499 The minimum value that  $I(X;Y)$  can take is 0. This occurs when the random variables  
 1500  $X$  and  $Y$  are independent. Then we have  $H(X|Y) = H(X)$ , and  $H(Y|X) = H(Y)$ , which  
 1501 according to equation 2.18, gives  $I(X;Y) = 0$ . We also have that  $H(X,Y) = H(X) +$   
 1502  $H(Y)$  in this case, which according equation 2.20, gives  $I(X;Y) = 0$ . Finally, we also have  
 1503  $P(X,Y) = P(X)P(Y)$ , which leaves us with 1 in the argument for the logarithm in equation  
 1504 2.21, which again gives  $I(X;Y) = 0$ .

1505 The mutual information reaches its maximum value when one of the variables  $X$  and  
 1506  $Y$  is completely determined by knowing the value of the other. In that case  $I(X;Y) =$   
 1507  $\min\{H(X), H(Y)\}$ .

### 1508 Variation of Information $VI(X,Y)$

The variation of information is another information theoretical quantity based on the mutual information. It is defined as

$$VI(X;Y) = H(X) + H(Y) - 2I(X;Y) \quad (2.23)$$

We can rewrite this as the summation of two positive quantities

$$VI(X;Y) = [H(X) - I(X;Y)] + [H(Y) - I(X;Y)] \quad (2.24)$$

1509 In English, the variation of information is the summation of the uncertainty in the random  
1510 variables  $X$  and  $Y$  excluding the uncertainty shared by those variables.

1511 This measure will become more relevant when we go on to talk about clusterings because  
1512  $VI(X; Y)$  forms a metric on the space of clusterings.

1513 **Measuring entropies & mutual information**

1514 In practice, we measured the mutual information between spike counts using Python and the  
1515 python package `pyitlib`. We used the PT-bias correction technique to estimate the bias of  
1516 our measurements when measuring the mutual information between the spike counts of two  
1517 cells (Treves and Panzeri, 1995).

1518 When measuring the mutual information between clusterings we used Python, but we  
1519 used the `mutual_info_score`, `adjusted_mutual_info_score`, and  
1520 `normalized_mutual_info_score` functions from the `sklearn.metrics` part of  
1521 the `sklearn` package.

1522 **2.5.5 Network analysis**

1523 **Correlation networks**

1524 In order to analyse functional networks created by the neurons in our ensemble, we mea-  
1525 sured the total correlation between each pair of neurons. These measurements induced an  
1526 undirected weighted graph/network between the neurons. The weight of each connection  
1527 was equal to the total correlation between each pair of neurons.

1528 We followed the same procedure for total correlations 2.5.2, spike count correlations, and  
1529 signal correlations 2.5.3.

1530 **Rectified correlations**

1531 At the time of writing, the community detection method outlined in (Humphries et al., 2019)  
1532 could only be applied to networks with positively weighted connections. But many neuron  
1533 pairs were negatively correlated. To apply the community detection method, we *rectified* the  
1534 network, by setting all the negative weights to zero.

1535 We also looked for structure in the network created by negative correlations by reversing  
1536 the signs of the correlations, and rectifying these correlations before applying our network  
1537 analysis.

1538 Finally, we used the absolute value of the correlations as the weights for the graph/network.  
1539 By doing this, we hoped to identify both correlated and anti-correlated functional communi-  
1540 ties of neurons.

1541 **Sparsifying data networks**

1542 When creating our correlation networks, we wanted to exclude any correlations that could  
1543 be judged to exist ‘by chance’. To do this, we measured the 5th and 95th percentile of  
1544 the shuffled correlations (see section 2.5.2) for the given mouse and time bin width. We  
1545 then set all the data correlations between these two values to 0. This excluded any ‘chance’  
1546 correlations from our network, and created a sparser network. This allowed us to make use  
1547 of the ‘sparse weighted configuration model’ as described in section 2.5.5.

1548 **Communities**

1549 Given some network represented by an adjacency matrix  $\mathbf{A}$ , a community within that net-  
1550 work is defined as a collection of nodes where the number of connections within these nodes  
1551 is higher than the expected number of connections between these nodes. In order to quan-  
1552 tify the ‘expected’ number of connections, we need a model of expected networks. This is  
1553 analogous to a ‘null model’ in traditional hypothesis testing. We test the hypothesis that our  
1554 data network departs from the null network model to a statistically significant degree. For  
1555 undirected unweighted networks, the canonical model of a null network is the configuration  
1556 model (Fosdick et al., 2016). Since we are working with weighted sparse networks, we used  
1557 more suitable null models, described below.

1558 **Weighted configuration model**

1559 The *weighted configuration model* is a canonical null network model for weighted networks.  
1560 Given some data network, the weighted configuration model null network will preserve the  
1561 degree sequence and weight sequence of each node in the data network. But the edges will  
1562 be distributed randomly (Fosdick et al., 2016). Any structure in the data network beyond  
1563 its degree sequence and weight sequence will not be captured in the weighted configuration  
1564 model. So, this model can be used in testing the hypothesis that this extra structure exists.

1565 **Sparse weighted configuration model**

1566 The *sparse weighted configuration model* is another null network model. Similar in nature to  
1567 the weighted configuration model (see section 2.5.5), but the sparsity of the data network is

1568 preserved in the null network. This is achieved by sampling from a probability distribution  
 1569 for the creation or non-creation of each possible connection, then distributing the weight of  
 1570 the data network randomly in this sparse network (Humphries et al., 2019). This is the null  
 1571 network that we used when searching for additional structure in our data networks.

1572 **Spectral rejection**

1573 We made use of the spectral rejection algorithm as outlined in (Humphries et al., 2019). The  
 1574 spectral rejection algorithm is a method for finding structure in a network not captured by a  
 1575 supposed null model, if such structure exists.

To describe the method, we denote our data network matrix  $\mathbf{W}$ , we denote the expected network of our null network model as  $\langle \mathbf{P} \rangle$ . Then the departure of our data network from the null network can be described by the matrix

$$\mathbf{B} = \mathbf{W} - \langle \mathbf{P} \rangle \quad (2.25)$$

1576 a common choice for  $\langle \mathbf{P} \rangle$  in community detection is the ‘configuration model’ (Fosdick et  
 1577 al., 2016; Humphries, 2011). The matrix  $\mathbf{B}$  is often called the configuration matrix, in this  
 1578 context we will use the term ‘deviation matrix’ as it captures the deviation of  $\mathbf{W}$  from the  
 1579 null model.

1580 To test for structure in the network represented by  $\mathbf{W}$ , we examine the eigenspectrum of  $\mathbf{B}$   
 1581 and compare it to the eigenspectrum of our null model. Firstly, note that since our data model  
 1582 doesn’t allow self loops, and is not directed, the matrix representing the network will be  
 1583 symmetric and positive semi-definite, and will therefore be invertible with real eigenvalues.  
 1584 We selected a null model with the same characteristics.

1585 To find the eigenspectrum of the null model, we generated  $N$  samples from our null  
 1586 model  $P_1, \dots, P_N$ , and we measured their deviation matrices  $B_1, \dots, B_N$ . We then calculated  
 1587 the eigenspectrum of each of those samples. We calculated the upper bound of the null model  
 1588 eigenspectrum by taking the mean of the largest eigenvalues of  $B_1, \dots, B_N$ . We calculated a  
 1589 lower bound on the null model eigenspectrum by taking the mean of the smallest eigenvalues  
 1590 of  $B_1, \dots, B_N$ .

1591 We then calculated the eigenspectrum of  $\mathbf{B}$ , our data network deviation matrix. If any of  
 1592 those eigenvalues lay outside of the upper or lower bounds of the null model eigenspectrum,  
 1593 this is evidence of additional structure not captured by the null model. If we chose the sparse  
 1594 weighted configuration model (see section 2.5.5) as our null network model, then eigenvalues

1595 lying below the lower bound indicate  $k$ -partite structure in the network. For example, if one  
1596 eigenvalue lay below the lower bound, this would indicate some bipartite structure in the data  
1597 network. If any eigenvalues lay above the upper bound of the null model eigenspectrum, this  
1598 is evidence of community structure in the data network. For example, one eigenvalue of  $\mathbf{B}$   
1599 lying above the upper bound of the null model eigenspectrum indicates the presence of two  
1600 communities in the network (Humphries, 2011).

1601 **Node rejection**

1602 If there are  $d$  data eigenvalues lying outside of the null network eigenspectrum, the  $d$  eigen-  
1603 vectors corresponding to these eigenvalues will form a vector space. If we project the nodes  
1604 of our network into this vector space, by projecting either rows or columns of the data ma-  
1605 trix, we can see how strongly each node contributes to the vector space. Nodes that contribute  
1606 strongly to the additional structure will project far away from the origin, nodes that do not  
1607 contribute to the additional structure will project close to the origin. We want to use this  
1608 information to discard those nodes that do not contribute.

1609 We can test whether a node projects *far* away from the origin or *close* to the origin  
1610 using the eigenvalues and eigenvectors of  $B_1, \dots, B_N$ . The  $j$ th eigenvector and eigenvalue  
1611 of  $B_i$  gives a value for a null network's projection into the  $j$ th dimension of the additional  
1612 structure vector space. The matrices  $B_1, \dots, B_N$  give  $N$  projections into that dimension.  
1613 These projections are a distribution of the null networks' projections. If the data node's  
1614 projection exceeds that of the null network projections this node is judged to project *far* from  
1615 the origin, and therefore contribute to the additional structure. Otherwise, the node is judged  
1616 to project *close* to the origin, and is therefore rejected (Humphries et al., 2019).

1617 **Community detection**

1618 Another application for this  $d$  dimensional space is community detection. We first project  
1619 all of the nodes into this  $d$ -dimensional space, then perform the clustering in this space. The  
1620 clustering and community detection procedure is described in (Humphries, 2011).

1621 In practice, the procedure is carried out  $n$  times (we chose  $n = 100$  times), this returns  $n$   
1622 clusterings. We resolve these  $n$  clusterings to one final clustering using *consensus clustering*.  
1623 We used the consensus clustering method that uses an explicit null model for the consensus  
1624 matrix, as outlined in (Humphries et al., 2019).

### 2.5.6 Clustering Comparison

A clustering  $\mathcal{C}$  is a partition of a set  $D$  into sets  $C_1, C_2, \dots, C_K$ , called clusters, that satisfy the following for all  $k, l \in \{1, \dots, K\}$ :

$$C_k \cap C_l = \emptyset \quad (2.26)$$

$$\bigcup_{k=1}^K C_k = D \quad (2.27)$$

If we consider two clusterings,  $\mathcal{C}$  with clusters  $C_1, C_2, \dots, C_K$  and  $\mathcal{C}'$  with clusters  $C'_1, C'_2, \dots, C'_K$ . There are a number of measurements we can use to compare  $\mathcal{C}$  and  $\mathcal{C}'$ . In the following, the number of elements in  $D$  is denoted by  $n$ , and the number of elements in cluster  $C_k$  is  $n_k$ .

#### Adjusted Rand Index

The *adjusted Rand Index* is a normalised similarity measure for clusterings based on pair counting.

If we consider the clusterings  $\mathcal{C}$  and  $\mathcal{C}'$ , and denote

- the number of pairs in the same cluster in  $\mathcal{C}$  and  $\mathcal{C}'$  by  $N_{11}$

- the number of pairs in different clusters in  $\mathcal{C}$  and  $\mathcal{C}'$  by  $N_{00}$

- the number of pairs in the same cluster in  $\mathcal{C}$  and different clusters in  $\mathcal{C}'$  by  $N_{10}$

- the number of pairs in different clusters in  $\mathcal{C}$  and the same cluster in  $\mathcal{C}'$  by  $N_{01}$

then the *Rand Index* is defined as

$$RI = \frac{N_{11} + N_{00}}{N_{11} + N_{00} + N_{10} + N_{01}} = \frac{N_{11} + N_{00}}{\binom{n}{2}} \quad (2.28)$$

The Rand Index is 1 when the clusterings are identical, and 0 when the clusterings are completely different.

The *adjusted Rand Index* intends on correcting the Rand Index for chance matching pairs.

This is defined as

$$ARI = \frac{2(N_{00}N_{11} - N_{01}N_{10})}{(N_{00} + N_{01})(N_{01} + N_{11}) + (N_{00} + N_{10})(N_{10} + N_{11})} \quad (2.29)$$

The adjusted Rand Index is 1 when the clusterings are identical, and 0 when the Rand Index is equal to its expected value.

---

**1642 Clustering as random variables**

If we take any random element of  $D$ , the probability that this element is in cluster  $C_k$  of clustering  $\mathcal{C}$  is

$$P(K = k) = \frac{n_k}{n} \quad (2.30)$$

1643 this defines a probability distribution, which makes the clustering a random variable. Any  
1644 clustering can be considered as a random variable this way.

This means that we can measure any of the information theoretic quantities defined in section 2.5.4 with respect to clusterings. For example, the entropy of a clustering is

$$H(\mathcal{C}) = - \sum_{k=1}^K \frac{n_k}{n} \log \frac{n_k}{n} \quad (2.31)$$

If we have two clusterings, the joint probability distribution of these clusterings is defined as

$$P(K = k, K' = k') = \frac{|C_k \cap C'_{k'}|}{n} \quad (2.32)$$

1645 The joint distribution allows us to define the mutual information between two clusterings,  
1646  $I(\mathcal{C}; \mathcal{C}')$  (Meilă, 2007).

**1647 Information based similarity measures**

The mutual information between two clusterings is a similarity measure, with  $I(\mathcal{C}; \mathcal{C}') = 0$  if  $\mathcal{C}$  and  $\mathcal{C}'$  are completely different, and  $I(\mathcal{C}; \mathcal{C}') = H(\mathcal{C}) = H(\mathcal{C}')$  if  $\mathcal{C}$  and  $\mathcal{C}'$  are identical. This can be normalised in a number of different ways to make more similarity measures (Vinh, Epps, and Bailey, 2010)

$$NMI_{joint} = \frac{I(\mathcal{C}; \mathcal{C}')}{H(\mathcal{C}, \mathcal{C}')} \quad (2.33)$$

$$NMI_{max} = \frac{I(\mathcal{C}; \mathcal{C}')}{\max\{H(\mathcal{C}), H(\mathcal{C}')\}} \quad (2.34)$$

$$NMI_{sum} = \frac{2I(\mathcal{C}; \mathcal{C}')}{H(\mathcal{C}) + H(\mathcal{C}')} \quad (2.35)$$

$$NMI_{sqrt} = \frac{I(\mathcal{C}; \mathcal{C}')}{\sqrt{H(\mathcal{C})H(\mathcal{C}')}} \quad (2.36)$$

$$NMI_{min} = \frac{I(\mathcal{C}; \mathcal{C}')}{\min\{H(\mathcal{C}), H(\mathcal{C}')\}} \quad (2.37)$$

We can control for chance similarities between the two clusterings by measuring the *adjusted mutual information* between the clusterings. This is defined as

$$AMI_{sum} = \frac{I(\mathcal{C}; \mathcal{C}') - E\{I(\mathcal{C}; \mathcal{C}')\}}{\frac{1}{2}[H(\mathcal{C}) + H(\mathcal{C}')] - E\{I(\mathcal{C}; \mathcal{C}')\}} \quad (2.38)$$

1648 The first term in the denominator, taking the average of the marginal entropies, can be re-  
 1649 placed by taking the maximum, minimum, or the geometric mean (Vinh, Epps, and Bailey,  
 1650 2010).

### 1651 Information based metrics

The variation of information between two clusterings  $VI(\mathcal{C}; \mathcal{C}')$  (see section 2.5.4) is a metric on the space of clusterings (Meilă, 2007). That is,

$$VI(\mathcal{C}; \mathcal{C}') \geq 0 \quad (2.39)$$

$$VI(\mathcal{C}; \mathcal{C}') = 0 \iff \mathcal{C} = \mathcal{C}' \quad (2.40)$$

$$VI(\mathcal{C}; \mathcal{C}') = VI(\mathcal{C}'; \mathcal{C}) \quad (2.41)$$

$$VI(\mathcal{C}; \mathcal{C}'') \leq VI(\mathcal{C}; \mathcal{C}') + VI(\mathcal{C}'; \mathcal{C}'') \quad (2.42)$$

Another metric is the *information distance* (Vinh, Epps, and Bailey, 2010)

$$D_{max} = \max\{H(\mathcal{C}), H(\mathcal{C}')\} - I(\mathcal{C}; \mathcal{C}') \quad (2.43)$$

Both of these can be normalised

$$NVI(\mathcal{C}; \mathcal{C}') = 1 - \frac{I(\mathcal{C}; \mathcal{C}')}{H(\mathcal{C}, \mathcal{C}')} \quad (2.44)$$

$$d_{max} = 1 - \frac{I(\mathcal{C}; \mathcal{C}')}{\max\{H(\mathcal{C}), H(\mathcal{C}')\}} \quad (2.45)$$

### 1652 Comparing detected communities and anatomical divisions

1653 In order to quantify the difference or similarity between the communities detected in our cor-  
 1654 relation network and the anatomical classification of the cells in that network, we considered  
 1655 the communities and the anatomical regions as clusters in two different clusterings,  $\mathcal{C}_{comm}$   
 1656 and  $\mathcal{C}_{anat}$ , respectively. We then measured the similarity between the clusterings using the  
 1657 mutual information, the adjusted mutual information, and the normalised mutual informa-  
 1658 tion. We measured the difference between, or the distance between, the clusterings using the

1659 variation of information, the normalised variation of information, and the normalised infor-  
1660 mation distance. We also measured the difference between the clusterings using the adjusted  
1661 Rand Index, just to use a non-information based measure.

1662 We took all of these measures for communities detected using different time bin widths.  
1663 This gave us an idea of the effect of time bin width on correlation networks in neural ensem-  
1664 bles relative to anatomical regions within those ensembles.

1665 **Chapter 3**

1666 **A simple two parameter distribution  
for modelling neuronal activity and  
capturing neuronal association**



1669                    *Abstract*

1670    Recent developments in electrophysiological technology have lead to an increase in the size  
1671    of electrophysiology datasets. Consequently, there is a requirement for new analysis tech-  
1672    niques that can make use of these new datasets, while remaining easy to use in practice. In  
1673    this work, we fit some one or two parameter probability distributions to spiking data collected  
1674    from a mouse exposed to visual stimuli. We show that the Conway-Maxwell-binomial dis-  
1675    tribution is a suitable model for the number of active neurons in a neuronal ensemble at any  
1676    given moment. This distribution fits these data better than binomial or beta-binomial distribu-  
1677    tions. It also captures the correlated activity in the primary visual cortex induced by stimulus  
1678    onset more effectively than simply measuring the correlations, at short timescales (< 10ms).  
1679    We also replicate the finding of Churchland et al (2010) relating to stimulus onset quenching  
1680    neural variability in cortical areas, and we show a correspondence between this quenching  
1681    and changes in one of the parameters of the fitted Conway-Maxwell-binomial distributions.

1682 **3.1 Introduction**

1683 Recent advances in electrophysiological technology, such as ‘Neuropixels’ probes (Jun et al.,  
1684 2017) have allowed extracellular voltage measurements to be collected from larger numbers  
1685 of cells than traditional methods, in multiple brain regions simultaneously, and routinely.  
1686 These larger datasets require innovative methods to extract information from the data in a  
1687 reasonable amount of time, ‘reasonable’ being subjective in this case.

1688 Theoretically, all the information at any given moment in an electrophysiological dataset  
1689 with  $n$  neurons could be captured by calculating the probability distribution for every possi-  
1690 ble spiking pattern. This would require defining a random variable with  $2^n$  possible values, a  
1691 task that quickly becomes impossible as  $n$  increases. Attempts at approximating this random  
1692 variable often involve measuring pairwise or higher order correlations (Schneidman et al.,  
1693 2006; Flach, 2013; Ganmor, Segev, and Schneidman, 2011). But pairwise correlations may  
1694 not be enough to characterise instantaneous neural activity (Tkačik et al., 2014). Further-  
1695 more, these kinds of models tend to ignore the temporal structure of neuronal data, in favour  
1696 of smaller model size, and scalability.

1697 Higher order correlations would be helpful here, but defining these correlations can be  
1698 tricky, never-mind quantifying them. If we use the interaction parameters arising from the  
1699 exponential family model as measures of higher order correlations, measuring these correla-  
1700 tions becomes computationally impractical quite quickly also (the number of ‘three neuron  
1701 correlations’ to measure scales with  $\binom{n}{3}$ ). In this paper, we dispense with measuring correla-  
1702 tions directly, and attempt to characterise correlated behaviour by measuring ‘association’; a  
1703 more general concept that includes correlation.

1704 In this work, we examined the ability of simple distributions to model the number of  
1705 active (spiking) neurons in a neuronal ensemble at any given timepoint. We compared a  
1706 little-known distribution named the Conway-Maxwell-binomial distribution to the binomial  
1707 distribution and the beta-binomial distribution. The binomial distribution is a probability dis-  
1708 tribution over the number of successes in a sequence of independent and identical Bernoulli  
1709 trials. The beta-binomial distribution is similar, but allows for a bit more flexibility while still  
1710 being a model for heterogeneity. Similar to the binomial and beta-binomial, the Conway-  
1711 Maxwell-binomial distribution is a probability distribution over the number of successes in a  
1712 series of Bernoulli trials, but allows over- and under-dispersion relative to the binomial dis-  
1713 tribution. This distribution should therefore be a good candidate for our purposes. We found  
1714 that Conway-Maxwell-binomial distribution was usually the best candidate of the three that

1715 we examined.

1716 We also observed some interesting changes in the number of active neurons in the primary  
1717 visual cortex and hippocampus at stimulus onset and some changes in this activity in the  
1718 thalamus which were sustained for the full duration of the stimulus presentation. This let us  
1719 know that there were some responses to model.

1720 We found that fitting a Conway-Maxwell-binomial distribution was a better method of  
1721 capturing association between neurons than measuring the spike count correlation for the  
1722 short time bins that we used (< 10ms).

1723 Finally, we also wanted to investigate parallels between the parameters of the Conway-  
1724 Maxwell-binomial distribution and quantities that have been established as relevant to sen-  
1725 sory processing. So, we replicated the findings made by Churchland et al. (2010) relating  
1726 to a reduction in neural variability at stimulus onset in the macaque cortical regions, but for  
1727 data taken from the mouse primary visual cortex. We compared these findings to the values  
1728 of the fitted Conway-Maxwell-binomial distribution parameters.

## 1729 3.2 Data

1730 We used data collected by Nick Steinmetz and his lab ‘CortexLab at UCL’ (Steinmetz, Caran-  
1731 dini, and Harris, 2019). The data can be found online <sup>1</sup> and are free to use for research  
1732 purposes.

1733 Two ‘Phase3’ Neuropixels (Jun et al., 2017) electrode arrays were inserted into the brain  
1734 of an awake, head-fixed mouse for about an hour and a half. These electrode arrays recorded  
1735 384 channels of neural data each at 30kHz and less than  $7\mu\text{V}$  RMS noise levels. The sites  
1736 are densely spaced in a ‘continuous tetrode’-like arrangement, and a whole array records  
1737 from a 3.8mm span of the brain. One array recorded from visual cortex, hippocampus, and  
1738 thalamus, the other array recorded from motor cortex and striatum. The data were spike-  
1739 sorted automatically by Kilosort and manually by Nick Steinmetz using Phy. In total 831  
1740 well-isolated individual neurons were identified.

### 1741 3.2.1 Experimental protocol

1742 The mouse was shown a visual stimulus on three monitors placed around the mouse at right  
1743 angles to each other, covering about  $\pm 135$  degrees azimuth and  $\pm 35$  degrees elevation.

---

<sup>1</sup><http://data.cortexlab.net/dualPhase3/>

1744 The stimulus consisted of sine-wave modulated full-field drifting gratings of 16 drift di-  
1745 rections ( $0^\circ, 22.5^\circ, \dots, 337.5^\circ$ ) with 2Hz temporal frequency and 0.08 cycles/degree spatial  
1746 frequency displayed for 2 seconds plus a blank condition. Each of these 17 conditions were  
1747 presented 10 times in a random order across 170 different trials. There were therefore 160  
1748 trials with a drifting-grating visual stimulus present, and 10 trials with a blank stimulus.

1749 **3.3 Methods**

1750 **3.3.1 Binning data**

1751 We converted the spike times for each cell into spike counts by putting the spike times into  
1752 time bins of a given ‘width’ (in milliseconds). We used time bins of 1ms, 5ms, and 10ms.  
1753 We used different time bin widths to assess the impact of choosing a bin width.

1754 **3.3.2 Number of *active* neurons**

1755 To count the number of active neurons in each neuronal ensemble, we split the time interval  
1756 for each trial into bins of a given width. We counted the number of spikes fired by each cell  
1757 in each bin. If a cell fired *at least* one spike in a given bin, we regarded that cell as active in  
1758 that bin. We recorded the number of active cells in every bin, and for the purposes of further  
1759 analysis, we recorded each cell’s individual spike counts.

1760 It should be noted that when we used a bin width of 1ms, the maximum number of  
1761 spikes in any bin was 1. For the wider time bins, some bins had spike counts greater than  
1762 1. Consequently when using a bin width of 1ms, the number of active neurons and the total  
1763 spike count of a given bin were identical. But for wider bin widths, the total spike count was  
1764 greater than the number of active neurons.

1765 So for the 1ms bin width, the activity of a neuron and the number of spikes fired by that  
1766 neuron in any bin can be modelled as a Bernoulli variable. But for wider time bins, only the  
1767 activity can be modelled in this way.

1768 **3.3.3 Moving windows for measurements**

1769 When taking measurements (e.g. moving average over the number of active neurons) or  
1770 fitting distributions (eg. the beta binomial distribution) we slid a window containing a certain  
1771 number of bins across the data, and made our measurements at each window position. For  
1772 example, when analysing 1ms bin data, we used a window containing 100 bins, and we slid

Bin width (ms)	Window size (bins)	Window size (ms)	Windows per trial
1ms	100	100ms	296
5ms	40	200ms	286
10ms	40	400ms	266

TABLE 3.1: Details of the different bin width and analysis window sizes used when binning spike times, and analysing those data.

1773 the window across the time interval for each trial moving 10 bins at a time. So that for  
 1774 3060ms of data, we made 296 measurements.

1775 For the 5ms bin width data, we used windows containing 40 bins, and slid the window 2  
 1776 bins at a time when taking measurements.

1777 For the 10ms bin width data, we used windows containing 40 bins, and slid the window  
 1778 1 bin at a time when taking measurements (see table 3.1 for concise details).

1779 By continuing to use windows containing 40 bins, we retained statistical power but sac-  
 1780 rificed the number of measurements taken.

1781 There was an interval between each trial with a grey image in place of the moving of  
 1782 the moving bar stimulus. This interval varied in time. But we included some of this interval  
 1783 when recording the data for each trial. We started recording the number of active neurons,  
 1784 and the number of spikes from each neuron from 530ms before each trial until 1030ms after  
 1785 each trial. This way, we could see the change in our measurements at the onset of a stimulus  
 1786 and the end of stimulus presentation.

1787 As mentioned in section 3.3.2, we recorded the number of active neurons in each bin, and  
 1788 the spike count for each neuron in each bin. The actual measurements we took using these  
 1789 data in each window were as follows:

1790 **Moving average** The average number of active cells in each window.

1791 **Moving variance** The variance of the number of active cells in each window.

1792 **Average correlation** We measured the correlation between the spike counts of each pair of  
 1793 cells in the ensemble, and took the average of these measurements.

1794 **Binomial  $p$**  We fitted a binomial distribution to the data in each window and recorded the  
 1795 fitted probability of success,  $p$  in each case.

1796 **Beta-binomial  $\alpha, \beta$**  We fitted a beta-binomial distribution to the data in each window, and  
 1797 recorded the values of the fitted shape parameters,  $\alpha$  and  $\beta$ , of each distribution.

1798 **Conway-Maxwell-binomial distribution  $p, \nu$**  We fitted a Conway-Maxwell-binomial dis-  
 1799 tribution to the data in each window, and recorded the fitted values of  $p$  and  $\nu$  for each  
 1800 distribution.

1801 **Log-likelihoods** We also recorded the log-likelihood of each of the fitted distributions for  
 1802 each window.

1803 **3.3.4 Fano factor**

The *Fano factor* of a random variable is defined as the ratio of the variable's variance to its mean.

$$F = \frac{\sigma^2}{\mu} \quad (3.1)$$

1804 We measured the Fano factor of the spike count of a given cell by measuring the mean and  
 1805 variance of the spike count across trials, and taking the ratio of those two quantities. When  
 1806 calculated in this way the Fano factor can be used as a measure of neural variability that  
 1807 controls for changes in the firing rate. This is similar to the calculation used in (Churchland  
 1808 et al., 2010).

1809 **3.3.5 Probability Distributions suitable for modelling ensemble activity**

1810 We present here three different probability distributions that could be suitable to model the  
 1811 number of active neurons in an ensemble. Each distribution has the set  $\{0, \dots, n\}$  as its sup-  
 1812 port, where  $n$  is the number of neurons in the ensemble. These are simple distributions with  
 1813 either two or three parameters each. However, we regard  $n$  as known when using these dis-  
 1814 tributions for modelling, so in effect each distribution has either one or two free parameters.

1815 **Association**

1816 *Association* between random variables is similar to the correlation between random variables  
 1817 but is more general in concept. The correlation is a measure of association; and association  
 1818 doesn't have a mathematical definition like correlation does. Essentially, the association  
 1819 between two random variables is their tendency to take the same or similar values. Positively  
 1820 associated variables tend to take the same value, and negatively associated variables tend to  
 1821 take different values. In this research, we work with probability distributions of the number of  
 1822 successes in a set of Bernoulli trials. These Bernoulli variables may or may not be associated.

1823 A probability distribution over the number of successes in  $n$  Bernoulli trials, where the  
 1824 Bernoulli variables may be associated, could constitute a good model for the number of active  
 1825 neurons in an ensemble of  $n$  neurons.

1826 **Binomial distribution**

The binomial distribution is a two parameter discrete probability distribution that can be thought of as a probability distribution the number of successes from  $n$  independent Bernoulli trials, each with the same probability of success. The parameters of the binomial distribution are  $n$  the number of trials, and  $0 \leq p \leq 1$ , the probability of success for each of these trials. A random variable with the binomial distribution can take values from  $\{0, \dots, n\}$ . The probability mass function of the distribution is

$$P(k; n, p) = \binom{n}{k} p^k (1 - p)^{n-k} \quad (3.2)$$

1827 As a model for the activity of a neuronal ensemble, the main problem with the binomial  
 1828 distribution is that it treats each neuron, represented as a Bernoulli trial, as independent. It is  
 1829 well known that neurons are not independent, and that correlated behaviour between neurons  
 1830 is vital for representing sensory information (Cohen and Maunsell, 2009). The binomial dis-  
 1831 tribution falls short in this regard, but it is useful as performance benchmark when assessing  
 1832 the performance of other models.

1833 **Beta-binomial distribution**

1834 The beta distribution is the conjugate distribution of the binomial distribution. The beta-  
 1835 binomial distribution is the combination of the beta distribution and the binomial distribution,  
 1836 in that the probability of success for the binomial distribution is sampled from the beta dis-  
 1837 tribution. This allows the beta-binomial distribution to capture some over dispersion relative  
 1838 to the binomial distribution.

The beta-binomial distribution is a three parameter distribution,  $n$  the number of Bernoulli trials, and  $\alpha \in \mathbb{R}_{>0}$  and  $\beta \in \mathbb{R}_{>0}$  the shape parameters of the beta distribution. The probability mass function for the beta-binomial distribution is

$$P(k; n, \alpha, \beta) = \binom{n}{k} \frac{B(k + \alpha, n - k + \beta)}{B(\alpha, \beta)} \quad (3.3)$$

1839 where  $B(\alpha, \beta)$  is the beta function.

This probability distribution can be reparametrised in a number of ways. One of which defines new parameters  $\pi$  and  $\rho$  by

$$\pi = \frac{\alpha}{\alpha + \beta} \quad (3.4)$$

$$\rho = \frac{1}{\alpha + \beta + 1} \quad (3.5)$$

1840 This reparametrisation is useful because  $\pi$  acts as a location parameter analogous to the  $p$   
 1841 parameter of a binomial distribution. A value of  $\rho > 0$  indicates over-dispersion relative to a  
 1842 binomial distribution.

1843 As a model for the activity of a neuronal ensemble, the beta-binomial distribution is  
 1844 more suitable than a binomial distribution because the over-dispersion of the beta-binomial  
 1845 distribution can be used to model positive association between the neurons. An extreme  
 1846 example of this over-dispersion/positive association can be seen in figure 3.1b. In this figure,  
 1847 the neurons are positively associated and so tend to take the same value, consequently the  
 1848 probability mass of the beta-binomial distribution builds up close to  $k = 0$  and  $k = n$ . It is  
 1849 worth noting that the location parameter for each distribution has the same value,  $p = \pi =$   
 1850 0.5.

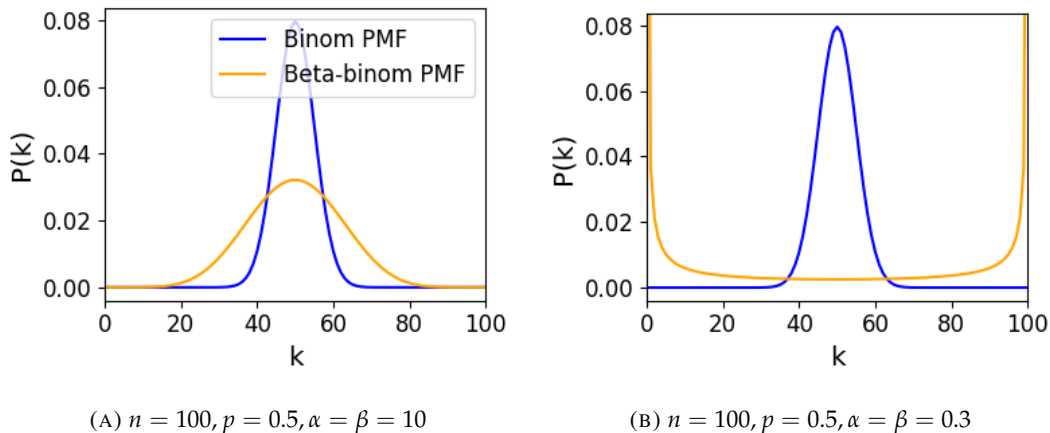


FIGURE 3.1: Figures showing the over-dispersion possible for a beta-binomial distribution relative to a binomial distribution. Parameters are shown in the captions.

### 1851 Conway-Maxwell-binomial distribution

1852 The Conway-Maxwell-binomial distribution (COMb distribution) is a three parameter generalisation of the binomial distribution that allows for over dispersion and under dispersion

relative to the binomial distribution. The parameters of the distribution are  $n$  the number of Bernoulli trials, and two shape parameters  $0 \leq p \leq 1$ , and  $\nu \in \mathbb{R}$ .

The probability mass function of the COMb distribution is

$$P(k; n, p, \nu) = \frac{1}{S(n, p, \nu)} \binom{n}{k}^{\nu} p^k (1-p)^{n-k} \quad (3.6)$$

where

$$S(n, p, \nu) = \sum_{j=0}^n \binom{n}{j}^{\nu} p^j (1-p)^{n-j} \quad (3.7)$$

The only difference between this PMF and the PMF for the standard binomial is the introduction of  $\nu$  and the consequent introduction of the normalising function  $S(n, p, \nu)$ .

Indeed, if  $\nu = 1$  the COMb distribution is identical to the binomial distribution with the same values for  $n$  and  $p$ . We can see in figure 3.2d that the KL-divergence  $D_{KL}(P_{COMb}(n, p, \nu) || P_{Bin}(n, p)) = 0$  along the line where  $\nu = 1$ . The analytical expression for the divergence is

$$D_{KL}(P_{COMb}(k; n, p, \nu) || P_{Bin}(k; n, p)) = (\nu - 1) E_{P_{COMb}(k; n, p, \nu)} \left[ \log \binom{n}{k} \right] \quad (3.8)$$

$$- \log S(n, p, \nu) \quad (3.9)$$

At  $\nu = 1$ , we have  $S(n, p, 1)$  which is just the sum over the binomial PMF, so  $S(n, p, 1) = 1$  and therefore  $D_{KL}(P_{COMb}(n, p, \nu) || P_{Bin}(n, p)) = 0$ .

If  $\nu < 1$  the COMb distribution will exhibit over-dispersion relative to the binomial distribution. If  $p = 0.5$  and  $\nu = 0$  the COMb distribution is the discrete uniform distribution, and if  $\nu < 0$  the mass of the COMb distribution will tend to build up near  $k = 0$  and  $k = n$ . This over-dispersion represents positive association in the Bernoulli variables. An example of this over-dispersion can be seen in figure 3.2b.

If  $\nu > 1$  the COMb distribution will exhibit under-dispersion relative to the binomial distribution. The larger the value of  $\nu$  the more probability mass will build up at  $n/2$  for even  $n$ , or at  $\lfloor n/2 \rfloor$  and  $\lceil n/2 \rceil$  for odd  $n$ . This under-dispersion represents negative association in the Bernoulli variables. An example of this under-dispersion can be seen in figure 3.2a.

It should be noted that the  $p$  parameter of the COMb distribution does not correspond to the mean of the distribution, as is the case for the binomial  $p$  parameter, and beta-binomial  $\pi$  parameter. That is, the COMb  $p$  parameter is not a location parameter. An illustration of this can be seen in figure 3.2c. This is because an interaction between the  $p$  and  $\nu$  parameters skews the mean. There is no analytical expression for the mean of the COMb distribution.

$\nu$	Relative dispersion	Association between neurons/variables
< 1	over	positive
1	none	none
> 1	under	negative

TABLE 3.2: Relative dispersion of the COMb distribution, and association between Bernoulli variables as represented by the value of the  $\nu$  parameter.

1874 Since the COMb distribution has the potential to capture positive and negative associa-  
 1875 tions between the neurons/Bernoulli variables, it should be an excellent candidate for mod-  
 1876 elling the number of active neurons in a neuronal ensemble.

1877 We wrote a dedicated Python package to enable easy creation and fitting of COMb dis-  
 1878 tribution objects. The format of the package imitates the format of other distribution objects  
 1879 from the `scipy.stats` Python package. The COMb package can be found here:  
 1880 [https://github.com/thomasjdelaney/Conway\\_Maxwell\\_Binomial\\_Distribution](https://github.com/thomasjdelaney/Conway_Maxwell_Binomial_Distribution)

### 1881 3.3.6 Fitting

1882 We fitted binomial, beta-binomial, and Conway-Maxwell-binomial (COMb) distributions to  
 1883 the neural activity in each of the overlapping windows covering each trial. To fit the distribu-  
 1884 tions we minimised the appropriate negative log likelihood function using the data from the  
 1885 window.

There is an analytical solution for maximum likelihood estimate of the binomial distribution's  $p$  parameter.

$$\hat{p} = \frac{1}{n} \sum_{i=1}^N k_i \quad (3.10)$$

1886 We minimised the negative log likelihood function of the beta-binomial distribution nu-  
 1887 merically. We calculated the negative log likelihood for a sample directly, by taking the sum  
 1888 of the log of the probability mass function for each value in the sample. We minimised the  
 1889 negation of that function using the `minimise` function of the `scipy.optimize` Python  
 1890 package.

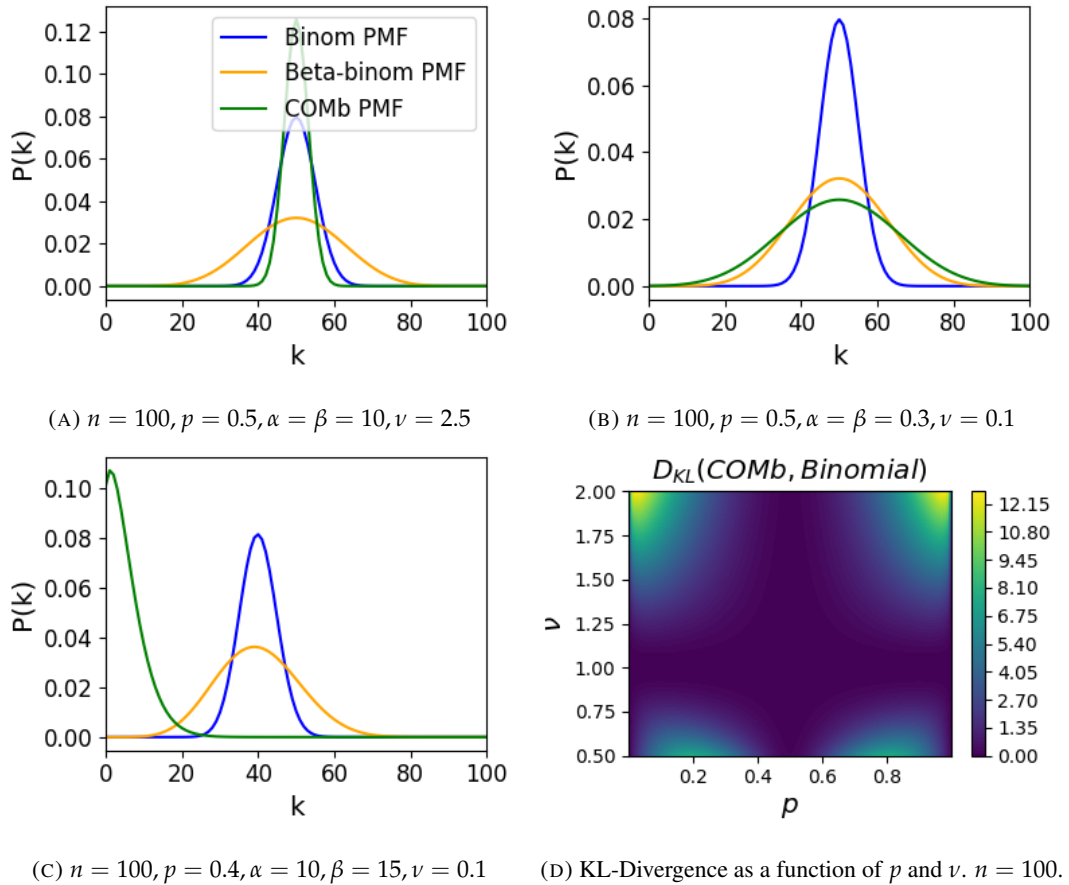


FIGURE 3.2: Figures showing (A) the under-dispersion and (B) over-dispersion permitted by the COMb distribution relative to a binomial distribution. (C) illustrates that the  $p$  parameter of the COMb distribution does not correspond to the mean of the distribution, as it does for the binomial and beta-binomial distributions. (D) shows a heatmap for the value of the Kullback-Liebler divergence between the COMb distribution and the standard binomial distribution with same value for  $n$ , as a function of  $p$  and  $\nu$ . Parameters are shown in the captions.

The log likelihood function of the COMb distribution given some sample  $\{k_1, \dots, k_N\}$  is

$$\ell(p, \nu | k_1, \dots, k_N) = N [n \log(1 - p) - \log S(n, p, \nu)] \quad (3.11)$$

$$+ \log \frac{p}{1 - p} \sum_{i=1}^N k_i \quad (3.12)$$

$$+ \nu \sum_{i=1}^N \log \binom{n}{k_i} \quad (3.13)$$

1891 We minimised the negation of this function using numerical methods. More specifically, we  
 1892 used the `minimise` function of the `scipy.optimize` Python package.

1893 **3.3.7 Goodness-of-fit**

1894 After fitting, we measured the goodness-of-fit of each model/distribution with their log like-  
 1895 lihood. We calculated this directly using the `logpmf` functions of the distribution objects in  
 1896 Python.

1897 **3.4 Results**

1898 We defined a neuron as *active* in a time bin if it fires at least one spike during the time interval  
 1899 covered by that bin. We measured the number of active neurons in the primary visual cortex  
 1900 of a mouse in 1ms bins across 160 trials of a moving bar visual stimulus. We then slid a  
 1901 100ms window across these 1ms bins taking measurements, and fitting distributions along  
 1902 the way. We did the same for neurons in the thalamus, hippocampus, striatum, and motor  
 1903 cortex. We repeated the analysis for 5ms time bins with 40 bin windows, and 10ms time bins  
 1904 with 40 bin windows.

1905 **3.4.1 Increases in mean number of active neurons and variance in number of  
 1906 active neurons at stimulus onset in some regions**

1907 We measured the average number of active neurons, and the variance of the number of active  
 1908 neurons in a 100ms sliding window starting 500ms before stimulus onset until 1000ms after  
 1909 stimulus onset. We found differences in the response across regions. There were no observed  
 1910 changes in response to the stimulus in the motor cortex or the striatum. The changes in the  
 1911 other regions are detailed below.

**1912 Primary visual cortex**

1913 We found a transient increase in both the average and variance of the number of active neu-  
1914 rons at stimulus onset, followed by a fall to pre-stimulus levels, followed by another transient  
1915 increase (see figure 3.3). The oscillation in both of these measurements appear to reflect the  
1916 frequency of the stimulus (see Data section 3.2.1), and it is known that stimulus structure can  
1917 influence response structure(Litwin-Kumar, Chacron, and Doiron, 2012). We see a similar  
1918 but lower amplitude oscillation at the end of the stimulus presentation.

**1919 Hippocampus**

1920 In the hippocampus we observed a transient increase in the average number of active neurons  
1921 and in the variance of the number of active neurons at stimulus onset (see figure 3.4). The  
1922 increase lasted about 125ms, and the subsequent fall to baseline took the a similar amount of  
1923 time.

**1924 Thalamus**

1925 In the thalamus we observed a transient increase in the both the average and variance of  
1926 the number of active neurons on stimulus onset, followed by a fall to pre-stimulus levels,  
1927 followed by a sustained increase until the stimulus presentation ends.

1928 As one you might expect for a visual stimulus, the change in the average number of active  
1929 neurons was greatest in the primary visual cortex. In this region, this quantity doubled on  
1930 stimulus onset. In contrast, in the hippocampus and the thalamus, the average number of  
1931 active neurons only increased by a fraction of the unstimulated baseline value. The duration  
1932 of the response in V1 and the hippocampus at stimulus onset was 300 – 400ms, but the  
1933 response in the thalamus appeared to last for the duration of stimulus presentation. The V1  
1934 also showed a change in the average number of active neurons at stimulus end. The change  
1935 was similar to that observed at stimulus onset, but smaller in magnitude (see figures 3.3, 3.4,  
1936 and 3.5)

**1937 3.4.2 Conway-Maxwell-binomial distribution is usually a better fit than bino-  
1938 mial or beta-binomial**

1939 Since the Conway-Maxwell-binomial distribution has not been fitted to neuronal data before,  
1940 it is not clear that it would be a better fit than the binomial or beta-binomial distributions.  
1941 In order to find out which parametric distribution was the best fit for the largest proportion

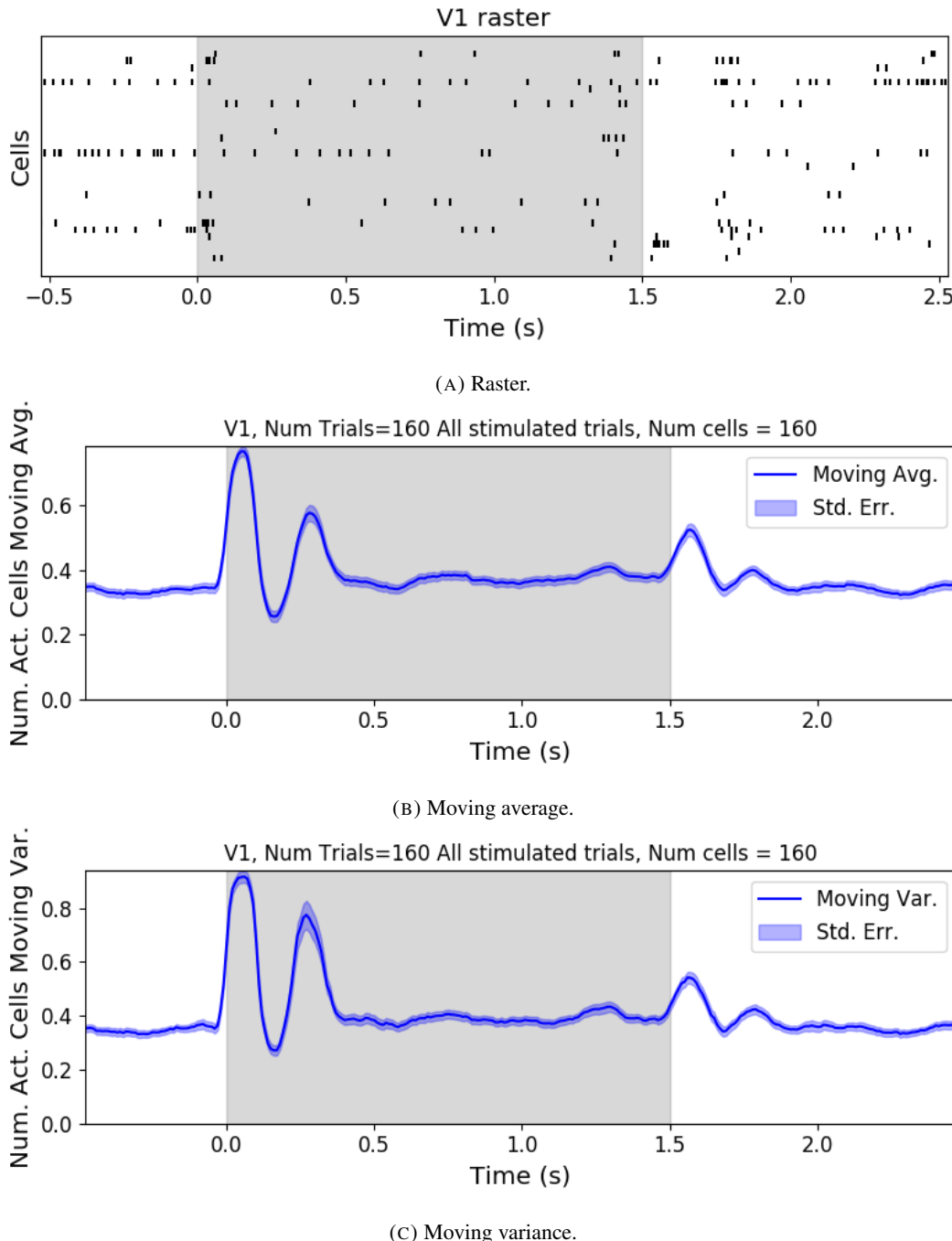


FIGURE 3.3: (A) Raster plot showing the spikes fired by 33 randomly chosen neurons in the primary visual cortex. (B-C) (B) average and (C) variance of the number of active neurons, measured using a sliding window 100ms wide, split into 100 bins. The midpoint of the time interval for each window is used as the timepoint (x-axis point) for the measurements using that window. The grey shaded area indicates the presence of a visual stimulus. The opaque line is an average across the 160 trials that included a visual stimulus of any kind. We can see a transient increase in the average number of active neurons and the variance of this number, followed by a fluctuation and another increase.

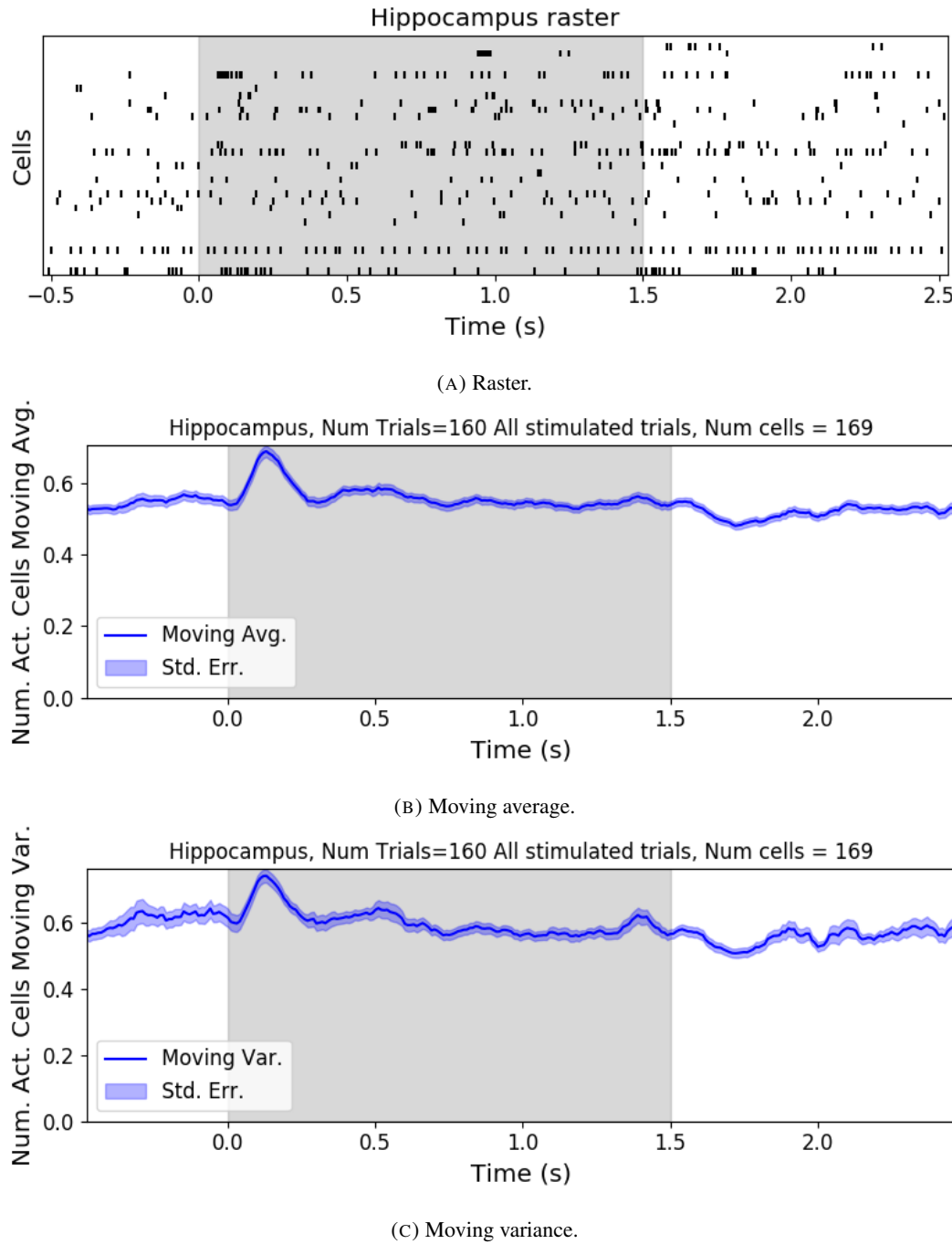


FIGURE 3.4: (A) Raster plot showing the spikes fired by 33 randomly chosen neurons in the hippocampus. (B-C) (B) average and (C) variance of the number of active neurons, measured using a sliding window 100ms wide, split into 100 bins. The midpoint of the time interval for each window is used as the timepoint (x-axis point) for the measurements using that window. The grey shaded area indicates the presence of a visual stimulus. The opaque line is an average across the 160 trials that included a visual stimulus of any kind. We can see a transient increase in the average number of active neurons and the variance of this number at stimulus onset.

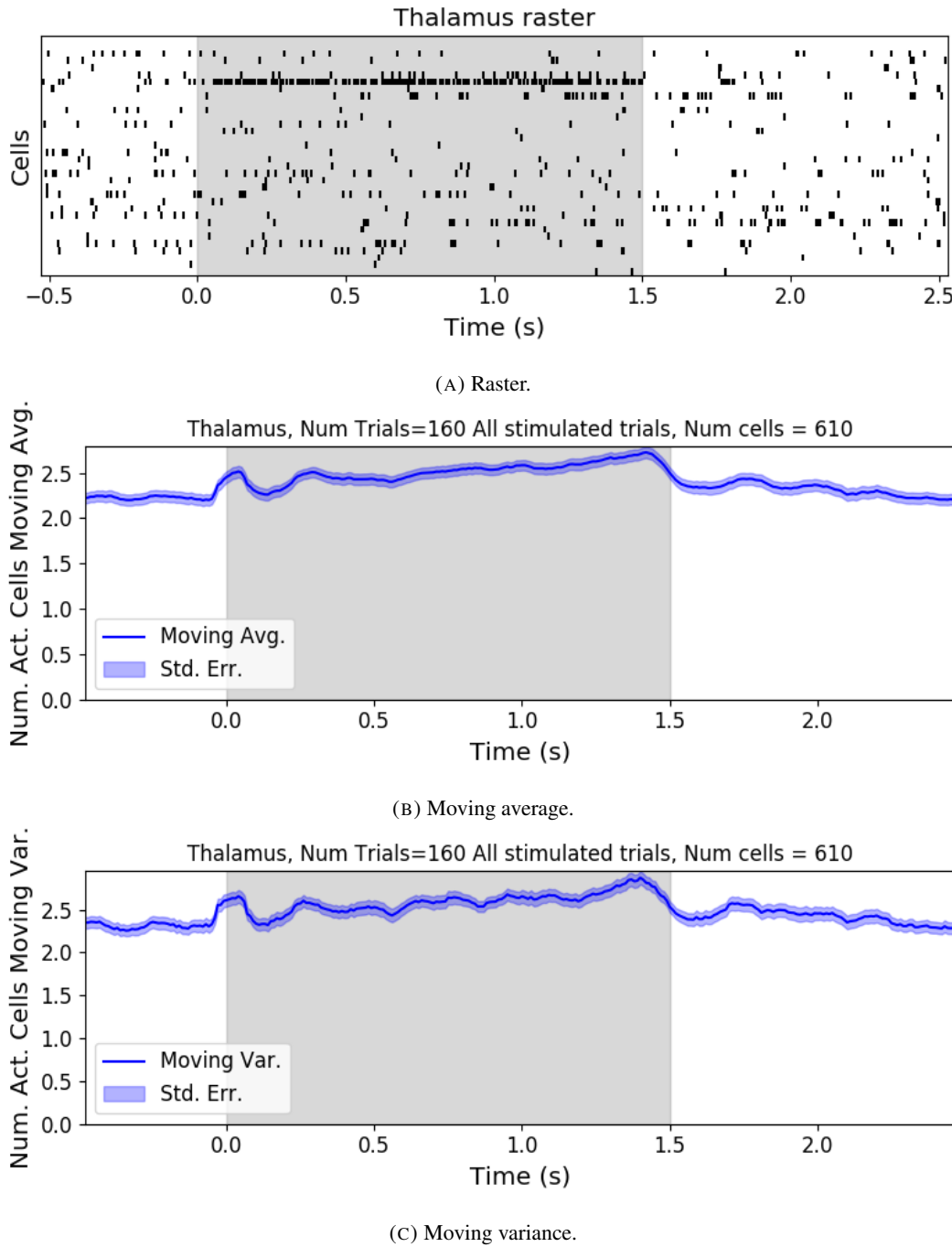
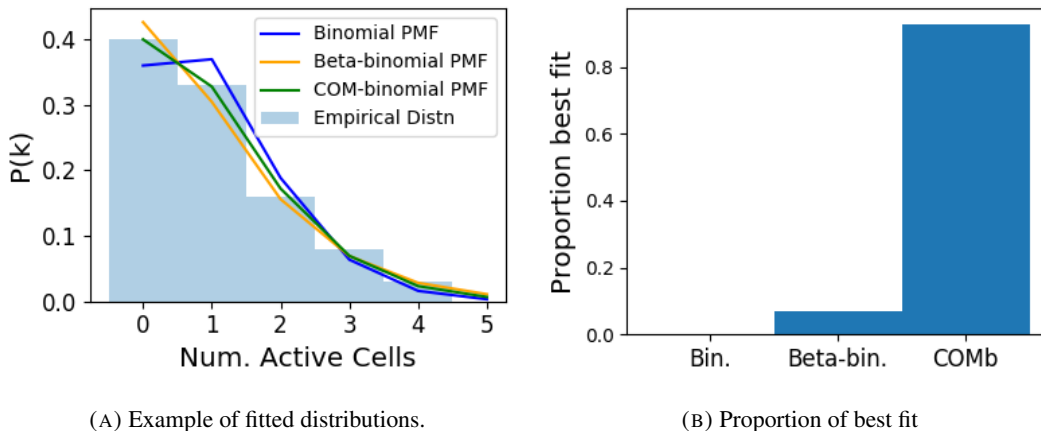


FIGURE 3.5: (A) Raster plot showing the spikes fired by 33 randomly chosen neurons in the thalamus. (B-C) (B) average and (C) variance of the number of active neurons, measured using a sliding window 100ms wide, split into 100 bins. The midpoint of the time interval for each window is used as the timepoint (x-axis point) for the measurements using that window. The grey shaded area indicates the presence of a visual stimulus. The opaque line is an average across the 160 trials that included a visual stimulus of any kind. We can see an immediate increase at stimulus onset, a subsequent fall, and another sustained increase until the stimulus presentation ends.

of our data, we fit a binomial, a beta-binomial, and a Conway-Maxwell-binomial (COMb) distribution to each window for each bin width, and each region. Then we assessed the goodness-of-fit of each distribution by calculating the log-likelihood of each fitted distribution using the associated sample. We measured the proportion of samples for which each distribution was the best fit, for each bin width value and each region.

We found that the COMb distribution was the best fit for most of the samples regardless of bin width or region. The bin width had an effect on the number of samples for which the COMb distribution was the best fit. The results are summarised in table 3.3. For a bin width of 1ms, the COMb distribution was the best fit for over 90% of samples, the beta-binomial distribution was the best fit for less than 10% of samples, and the binomial distribution was the best fit for less than 1% of samples, across regions. For 5ms bins, the COMb distribution was the best fit for 70 – 80% of samples, the beta-binomial distribution was the best fit for 20 – 30% of the samples, and again the binomial distribution was the best fit for less than 1% of samples, across regions. Finally, for 10ms bins, the COMb distribution was the best fit for 53 – 80% of samples, the beta-binomial distribution was the best fit for 20 – 47% of the samples, and the binomial distribution was the best fit for less than 0.1% of samples, across regions.



(A) Example of fitted distributions.

(B) Proportion of best fit

FIGURE 3.6: (A) An example of the binomial, beta-binomial, and Conway-Maxwell-binomial distributions fitted to a sample of neural activity. The Conway-Maxwell-binomial distribution is the best fit in this case. The histogram shows the empirical distribution of the sample. The probability mass function of each distribution is indicated by a different coloured line. (B) Across all samples in all trials, the proportion of samples for which each fitted distribution was the best fit. The Conway-Maxwell-binomial distribution was the best fit for 93% of the samples taken from V1 using a bin width of 1ms.

<b>Bin Width (ms)</b>	<b>Binomial</b>	<b>Beta-binomial</b>	<b>COMb</b>
1ms	< 1%	< 10%	> 90%
5ms	< 0.1%	20 – 30%	70 – 80%
10ms	< 0.1%	20 – 47%	53 – 80%

TABLE 3.3: Proportion of samples for which each distribution was the best fit, grouped by bin width. The COMb distribution is the best fit most of the time.

### 1959 3.4.3 Conway-Maxwell-binomial distribution captures changes in association 1960 at stimulus onset

We fit a Conway-Maxwell-binomial (COMb) distribution to the number of active neurons in the 1ms time bins in a 100ms sliding window. We also measured the correlation coefficient between the spike counts of all possible pairs of neurons, and took the average of these coefficients. We did this for all the trials with a visual stimulus. We observed a reduction in the COMb distribution's  $\nu$  parameter at stimulus onset from around 1 to between 0 and 1 (see figure 3.7a). A value of  $\nu$  less than 1 indicates positive association between the neurons (see section 3.3.5). We might expect to see this positive association reflected in the correlation coefficients, but this is not the case. We see no change in the time series of average correlation measures at stimulus onset.

This may be due to the very short time bin we used in this case. We know that using small time bins can artificially reduce correlation measurements (Cohen and Kohn, 2011). In this case, fitting the COMb distribution may be a useful way to measure association in a neuronal ensemble over very short timescales (< 10ms).

### **1974 3.4.4 Replicating stimulus related quenching of neural variability**

Churchland et al. (2010) inspected the effect of a stimulus on neural variability. One of the measures of neural variability that they employed was the Fano factor of the spike counts of individual cells (see section 3.3.4). They found a reduction in neural variability as measured by the Fano factor in various cortical areas in a macaque at the onset of various visual stimuli, or a juice reward (Churchland et al., 2010).

1980 We measured the Fano factor of the spike count of each cell in each brain region, during  
1981 each trial. We measured the mean and standard error of these Fano factors from 500ms  
1982 before stimulus onset until 1000ms after stimulus end. For the primary visual cortex, we  
1983 found a transient reduction in the Fano factor immediately after stimulus onset. We used  
1984 a Mann-Whitney U test to check that the Fano factors measured in a window starting at

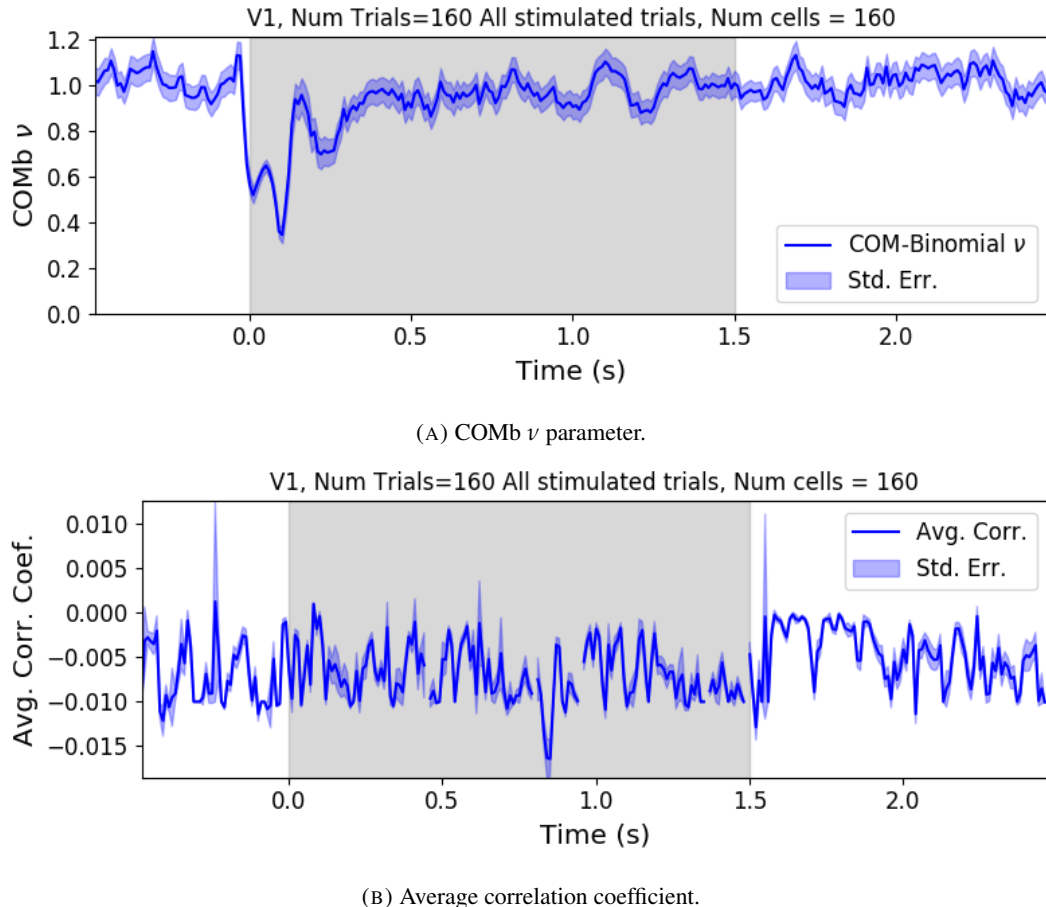


FIGURE 3.7: (A) We fit a Conway-Maxwell-binomial distribution to the number of active neurons in 1ms time bins of a 100ms sliding window. We did this for all trials with a visual stimulus and took the average across those trials. We see a transient drop in value for the distribution's  $\nu$  parameter at stimulus onset. This shows an increase in association between the neurons. (B) We measured the correlation coefficient between the spike counts of all possible pairs of neurons in the same sliding window. We took the average of those coefficients. We also did this for every visually stimulated trial, and took the average across trials. The increase in association is not reflected with an increase in average correlation.

1985 stimulus onset and ending 100ms later were significantly lower than the factors measured  
 1986 in a window ending at stimulus onset ( $p < 0.001$ , see figure 3.8a). We did not get this  
 1987 statistically significant result in any other region.

1988 Our findings agree with those of Churchland et al. for the primary visual cortex. However  
 1989 Churchland also found a reduction in the Fano factor in the dorsal premotor cortex (PMd) at  
 1990 stimulus onset. Our measurements from the mouse motor cortex show no change at stimulus  
 1991 onset (see figure 3.8b). This could indicate some difference in the functionality of the motor  
 1992 cortex in a macaque and the motor cortex of a mouse.

1993 Similar to these findings in the Fano factor, we found a reduction in the  $\nu$  parameter of  
 1994 the COMB distribution on stimulus onset in V1 (figure 3.7a) and in no other region from

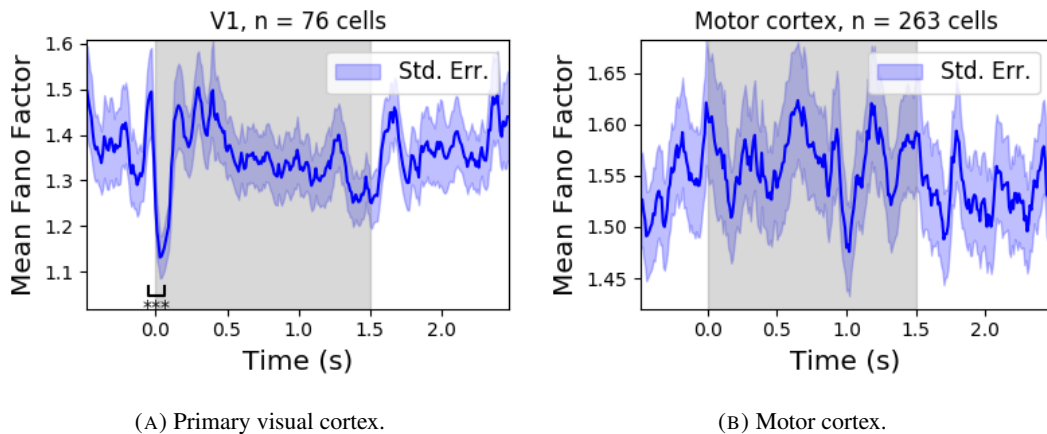


FIGURE 3.8: (A) The mean Fano factor of the spike counts of the cells in the primary visual cortex. Means were taken across cells first, then across trials. There was a significant decrease in the Fano factors immediately after stimulus onset. (B) The mean Fano factor of the spike counts of the cells in the motor cortex. No significant change in measurements at any point.

1995 which we had data. Specifically, the  $\nu$  parameter reduced from around 1, to between 1 and 0.  
 1996 This represents a change from no association between the neurons, to a positive association.  
 1997 It is possible that this positive association may be responsible for the reduction in the Fano  
 1998 factor.

### 1999 3.5 Discussion

2000 Our aim in this research was to develop a new statistical method for analysing the activity  
 2001 of a neuronal ensemble at very short timescales. We wanted our method to use information  
 2002 taken from the whole ensemble, but we also wanted the method to be quick and easy to  
 2003 implement. It is likely that analysis methods with these characteristics will become valuable  
 2004 as electrophysiological datasets include readings from more cells over longer time periods. In  
 2005 this case, we used the number of active, or spiking, neurons in a very short time bin ( $< 10\text{ms}$ )  
 2006 as a measure of ensemble activity.

2007 First of all, we showed that there were changes in response that we could model at these  
 2008 very short time scales in some of the brain regions from which we had recordings. We ob-  
 2009 served changes in the average number of active neurons, and the variance of the number of  
 2010 active neurons in three different brain regions in response to visual stimuli. Since we know  
 2011 that correlated behaviour is associated with sensory perception (deCharms and Merzenich,  
 2012 1996), we might hope to measure the pairwise correlations within the neuronal population  
 2013 in order to further investigate these responses. But, using such short time bins can produce

2014 artificially small spike count correlation measurements (Cohen and Maunsell, 2009). Over-  
2015 coming this limitation was one of our objectives for our new method. In order to do this, we  
2016 abandoned the idea of measuring the correlations directly and embraced the concept of *asso-*  
2017 *ciation*. In order to quantify the association between neurons, we used the Conway-Maxwell-  
2018 binomial distribution to model the number of active (spiking) neurons in an ensemble as a  
2019 sum of possibly associated Bernoulli random variables.

2020 We showed that the Conway-Maxwell-binomial distribution performed better than the  
2021 more common options of the binomial and beta-binomial distributions. Furthermore, we  
2022 showed that the positively associated behaviour between neurons in the primary visual cortex  
2023 could be captured by fitting a Conway-Maxwell-binomial distribution, but was not captured  
2024 by the more standard approach of measuring the spike count correlation. The associated  
2025 behaviour could not be measured using spike count correlations, because of the very short  
2026 bins required to capture short timescale behaviour.

2027 We replicated a famous result from Churchland et al (2010) relating to the quenching of  
2028 neural variability in cortical areas at stimulus onset, and in doing so, we established a corre-  
2029 spondence between the association quantifying parameter of the Conway-Maxwell-binomial  
2030 (COMB) distribution and the neural variability as measured by the Fano factor. We found a  
2031 reduction in the  $\nu$  parameter of the COMB distribution at stimulus onset, indicating a change  
2032 from no association to positive association between neurons in V1. We found a corresponding  
2033 reduction in the Fano factor of the individual cells in V1. The positive association between  
2034 neurons induced by the stimulus would constrain the neurons to fire at the same time. The  
2035 stimulus also induced a larger number of neurons to spike. These two actions combined could  
2036 cause an increase in the firing rate of individual cells that is greater in magnitude than the in-  
2037 crease in firing rate variability. If this is indeed the case, then the association as captured by  
2038 the COMB distribution could be regarded as one of the ‘natural parameters’ of the ensemble  
2039 response for short timescales. That is, a quantity that directly measures some aspect of the  
2040 behaviour of the ensemble. In this case, it the correlated behaviour of the individual neurons  
2041 is captured.

2042 This work could be just a first step in creating analysis methods based on the Conway-  
2043 Maxwell-binomial distribution, or similar statistical models. One way to extend the method  
2044 would be to pair it up with the ‘Population Tracking model’ (O’Donnell et al., 2017). This  
2045 model attempts to characterise the interaction between an ensemble and each member of the  
2046 ensemble by quantifying the probability of spiking for a given a cell, given the number of  
2047 active cells in the whole population. Combining this model with the COMB distribution

2048 would give us a model that could accurately fit the number of active neurons at any moment,  
2049 and that gives a probability of firing for each cell, and therefore probabilities for full spiking  
2050 patterns, without adding a huge number of parameters to fit.

2051 A more complex way to extend the model would be to fit a Conway-Maxwell-binomial  
2052 distribution to data recorded from multiple brain regions simultaneously, with a different fit  
2053 for each region, then to analyse the temporal relationship between the fitted parameters of  
2054 each region. If we analysed the time series of the COMB distribution parameters from the  
2055 different regions, looking at cross-correlations between regions, this may give some results  
2056 relating to the timescales in which information is processed in different brain regions.

<sup>2057</sup> **Chapter 4**

<sup>2058</sup> **Studies with practical limitations &**  
<sup>2059</sup> **negative results**



2060

## *Abstract*

2061 Here I will present some details on research topics that I started, but that unfortunately did not  
2062 lead anywhere useful. There are two pieces of research, based on two papers. Each paper is  
2063 related to the overall theme of my PhD of analysing and modelling behaviours of populations  
2064 of neurons. The first part is based on a model of parallel spike trains including higher order  
2065 interactions by Shimazaki et al (2012). The second part is based on a multiscale model for  
2066 making inferences on hierarchical data.

2067 **4.1 Dynamic state space model of pairwise and higher order neu-  
2068 ronal correlations**

2069 In their paper Shimazaki et al (2012) aimed to model spike trains from populations of neurons  
2070 in parallel, with pairwise and higher order dynamic interactions between the trains. They  
2071 modelled the spike trains as multi-variate binary processes using a log-linear model, and they  
2072 extracted spike interaction parameters using a Bayesian filter/EM-algorithm. They developed  
2073 a goodness-of-fit measure for the model to test if including these higher order correlations  
2074 is necessary for an accurate model. Their measure was based on the Bayes factor but they  
2075 also assessed the suitability of higher order models using the AIC and BIC. So the increase  
2076 in the number of parameters associated with fitting higher order interactions was taken into  
2077 account. They tested the performance of the model on synthetic data with known higher  
2078 order correlations. They used the model to look for higher order correlations in data from  
2079 awake behaving animals. They use the model to demonstrate dynamic appearance of higher  
2080 order correlations in the monkey motor cortex (Shimazaki et al., 2012).

2081 We used the available Python repository to implement the model, and we successfully  
2082 worked through the tutorial provided. But we found that the model did not scale well to  
2083 larger populations. We attempted to fit the model to a population of 10 neurons and found we  
2084 didn't manage to finish the process. Since, our goal was to find a model to scale to hundreds  
2085 or thousands of neurons, we decided that this model was no longer worth pursuing.

2086 **4.2 A multiscale model for hierarchical data applied to  
2087 neuronal data**

2088 In their paper Kolaczyk et al (2001) developed a framework for a modelling hierarchically  
2089 aggregated data, and making inferences based on a model arising from this framework. They  
2090 assumed that a hierarchical aggregation existed on the data in question, where each element at  
2091 each level of the hierarchy had some associated measurements, an associated mean process,  
2092 which was the expected value of these measurements. They also assumed that the measure-  
2093 ments of each parent were equal to the sum of the measurements from all of its children.  
2094 They showed that these assumptions gave rise to a relationship between parent and child  
2095 measurements across all levels of the hierarchy, where the product of the likelihood of the  
2096 parameters of the lowest level of the hierarchy can be expressed as products of conditional  
2097 likelihoods of the elements of higher levels of the hierarchy (Kolaczyk and Huang, 2010).

2098 They gave examples of these expressions for measurements sampled from Gaussian dis-  
2099 tributions, and Poisson distributions, and showed the definitions of the hierarchical param-  
2100 eters which reparametrise the distribution of these data taking the hierarchy into account.  
2101 They go on to suggest prior distributions for this multiscale model, and integrate these priors  
2102 to give posterior distributions for the measurements from each element at each level in the hi-  
2103 erarchy, and expressions for the MAP estimated parameters of each the associated processes  
2104 (Kolaczyk and Huang, 2010).

2105 We implemented their model in Python by creating some synthetic data from Poisson  
2106 distributions, and defining a hierarchy by agglomerating these data. We calculated the MAP  
2107 estimates using our knowledge of the hierarchy, and using the expressions given in the paper.  
2108 We found that the MAP estimates were far less accurate than would be achieved by simply  
2109 ignoring the hierarchy during estimation, and using a maximum likelihood approach. After  
2110 that, we decided to move on.

**4.3 Discussion**

Ideas (not in order):

• Calcium imaging limitations (spike inference not always possible)

• Judging by Greenberg biophysical modelling is the way to go.

• our fluorescence model could be useful in a number of situations.

• Applied new network science to new electrophysiological dataset.

• Abandon calcium

• Multi region calcium imaging dataset would be useful?

• Results might be intuitive, but are new nonetheless (as far as I know)

• Potential for more network science applications?

• Applied the COMB distribution to neuronal data for the first time.

• captures correlated behaviour by quantifying *association*.

• Abandon correlations.

• coupling with existing models could yield some nice models.

• More statistical invention could be useful.



# 2126 Bibliography

- 2127 Allen, William E. et al. (2019). “Thirst regulates motivated behavior through modulation of  
 2128 brainwide neural population dynamics”. In: *Science* 364.6437. ISSN: 0036-8075. DOI:  
 2129 [10.1126/science.aav3932](https://doi.org/10.1126/science.aav3932). eprint: <https://science.sciencemag.org/content/364/6437/eaav3932.full.pdf>. URL: <https://science.sciencemag.org/content/364/6437/eaav3932>.
- 2132 Baadel, S., F. Thabtah, and J. Lu (2016). “Overlapping clustering: A review”. In: *2016 SAI Computing Conference (SAI)*, pp. 233–237. DOI: [10.1109/SAI.2016.7555988](https://doi.org/10.1109/SAI.2016.7555988).
- 2134 Baldassano, Christopher et al. (2017). “Discovering Event Structure in Continuous Narrative  
 2135 Perception and Memory”. In: *Neuron* 95.3, 709 –721.e5. ISSN: 0896-6273. DOI: <https://doi.org/10.1016/j.neuron.2017.06.041>. URL: <http://www.sciencedirect.com/science/article/pii/S0896627317305937>.
- 2138 Bartol, Thomas M. et al. (2015). “Computational reconstitution of spine calcium transients  
 2139 from individual proteins”. In: *Frontiers in Synaptic Neuroscience* 7, p. 17. ISSN: 1663-  
 2140 3563. DOI: [10.3389/fnsyn.2015.00017](https://doi.org/10.3389/fnsyn.2015.00017). URL: <https://www.frontiersin.org/article/10.3389/fnsyn.2015.00017>.
- 2142 Berens, Philipp et al. (May 2018). “Community-based benchmarking improves spike rate inference  
 2143 from two-photon calcium imaging data”. In: *PLOS Computational Biology* 14.5, pp. 1–13. DOI: [10.1371/journal.pcbi.1006157](https://doi.org/10.1371/journal.pcbi.1006157). URL: <https://doi.org/10.1371/journal.pcbi.1006157>.
- 2146 Bezanson, Jeff et al. (Sept. 2012). “Julia: A Fast Dynamic Language for Technical Computing”. In: *MIT*.
- 2148 Chen, Tsai-Wen et al. (July 2013). “Ultrasensitive fluorescent proteins for imaging neuronal  
 2149 activity”. In: *Nature* 499, 295–300. DOI: [10.1038/nature12354](https://doi.org/10.1038/nature12354). URL: <https://doi.org/10.1038/nature12354>.
- 2151 Churchland, Mark M. et al. (2010). “Stimulus onset quenches neural variability: a widespread  
 2152 cortical phenomenon”. eng. In: *Nature neuroscience* 13.3. 20173745[pmid], pp. 369–378.  
 2153 ISSN: 1546-1726. DOI: [10.1038/nn.2501](https://doi.org/10.1038/nn.2501). URL: <https://pubmed.ncbi.nlm.nih.gov/20173745>.

- 2155 Cohen, Marlene R. and Adam Kohn (2011). “Measuring and interpreting neuronal correla-  
2156 tions”. In: *Nature Neuroscience* 14.7, pp. 811–819. ISSN: 1546-1726. DOI: [10.1038/nn.2842](https://doi.org/10.1038/nn.2842). URL: <https://doi.org/10.1038/nn.2842>.
- 2158 Cohen, Marlene R. and John H. R. Maunsell (2009). “Attention improves performance pri-  
2159 marily by reducing interneuronal correlations”. eng. In: *Nature neuroscience* 12.12. 19915566[pmid],  
2160 pp. 1594–1600. ISSN: 1546-1726. DOI: [10.1038/nn.2439](https://doi.org/10.1038/nn.2439). URL: <https://pubmed.ncbi.nlm.nih.gov/19915566>.
- 2162 Dana, Hod et al. (Sept. 2014). “Thy1-GCaMP6 Transgenic Mice for Neuronal Population  
2163 Imaging In Vivo”. In: *PloS one* 9, e108697. DOI: [10.1371/journal.pone.0108697](https://doi.org/10.1371/journal.pone.0108697).
- 2165 deCharms, R. Christopher and Michael M. Merzenich (1996). “Primary cortical represen-  
2166 tation of sounds by the coordination of action-potential timing”. In: *Nature* 381.6583,  
2167 pp. 610–613. ISSN: 1476-4687. DOI: [10.1038/381610a0](https://doi.org/10.1038/381610a0). URL: <https://doi.org/10.1038/381610a0>.
- 2169 Deneux, Thomas et al. (July 2016). “Accurate spike estimation from noisy calcium signals  
2170 for ultrafast three-dimensional imaging of large neuronal populations in vivo”. In: *Nature  
2171 Communications* 7.1. DOI: [10.1038/ncomms12190](https://doi.org/10.1038/ncomms12190). URL: <https://doi.org/10.1038/ncomms12190>.
- 2173 Faas, G. C. et al. (Mar. 2011). “Calmodulin as a direct detector of Ca<sup>2+</sup> signals”. In: *Nature  
2174 neuroscience* 14.3, pp. 301–304. DOI: [10.1038/nn.2746](https://doi.org/10.1038/nn.2746). URL: <https://doi.org/10.1038/nn.2746>.
- 2176 Fiala, John C. and Kristen M. Harris (1999). *Dendrite Structure*.
- 2177 Flach, Boris (Sept. 2013). “A Class of Random Fields on Complete Graphs with Tractable  
2178 Partition Function”. In: *IEEE transactions on pattern analysis and machine intelligence*  
2179 35, pp. 2304–6. DOI: [10.1109/TPAMI.2013.99](https://doi.org/10.1109/TPAMI.2013.99).
- 2180 Forney, G. D. (1973). “The viterbi algorithm”. In: *Proceedings of the IEEE* 61.3, pp. 268–  
2181 278. ISSN: 1558-2256. DOI: [10.1109/PROC.1973.9030](https://doi.org/10.1109/PROC.1973.9030).
- 2182 Fosdick, Bailey et al. (Aug. 2016). “Configuring Random Graph Models with Fixed Degree  
2183 Sequences”. In: *SIAM Review* 60. DOI: [10.1137/16M1087175](https://doi.org/10.1137/16M1087175).
- 2184 Friedrich, Johannes and Liam Paninski (2016). “Fast Active Set Methods for Online Spike  
2185 Inference from Calcium Imaging”. In: *Advances in Neural Information Processing Systems* 29. Ed. by D. D. Lee et al. Curran Associates, Inc., pp. 1984–1992. URL: <http://papers.nips.cc/paper/6505-fast-active-set-methods-for-online-spike-inference-from-calcium-imaging.pdf>.

- 2189 Ganmor, Elad, Ronen Segev, and Elad Schneidman (2011). “Sparse low-order interaction  
2190 network underlies a highly correlated and learnable neural population code”. In: *Proceed-  
2191 ings of the National Academy of Sciences* 108.23, pp. 9679–9684. ISSN: 0027-8424. DOI:  
2192 [10.1073/pnas.1019641108](https://doi.org/10.1073/pnas.1019641108). eprint: <https://www.pnas.org/content/108/23/9679.full.pdf>. URL: <https://www.pnas.org/content/108/23/9679>.
- 2195 Girard, P., J. M. Hupé, and J. Bullier (2001). “Feedforward and Feedback Connections Be-  
2196 tween Areas V1 and V2 of the Monkey Have Similar Rapid Conduction Velocities”. In:  
2197 *Journal of Neurophysiology* 85.3. PMID: 11248002, pp. 1328–1331. DOI: [10.1152/jn.2001.85.3.1328](https://doi.org/10.1152/jn.2001.85.3.1328). eprint: <https://doi.org/10.1152/jn.2001.85.3.1328>. URL: <https://doi.org/10.1152/jn.2001.85.3.1328>.
- 2200 Greenberg, David et al. (Nov. 2018). “Accurate action potential inference from a calcium  
2201 sensor protein through biophysical modeling:” in: DOI: [10.1101/479055](https://doi.org/10.1101/479055).
- 2202 Gründemann, Jan et al. (2019). “Amygdala ensembles encode behavioral states”. In: *Science*  
2203 364.6437. ISSN: 0036-8075. DOI: [10.1126/science.aav8736](https://doi.org/10.1126/science.aav8736). eprint: <https://science.sciencemag.org/content/364/6437/eaav8736.full.pdf>. URL: <https://science.sciencemag.org/content/364/6437/eaav8736>.
- 2207 Hodgkin, A. L. and A. F. Huxley (1939). “Action Potentials Recorded from Inside a Nerve Fi-  
2208 bre”. In: *Nature* 144.3651, pp. 710–711. ISSN: 1476-4687. DOI: [10.1038/144710a0](https://doi.org/10.1038/144710a0).  
2209 URL: <https://doi.org/10.1038/144710a0>.
- 2210 Humphries, Mark et al. (Jan. 2019). “Spectral rejection for testing hypotheses of structure in  
2211 networks”. In:
- 2212 Humphries, Mark D. (2011). “Spike-Train Communities: Finding Groups of Similar Spike  
2213 Trains”. In: *Journal of Neuroscience* 31.6, pp. 2321–2336. ISSN: 0270-6474. DOI: [10.1523/JNEUROSCI.2853-10.2011](https://doi.org/10.1523/JNEUROSCI.2853-10.2011). eprint: <https://www.jneurosci.org/content/31/6/2321.full.pdf>. URL: <https://www.jneurosci.org/content/31/6/2321>.
- 2217 Jun, James J. et al. (2017). “Fully integrated silicon probes for high-density recording of  
2218 neural activity”. In: *Nature* 551.7679, pp. 232–236. ISSN: 1476-4687. DOI: [10.1038/nature24636](https://doi.org/10.1038/nature24636). URL: <https://doi.org/10.1038/nature24636>.

- 2220 Kilhoffer, Marie-Claude et al. (Sept. 1992). “Use of Engineered Proteins With Internal Tryp-  
2221 tophean Reporter Groups and Perturbation Techniques to Probe the Mechanism of Ligand-  
2222 Protein Interactions: Investigation of the Mechanism of Calcium Binding to Calmod-  
2223 ulin”. In: *Biochemistry* 31.34, pp. 8098–8106. DOI: [10.1021/bi00149a046](https://doi.org/10.1021/bi00149a046). URL:  
2224 <https://doi.org/10.1021/bi00149a046>.
- 2225 Koch, Christoff (1999). *Biophysics of Computation: Information Processing in Single Neu-*  
2226 *rons*. Oxford University Press. ISBN: ISBN 0-19-510491-9.
- 2227 Kolaczyk, Eric and Haiying Huang (Sept. 2010). “Multiscale Statistical Models for Hier-  
2228 archical Spatial Aggregation”. In: *Geographical Analysis* 33, pp. 95 –118. DOI: [10.1111/j.1538-4632.2001.tb00439.x](https://doi.org/10.1111/j.1538-4632.2001.tb00439.x).
- 2230 Lee, Suk-HO et al. (July 2000). “Differences in Ca<sup>2+</sup> buffering properties between excitatory  
2231 and inhibitory hippocampal neurons from the rat”. In: *The Journal of Physiology* 525.  
2232 DOI: [10.1111/j.1469-7793.2000.t01-3-00405.x](https://doi.org/10.1111/j.1469-7793.2000.t01-3-00405.x).
- 2233 Litwin-Kumar, Ashok, Maurice Chacron, and Brent Doiron (Sept. 2012). “The Spatial Struc-  
2234 ture of Stimuli Shapes the Timescale of Correlations in Population Spiking Activity”.  
2235 In: *PLoS computational biology* 8, e1002667. DOI: [10.1371/journal.pcbi.1002667](https://doi.org/10.1371/journal.pcbi.1002667).
- 2237 Maravall, M et al. (May 2000). “Estimating intracellular calcium concentrations and buffer-  
2238 ing without wavelength ratioing”. In: *Biophysical Journal* 78.5, pp. 2655–2667. DOI:  
2239 [10.1016/S0006-3495\(00\)76809-3](https://doi.org/10.1016/S0006-3495(00)76809-3). URL: [https://doi.org/10.1016/S0006-3495\(00\)76809-3](https://doi.org/10.1016/S0006-3495(00)76809-3).
- 2241 Maugis, Pa (Jan. 2014). “Event Conditional Correlation: Or How Non-Linear Linear Depen-  
2242 dence Can Be”. In:
- 2243 Meilă, Marina (2007). “Comparing clusterings—an information based distance”. In: *Journal*  
2244 *of Multivariate Analysis* 98.5, pp. 873 –895. ISSN: 0047-259X. DOI: <https://doi.org/10.1016/j.jmva.2006.11.013>. URL: <http://www.sciencedirect.com/science/article/pii/S0047259X06002016>.
- 2247 Murray, John D. et al. (2014). “A hierarchy of intrinsic timescales across primate cortex”.  
2248 In: *Nature Neuroscience* 17.12, pp. 1661–1663. ISSN: 1546-1726. DOI: [10.1038/nn.3862](https://doi.org/10.1038/nn.3862). URL: <https://doi.org/10.1038/nn.3862>.
- 2250 Neher, E. and G. J. Augustine (1992). “Calcium gradients and buffers in bovine chromaffin  
2251 cells”. eng. In: *The Journal of physiology* 450. 1331424[pmid], pp. 273–301. ISSN: 0022-  
2252 3751. DOI: [10.1113/jphysiol.1992.sp019127](https://doi.org/10.1113/jphysiol.1992.sp019127). URL: <https://pubmed.ncbi.nlm.nih.gov/1331424>.

- 2254 O'Donnell, Cian et al. (Jan. 2017). "The population tracking model: a simple, scalable statis-  
2255 tical model for neural population data". English. In: *Neural Computation* 29.1, pp. 50–  
2256 93. ISSN: 0899-7667. DOI: [10.1162/NECO\\_a\\_00910](https://doi.org/10.1162/NECO_a_00910).
- 2257 Patterson, Carolyn A. et al. (2014). "Similar adaptation effects in primary visual cortex and  
2258 area MT of the macaque monkey under matched stimulus conditions". In: *Journal of Neu-  
2259 rophysiology* 111.6. PMID: 24371295, pp. 1203–1213. DOI: [10.1152/jn.00030.2013](https://doi.org/10.1152/jn.00030.2013).  
2260 eprint: <https://doi.org/10.1152/jn.00030.2013>. URL: <https://doi.org/10.1152/jn.00030.2013>.
- 2261 Peron, Simon P. et al. (2015). "A Cellular Resolution Map of Barrel Cortex Activity during  
2262 Tactile Behavior". In: *Neuron* 86.3, pp. 783–799. ISSN: 0896-6273. DOI: [10.1016/j.neuron.2015.03.027](https://doi.org/10.1016/j.neuron.2015.03.027). URL: <https://doi.org/10.1016/j.neuron.2015.03.027>.
- 2263 Pnevmatikakis, E.A. et al. (Jan. 2016). "Simultaneous Denoising, Deconvolution, and Demix-  
2264 ing of Calcium Imaging Data". In: *Neuron* 89.2, pp. 285–299. DOI: [10.1016/j.neuron.2015.11.037](https://doi.org/10.1016/j.neuron.2015.11.037). URL: <https://doi.org/10.1016/j.neuron.2015.11.037>.
- 2265 Pnevmatikakis, Eftychios et al. (Nov. 2013). "Bayesian spike inference from calcium imaging  
2266 data". In: *Conference Record - Asilomar Conference on Signals, Systems and Computers*.  
2267 DOI: [10.1109/ACSSC.2013.6810293](https://doi.org/10.1109/ACSSC.2013.6810293).
- 2268 Pnevmatikakis, Eftychios et al. (Sept. 2014). "A structured matrix factorization framework  
2269 for large scale calcium imaging data analysis". In:
- 2270 Schneidman, Elad et al. (2006). "Weak pairwise correlations imply strongly correlated net-  
2271 work states in a neural population". eng. In: *Nature* 440.7087. 16625187[pmid], pp. 1007–  
2272 1012. ISSN: 1476-4687. DOI: [10.1038/nature04701](https://doi.org/10.1038/nature04701). URL: <https://pubmed.ncbi.nlm.nih.gov/16625187>.
- 2273 Shannon, C. E. (1948). "A Mathematical Theory of Communication". In: *Bell System Techni-  
2274 cal Journal* 27.3, pp. 379–423. DOI: [10.1002/j.1538-7305.1948.tb01338.x](https://doi.org/10.1002/j.1538-7305.1948.tb01338.x).  
2275 eprint: <https://onlinelibrary.wiley.com/doi/pdf/10.1002/j.1538-7305.1948.tb01338.x>. URL: <https://onlinelibrary.wiley.com/doi/abs/10.1002/j.1538-7305.1948.tb01338.x>.
- 2276 Shimazaki, Hideaki et al. (2012). "State-space analysis of time-varying higher-order spike  
2277 correlation for multiple neural spike train data". eng. In: *PLoS computational biology* 8.3.  
2278 22412358[pmid], e1002385–e1002385. ISSN: 1553-7358. DOI: [10.1371/journal.pcbi.1002385](https://doi.org/10.1371/journal.pcbi.1002385). URL: <https://pubmed.ncbi.nlm.nih.gov/22412358>.

- 2288 Steinmetz, Nick, Matteo Carandini, and Kenneth D. Harris (2019). "Single Phase3" and  
2289 "Dual Phase3" *Neuropixels Datasets*. DOI: [10.6084/m9.figshare.7666892.v2](https://doi.org/10.6084/m9.figshare.7666892.v2). URL: [https://figshare.com/articles/dataset/\\_Single\\_Phase3\\_Neuropixels\\_Dataset/7666892/2](https://figshare.com/articles/dataset/_Single_Phase3_Neuropixels_Dataset/7666892/2).
- 2290 Stringer, Carsen et al. (2019). "Spontaneous behaviors drive multidimensional, brainwide ac-  
2291 tivity". In: *Science* 364.6437. ISSN: 0036-8075. DOI: [10.1126/science.aav7893](https://doi.org/10.1126/science.aav7893).  
2292 eprint: <https://science.sciencemag.org/content/364/6437/eaav7893.full.pdf>. URL: <https://science.sciencemag.org/content/364/6437/eaav7893>.
- 2293 Tada, Mayumi et al. (2014). "A highly sensitive fluorescent indicator dye for calcium imag-  
2294 ing of neural activity in vitro and in vivo". In: *European Journal of Neuroscience* 39.11,  
2295 pp. 1720–1728. DOI: [10.1111/ejn.12476](https://doi.org/10.1111/ejn.12476). eprint: <https://onlinelibrary.wiley.com/doi/pdf/10.1111/ejn.12476>. URL: <https://onlinelibrary.wiley.com/doi/abs/10.1111/ejn.12476>.
- 2296 Tian, Lin et al. (2009). "Imaging neural activity in worms, flies and mice with improved  
2297 GCaMP calcium indicators". eng. In: *Nature methods* 6.12. 19898485[pmid], pp. 875–  
2298 881. ISSN: 1548-7105. DOI: [10.1038/nmeth.1398](https://doi.org/10.1038/nmeth.1398). URL: <https://pubmed.ncbi.nlm.nih.gov/19898485>.
- 2299 Tkačik, Gašper et al. (2014). "Searching for collective behavior in a large network of sen-  
2300 sory neurons". eng. In: *PLoS computational biology* 10.1. 24391485[pmid], e1003408–  
2301 e1003408. ISSN: 1553-7358. DOI: [10.1371/journal.pcbi.1003408](https://doi.org/10.1371/journal.pcbi.1003408). URL:  
2302 <https://pubmed.ncbi.nlm.nih.gov/24391485>.
- 2303 Treves, Alessandro and Stefano Panzeri (1995). "The Upward Bias in Measures of Informa-  
2304 tion Derived from Limited Data Samples". In: *Neural Computation* 7.2, pp. 399–407.  
2305 DOI: [10.1162/neco.1995.7.2.399](https://doi.org/10.1162/neco.1995.7.2.399). eprint: <https://doi.org/10.1162/neco.1995.7.2.399>. URL: <https://doi.org/10.1162/neco.1995.7.2.399>.
- 2306 Vinh, Nguyen Xuan, Julien Epps, and James Bailey (Dec. 2010). "Information Theoretic  
2307 Measures for Clusterings Comparison: Variants, Properties, Normalization and Correc-  
2308 tion for Chance". In: *J. Mach. Learn. Res.* 11, 2837–2854. ISSN: 1532-4435.
- 2309 Vogelstein, Joshua T. et al. (Oct. 2010). "Fast nonnegative deconvolution for spike train infer-  
2310 ence from population calcium imaging". In: *Journal of neurophysiology* 104.6, 295–300.  
2311 DOI: [10.1152/jn.01073.2009](https://doi.org/10.1152/jn.01073.2009). URL: <https://dx.doi.org/10.1152%2Fjn.01073.2009>.
- 2312
- 2313
- 2314
- 2315
- 2316
- 2317
- 2318
- 2319
- 2320
- 2321

- 2322 Wierzynski, "Casimir M. et al. ("2009"). "State-Dependent Spike-Timing Relationships be-  
2323 tween Hippocampal and Prefrontal Circuits during Sleep"". In: "Neuron" "61"."4", "587  
2324 –596". ISSN: "0896-6273". DOI: "<https://doi.org/10.1016/j.neuron.2009.01.011>". URL: "<http://www.sciencedirect.com/science/article/pii/S0896627309000786>".
- 2327 Zariwala, Hatim A. et al. (2012). "A Cre-dependent GCaMP3 reporter mouse for neuronal  
2328 imaging in vivo". eng. In: *The Journal of neuroscience : the official journal of the Society  
2329 for Neuroscience* 32.9. 22378886[pmid], pp. 3131–3141. ISSN: 1529-2401. DOI: [10.1523/JNEUROSCI.4469-11.2012](https://doi.org/10.1523/JNEUROSCI.4469-11.2012). URL: <https://pubmed.ncbi.nlm.nih.gov/22378886>.
- 2332 Zou, Hui and Trevor Hastie (2005). "Regularization and variable selection via the Elastic  
2333 Net". In: *Journal of the Royal Statistical Society, Series B* 67, pp. 301–320.